eman ta zabal zazu
Universidad del País Vasco
Euskal Herriko Unibertsitatea

DOCTORAL THESIS

Magnetotactic bacteria: sources of model magnetic nanoparticles and biorobots for localized therapies

David Gandia Aguado

Directors:
Dr. Mª Luisa Fdez-Gubieda Ruiz
Dr. Javier Alonso Masa

2022

Resumen

Las bacterias magnetotácticas (MTB por sus siglas en inglés) constituyen un grupo de procariotas acuáticas móviles capaces de alinearse pasivamente con el campo magnético terrestre gracias a su capacidad de biomineralizar nanopartículas magnéticas, denominadas magnetosomas. La bacteria organiza estas nanopartículas en forma de cadena a lo largo de su eje longitudinal. Los magnetosomas son inclusiones intracelulares compuestas de un núcleo cristalino de un mineral magnético (típicamente magnetita, Fe_3O_4, o greigita, Fe_3S_4) rodeado de una membrana lipoproteica de 3-4 nm de espesor.

La existencia de las MTB fue documentada por primera vez por Salvatore Bellini en 1963, cuando observó en muestras de agua dulce que algunos microorganismos migraban de forma preferencial siguiendo la dirección del norte magnético. Para explicar tal comportamiento, sugirió la existencia de "brújulas internas" responsables de la orientación de estos microorganismos, a los que denominó *bacterias magnetosensibles*. Sin embargo, sus hallazgos pasaron desapercibidos para la comunidad científica hasta que Richard P. Blakemore redescubriera de forma independiente las MTB en 1975. Blakemore fue el primero en observar y confirmar la presencia de las "brújulas internas" propuestas por Bellini. Es precisamente Richard P. Blakemore quien acuñó los términos *bacterias magnetotácticas* para referirse a las células, *magnetosomas* para referirse a las nanopartículas, y *magnetotaxis* para describir su habilidad de orientación con el campo magnético terrestre.

Presentes en sedimentos y aguas estratificadas, las MTB han colonizado casi la totalidad de ambientes acuáticos, ya sean marinos o dulces, localizándose en la denominada *zona de transición óxica-anóxica*, en relativamente altas densidades celulares (10^5-10^6 cells·mL^{-1}).

La explicación mayormente aceptada en cuanto al comportamiento magnético de estos microorganismos es la denominada *hipótesis magnetoaerotáctica*. Las MTB, al igual que cualquier ser vivo, necesitan

encontrar zonas óptimas de oxígeno y nutrientes donde poder desarrollarse, en su caso, la zona de transición oxica-anóxica, típicamente cerca de los sedimentos. Según este modelo, la alineación pasiva de las MTB con las líneas de campo magnetico terrestre "fijaría" la célula en una determinada orientación, reduciendo su movimiento de tres dimensiones a un desplazamiento unidimensional (ascenso o descenso en la columna de agua). Esta limitación en la capacidad de movimiento ayudaría a las bacterias a posicionarse en una altura idónea del gradiente químico y redox para su crecimiento, haciendo por tanto más efectiva la quimio- y aerotaxis.

El término "bacteria magnetotáctica" no tiene propiamente un significado taxonómico y hace referencia a un diverso conjunto de microorganismos, los cuales únicamente comparten la característica de biomineralizar una o varias cadenas de magnetosomas para orientarse con el campo magnético terrestre. Una de las peculiaridades de los magnetosomas es que sus propiedades (composición química, forma, tamaño) son características de cada especie bacteriana. El núcleo mineral del magnetosoma se caracteriza por un alto grado de pureza y cristalinidad. Aunque hay diversidad de formas, existen tres patrones morfológicos principales: cuboctaédrico, prismático y en forma de flecha o lanza. Por otro lado, los tamaños típicos de los magnetosomas están entre 35-120 nm.

Tanto las MTB como los magnetosomas son objeto de creciente interés entre la comunidad científica debido a sus particulares características magnéticas y estructurales, que les convierten en buenos candidatos a utilizar en aplicaciones biomédicas y biotecnológicas. Los magnetosomas, además de tener una forma y tamaño uniforme, presentar una alta pureza química y un alto momento magnético térmicamente estable a temperatura ambiente, están rodeados por una membrana de naturaleza lipídica-proteica que les confiere estabilidad, evitando que se agreguen una vez extraidos. Esto además facilita su funcionalización y los hace biocompatibles. Por todo ello, los magnetosomas son considerados nanopartículas ideales para aplicaciones biomédicas, en particular para el tratamiento contra el cáncer mediante hipertermia magnética. Además, la calidad y reproducibilidad de los magnetosomas les convierte en modelos idóneos para, por ejemplo, investigar la relación entre morfología y propiedades magnéticas. Por otro lado, las MTB están empezando a estudiarse como biorrobots contra el cáncer, gracias a sus propiedades de guiado y autopropulsión. En esta Tesis

nos hemos centrado tanto en la aplicabilidad de las MTB para terapia biomédica, como en el interés intrínseco de sus propiedades magnéticas según lo comentado.
La Tesis se ha estructurado en 4 capítulos.

En el *Capítulo* 1, a modo de introducción, describimos por un lado las principales características de las bacterias magnetotácticas y, por otro lado, las capacidades de las MTB como agentes anticancerígenos.

En el *Capítulo 2* investigamos el uso de los magnetosomas como nanopartículas magnéticas modelo. De esta manera, mostraremos cómo el control genético ejercido por las bacterias magnetotácticas a la hora de biomineralizar los magnetosomas nos ofrece una oportunidad incomparable para estudiar la estrecha relación existente entre la morfología y las propiedades magnéticas de las nanopartículas. En este sentido, descifraremos el comportamiento magnético de la cadena de magnetosomas de la especie bacteriana *Magnetospirillum gryphiswaldense* MSR-1, fijando especialmente nuestra atención en la influencia dominante que tiene la anisotropía de forma en este tipo de nanopartículas facetadas. Este trabajo nos servirá para proponer una metodología de análisis compuesta de distintas técnicas experimentales y un modelo computacional basado en la técnica de elementos finitos que puede ser de gran utilidad para otros grupos que trabajen con nanoestructuras magnéticas. Además, mediante la técnica de tomografía y holografía electronica (EHT) veremos la estructura de la cadena y su configuración magnetica.

En el *Capítulo 3* estudiaremos cómo las propiedades magnéticas de los magnetosomas varían en función de la especie bacteriana. Los cambios en la morfología de los magnetosomas de una especie a otra otorgan un cierto control sobre la respuesta magnética de las mismas, especialmente interesante para su potencial uso en un amplio rango de aplicaciones. Por ello, para este estudio, utilizaremos dos especies de bacterias magnetotácticas adicionales, aparte de la *M. gryphiswaldense* MSR-1: *Magnetospirillum magneticum* AMB-1 y *Magnetovibrio blakemorei* MV-1. Estudiaremos las respuesta magnética de estas nuevas especies, mostrando además como el medio de cultivo tiene una gran influencia sobre las propiedades exhibidas por los magnetosomas, proporcionando en su caso una nueva fuente de control sobre las carac-

terísticas magnéticas de las MTB.

En el *Capítulo 4* analizamos con detalle el empleo de las MTB como agentes anticancerígenos. Esto se enmarca dentro de una ambiciosa iniciativa en la que hemos estado trabajando, con el objetivo de mostrar el gran potencial de las bacterias magnetotácticas como biorobots anticancerígenos. Las MTB pueden ser externamente controladas y monitorizadas, gracias a sus capacidades de autopropulsión y fácil guiado; y además los magnetosomas tienen capacidad de generar calor al estar sometidas a un campo magnético alterno. Para ello, primero evaluaremos la respuesta de la *M. gryphiswaldense* MSR-1 en hipertermia magnética y como culminación, mostraremos y describiremos las característiscas de una plataforma de magnetotaxia, construida como parte de esta tesis, para poder monitorizar, guiar y seguir el movimiento de las bacterias magnetotácticas.

Contents

Abbreviations

AC	Alternating Current
AMF	Alternating Magnetic Field
DOG	Difference of Gaussians
DOF	Depth of Field
ECT	Electronic CryoTomography
EHT	Electron Holographic Tomography
EXAFS	Extended X-ray Absorption Fine Structure
FC	Field Cooled
FDA	Food and Drug Administration
FEM	Finite Element Method
FFT	Fast Fourier Transform
FOV	Field of View
FSM	Flask Standard Medium
MFH	Magnetic Fluid Hyperthermia
LAP	Linear Assignment Problem
LLG	Landau-Lifshitz-Gilbert
LOG	Laplacian of Gaussian
LRT	Linear Response Theory
MNP	Magnetic Nanoparticle
MPI	Magnetic Particle Imaging
MRI	Magnetic Resonance Imaging
MSGM	Magnetic Spirillum Growth Medium
MTB	Magnetotactic Bacteria
SA	Self-Assembly
SAR	Specific Absorption Rate
SQUID	Superconducting Quantum Interference Device
SPION	Superparamagnetic Iron Oxide Nanoparticles
SPT	Single Particle Tracking
TEM	Transmission Electron Microscopy
TO	Truncated Octahedron
VSM	Vibrating Sample Magnetometer
WMS	Wolfe's mineral solution
XAFS	X-ray Absorption Fine Structure
XAS	X-ray Absorption Spectroscopy
XMCD	X-ray Magnetic Circular Dichroism
ZFC	Zero-Field Cooled

Chapter 1

Magnetotactic bacteria, magnetosomes and their applications

1.1. What are magnetotactic bacteria?

Magnetotactic bacteria (MTB) are aquatic motile microorganisms with the ability to align and orient themselves in the presence of the Earth's magnetic field [1]. This special property arises due to the presence of one or several chains of intracellular magnetic nanoparticles coated with a lipid bilayer membrane. These magnetic nanoparticles, called *magnetosomes*, have a size between 35–120 nm, being magnetically stable at room temperature [2]. Magnetosomes are arranged in a chain configuration along the longitudinal axis of the bacteria. This configuration maximizes the magnetic moment of the MTB, allowing them to orient in water by the torque the geomagnetic field exerts on the chain.

The first documentation of the existence of MTB was done by Salvatore Bellini in 1963, when he observed, in freshwater samples, that some microorganisms migrated preferentially following the direction of the magnetic north. To explain such behavior, he suggested the existence of internal compasses responsible for the orientation of these microorganisms, which he called "magnetosensitive bacteria". However, his findings went unnoticed by the scientific community until Richard P. Blakemore in 1975 independently rediscovered bacteria in marine sediments swimming along the geomagnetic field lines [1].

By using transmission electron microscopy, he observed intracellular magnetic organelles aligned forming a chain inside the bacteria. R. P. Blakemore referred to these magnetic organelles as *magnetosomes* and classified the bacteria as *magnetotactic bacteria*, MTB [1].
MTB can passively align, Fig 1.1, and actively swim along the geomagnetic field lines [3–5]. This behavior is known as *magnetotaxis*. The arrangement of the magnetosomes in a chain causes the addition of the magnetic moments of every individual magnetosome, turning the cell into a single magnetic dipole. This allows MTB to behave as compass needles that passively get aligned along magnetic field lines. Motile bacteria are of crucial importance in aquatic biogeochemistry as they transport minerals and organic matter [6, 7]. The movement of these aquatic bacteria directly depends on environmental signals such as flow [8], light [9], gravity [10], temperature [11] and chemical gradients [12, 13]. MTB live in heterogeneous habitats like freshwater, marine habitats and wet soils, and actively participate in biogeochemical processes [14], including the Earth's iron and sulfur cycles, since they use these elements as nutrients [3] [15]. The most accepted justification for the magnetic behavior of MTB is the so-called *magnetoaerotactic hypothesis* [16–18]. To this respect, MTB have sensory elements that guide them to the regions with their preferred oxygen concentration, an ability called *aerotaxis*. On the other hand, the chain of magnetosomes provides them with an additional advantage, the magnetotaxis [5]. The geomagnetic field lines act as a pathway for searching the optimal position in the stratified water column, since MTB aligned in the Earth's magnetic field reduce a three-dimensional search to a single dimension. Nevertheless, in the last few years, other possible roles of the magnetosomes have also been proposed, such as acting as detoxifying agents capable of scavenging metal ions or reactive oxygen species [19, 20].

1.2. Magnetosomes

Magnetosomes can be differentiated in two structures, the mineral magnetic core and the organic envelope that consists of a proteinaceous lipid bilayer membrane [4, 5, 21]. The mineral core presents high chemical purity, being made of magnetite, Fe_3O_4, in most of the species, though some of them synthesize greigite, Fe_3S_4. The size of the magnetic crystals typically ranges between 35 and 120 nm. In this

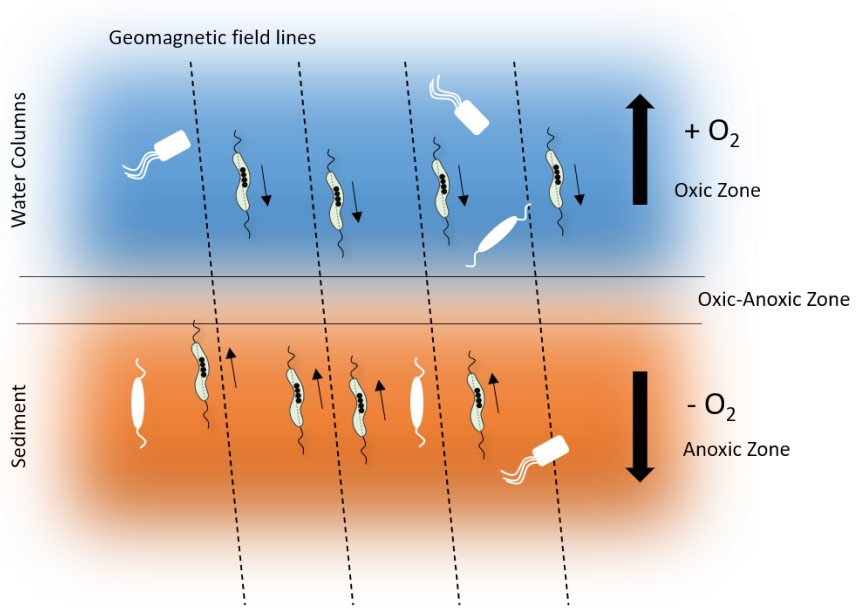

Figure 1.1: *A schematic model of the movement in the water column according to the magnetoaerotactic hypothesis. Unlike other microorganisms (blank), whose movement is random (three-dimensional search), the MTB swim along the geomagnetic field lines (one-dimensional search) towards the oxic-anoxic transition zone.*

diameter range, magnetite magnetic nanoparticles (MNPs) are room temperature stable single magnetic domains [2, 3, 22–24].

1.2.1. Magnetite structure

The structure of magnetite is the crystal structure of the spinel [25], see Fig. 1.2 a. This complex structure is composed by a total of 56 ions per unit cell. The structure consists of oxygen ions that are closely packed in a face centered cubic lattice, and the metal ions, which will be smaller, and occupy the spaces between the oxygen ions. The spaces can be of two types. One is called the tetrahedral site or site A, because it is located in the center of a tetrahedron whose corners are occupied by oxygen ions. The other is called the octahedral site or B site, because the oxygen ions around it occupy the corners of an octahedron. Not all available sites are occupied by metal ions. Only

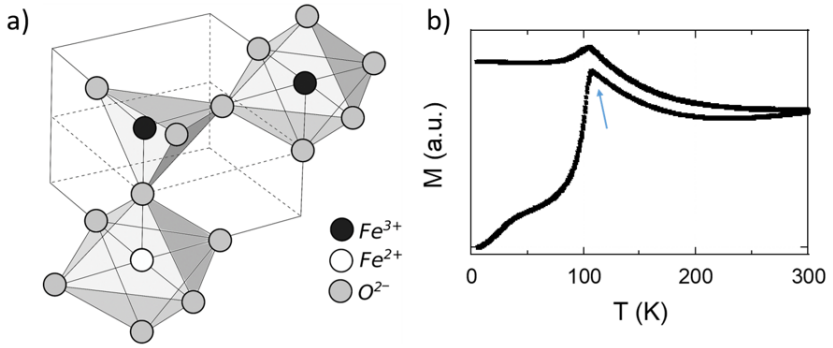

Figure 1.2: *(a) Crystal structure of magnetite. (b) M(T) curve of M. gryphiswaldense measured at 5 mT. The sharp transition observed at 107 K corresponds to the Verwey transition*

one eighth of sites A, that is, 8 of the 64 possible tetrahedral sites are occupied. In the case of the octahedral positions only half of the sites will be occupied, taking then 16 of the 32 possible sites B. In the case of magnetite, the Fe cation arrangement is the following: 8 Fe^{2+} in octahedral sites (Fe_{Oh}), 8 Fe^{3+} in tetrahedral sites (Fe_{Th}), and 8 Fe^{3+} in octahedral ones (Fe_{Oh}).
The Fe^{3+} ions in tetrahedral positions are antiferromagnetically coupled with Fe^{3+} ions in octahedral positions, and therefore, they do not contribute to the magnetic moment. On the other hand, Fe^{2+} ions in octahedral positions are ferromagnetically coupled with Fe^{3+} ions in octahedral sites, through a double exchange mechanism [26], which gives rise to the ferrimagnetic moment of magnetite.
The saturation magnetization, M_s, value is around 90 emu/g at room temperature, while the Curie temperature is 858 K for magnetite. In addition, bulk magnetite presents a characteristic first order magnetic/structural transition at $T_v \sim 120$ K, which drops to 105 K for magnetosomes [27], called the Verwey transition. Upon warming through T_v, the magnetite crystal lattice changes from an insulator monoclinic structure to the metallic cubic inverse spinel structure that persists at room temperature. The presence of this transition is typically associated to a sudden drop in the $M - T$ curves around T_v, as depicted in Fig. 1.2.b. Since the Verwey transition is very sensitive to inhomogeneities and non-stochiometry effects, it can act a as clear cut

indicator of the presence of stochiometric magnetite in our samples.

1.3. MTB diversity

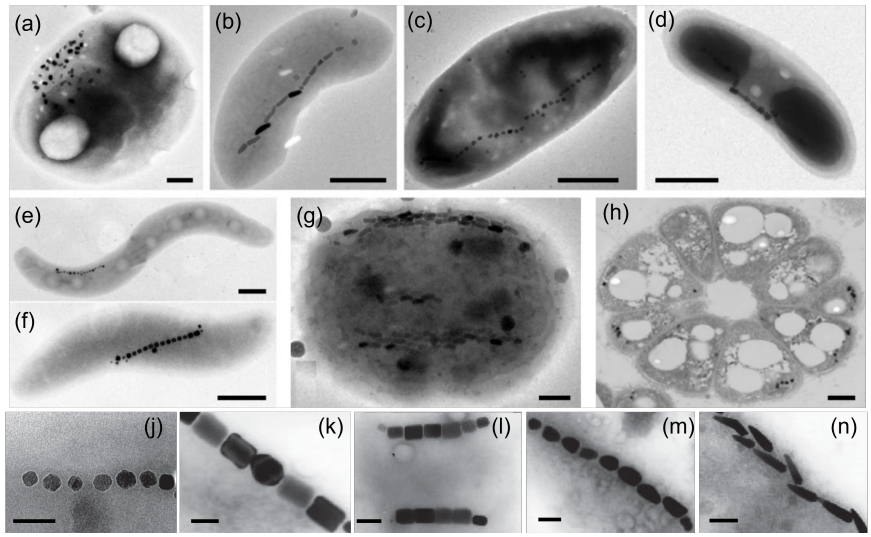

Figure 1.3: *TEM images of different morphotypes of magnetotactic bacteria, i.e: cocci (a), vibroid (b), bacilli (c, d), spirilli (e, f), ovoid cells (g) and multicellular forms (h). The scale bar equals 200 nm (a, g), 500 nm (b, e, f, h) and 1 µm (c, d). Images taken from Bazylinski et al. [5], Lefevre et al. [28] and Araujo et al. [29]. Crystal morphologies and intracellular arrangement of magnetosomes: (j) truncated-octahedral; (k,l) elongated prismatic; (m) tooth-shaped and (i) bullet-shaped. Scale bars: 100 nm. Adapted from from Uebe and coworkers [30] (e-i)*

The term "magnetotactic bacteria" has no taxonomic significance [3] and represents a heterogeneous group of prokaryotes that display great morphological and physiological diversities. The described morphotypes include, see Fig 1.3, cocci, vibroid, bacilli, ovoid, spirillum and even some colonial bacteria, which form multicellular aggregates [5, 31].
The composition, morphology, and size of the magnetosomes are characteristics of each species. This fact clearly reflects that the formation of magnetosomes is driven by a strict genetic control [32]. On the other hand some of the morphologies of the crystals are cube-octahedral (j),

elongated prismatic (k and l), and bullet- or tooth-shaped (m and n), see Fig 1.3 bottom.
MTB are microorganisms difficult to grow and maintain in the laboratory [28], and until now, only a few species have been isolated in axenic culture and deposited bioresource centers. The first isolated species from freshwater sediments were *Magnetospirillum gryphiswaldense*-MSR-1, Fig. 1.4 a, and *Magnetospirillum magneticum* AMB-1, Fig. 1.4 b, [33, 34] in the early 1990s. Both are spirilla and biomineralize truncated-octahedral magnetite crystals. While *M. gryphiswaldense* arrange magnetosomes in a single chain, *M. magneticum* form multiple chains within it. These strains are easier to culture than the rest, and most of the research groups working on MTB focus on them. Alternatively, *Magnetovibrio blakemorei* MV-1 [5], Fig. 1.4 c, is a marine vibrioid to helicoid morphotype that biosynthesizes elongated magnetite nanoparticles with a crystal morphology described as truncated hexa-octahedral. Since the discovery of MTB, the culture media composition and the incubation conditions have been optimized to increase magnetosome production mainly in *M. gryphiswaldense* MSR-1 and *M. magneticum*, while in the case of *M. blakemorei* there is still work to do. In this Thesis, we have worked with these three different species. Since 2011, our group has been working with *M. gryphiswaldense* strain MSR-1, and the culture routes for this species have been optimized. The production of the two other species in the group began in 2018, at the beginning of this Thesis.

1.4. MTB for cancer therapy

Both MTB and magnetosomes have been gaining interest among the scientific community due to their special magnetic and structural characteristics that make them good candidates for nanotechnological applications.
Cancer is one of the most common causes of death worldwide. According to the Global Cancer Observatory [35], only in 2020, around 19.3 million new cases were reported, with a mortality rate higher than 50%, making it the second leading cause of death in the world (only surpassed by cardiovascular diseases). These statistics reflect the need of finding novel strategies and more effective cancer treatments. Cancer treatment methods are mostly based on a combination of surgery, radiotherapy and/or chemotherapy. The most common and useful treatment of cancer is surgery, which permits the bulk of a tumor

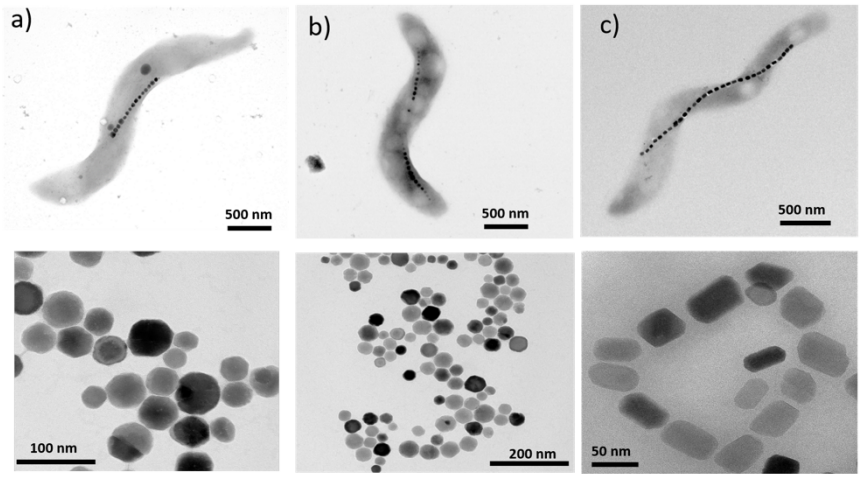

Figure 1.4: *Transmission electron microscopy of (top) (a) M. gryphiswaldense; (b) M. magneticum; (b) M. Blakemorei and their corresponding magnetosomes (bottom).*

to be removed. Unfortunately, in most cases, residual tumor cells remain, which eventually can grow and spread again. Chemotherapy and radiotherapy after surgery attempt to target these cells to prolong patient survival, but these tumor cells can be very resistant to standard therapies. In addition, these therapies can cause strong collateral damage to the human body and deteriorate the patient's health [36]. The new strategies should overcome the known inherent limitations of the standard therapies, such as unspecific targeting, heterogeneous distribution of drugs within the tumour, and non-selective cytotoxicity.

When isolated from the MTB, magnetosomes display a number of potential applications for targeted cancer therapies, such as magnetic hyperthermia, localized drug delivery, or tumor monitoring. The characteristics and properties of magnetosomes for these applications exceed in several aspects those of synthetic magnetic nanoparticles. Likewise, the whole MTB have also been recently considered as promising agents for cancer treatment, taking advantage of their self-propulsion capability provided by their flagella and the guidance capabilities ensured by their magnetosome chain [37].

1.4.1. Magnetosomes as anticancer agents

Magnetic nanoparticles, in general, present a large number of potential clinical applications as diagnostic and therapeutic agents in cancer treatment [38]. Regarding diagnosis, MNPs can be used as contrast agents for molecular imaging and magnetic separation. As therapeutic agents, they can be used, for example, in magnetic fluid hyperthermia (MFH), a technique that aims at debilitating cancer cells by delivering heat to them in a localized way [38–40]. In MFH the heat sources are MNPs attached to, or internalized inside the cancer cells. Under an alternating magnetic field, the MNPs heat up and transmit the heat to the cancer cells. In addition, MNPs can also be used as drug carriers for targeted drug delivery. Precisely, thanks to the nanoparticles being magnetic, they can be directed to specific sites by using magnetic field gradients. In drug delivery, chemotherapeutic agents are attached to the nanoparticles so that they are specifically delivered to the target site. This can substantially reduce the side effects of chemotherapy. In this context, magnetosomes are MNPs that present several characteristics that make them very promising theranostic agents: high crystallinity and regularity; very good reproducibility; high magnetic response that allows easy separation and guidance; a natural lipid bilayer membrane, conferring electrostatic stability and reducing agglomeration; easy functionalization of this lipid bilayer with biological functions for cellular targeting or in situ enzymatic catalysis; and therapeutic action due to the hyperthermic effect exhibited under alternating magnetic fields [41].
The use of magnetosomes for *in vitro* and *in vivo* hyperthermia treatment has already been tested with very encouraging and promising results [42–46]. In a recent work, mice bearing xenografted MDA-MB-231 breast cancer were treated with chains of magnetosomes from *M. magneticum* AMB-1, under a magnetic field of $H = 200$ Oe and $f = 198$ kHz, leading to the total disappearance of tumor after 30 days [47]. In another work, magnetosomes coated with poly-L-lysine were administered to mice with glioblastoma [48]. The mice were exposed to 27 magnetic hyperthermia sessions, each lasting 30 min, using a magnetic field of $H = 270$ Oe and $f = 202$ kHz. All of the mice were alive and apparently cured 350 days after the first injection. In addition, it has been shown that these magnetosomes are capable of maintaining anti-tumor activity even after suffering high levels of degradation inside the tumor cells, which makes them ideal

candidates for long-term hyperthermia treatment [49].
Unfortunately, there are several intrinsic limitations associated to the use of MNPs in general, and magnetosomes in particular, as nanoagents for cancer treatment. These include their limited penetration through biological barriers, poor reaching and targeting capacity, and uneven distribution in the tumor tissue. In fact, in current clinical applications, the administration of the MNPs to the tumor area is mainly limited to direct intra-tumoral injection, which is an invasive procedure, only suitable for well-localized tumors (e.g., prostate) [50]. Ideally, indirect administration methods, such as intravenous or intra-arterial, would be more desirable, but in these cases, generally much fewer MNPs end up reaching the tumor [51, 52]. In order to overcome these difficulties, different alternatives have been proposed in the last few years. Among them, the idea of using biological entities such as viruses and bacteria to interact with tumors has been gaining momentum.

1.4.2. Magnetotactic bacteria as anticancer agents

A further step in this research area consists on using the whole MTB as a biorobot for cancer treatment [37]. In fact, one of the most interesting, promising, and extraordinary approaches for cancer therapy consists on devising nano or micro-robots capable of targeting and destroying cancer cells. To this respect, it has been proposed to take advantage of the innate capacities of biological entities such as viruses or bacteria to interact with other cells and organisms. Moreover, the use of these MTB as nano-robots opens up the possibility of other applications in non-biological media such as in micromanipulation devices and microfluidic channels. For example, Martel *et al.* [53] have shown that swimming MTB can be exploited to manipulate and transport micro- and nanometer-sized objects. Beyond biomedicine, such applications demonstrate that there is a real and exciting prospect of using MTB to open new horizons in environmental technologies.
Bacteria, in general, have a long history in cancer therapy. Already in 1890, Coley *et al.* [54] discovered that some cancer patients recovered after suffering bacterial infections that destroyed the tumors. Over the past century, many genera of bacteria have been investigated as anticancer agents [55]. The effectiveness of bacteria against cancer relies upon their ability to selectively infect and kill the cancer cells *in situ*. Motility is one of the key features of bacterial therapy, since bacteria can actively swim and penetrate deep into the tumor tis-

sue. It happens that tumors display irregular and chaotic vasculature, leading to areas with low oxygen concentration and nutrient limitation [56]. Such hypoxic regions are a perfect niche for anaerobic and microaerophilic bacteria, such as MTB, to perform selective colonization. The mechanism behind this bacterial therapy is still not well understood, but there is evidence indicating that bacteria can perform direct oncolysis and stimulate the immune system [55]. Direct oncolysis is mediated by secreting exotoxins in the tumor area and by competing for nutrients with the cancer cells. In addition, bacterial infections activate the immune system, which targets not only bacteria but also tumor cells. Another advantage of bacterial therapy is that the bacteria can be genetically modified to deliver and/or express specific cytotoxic agents, increasing their effectiveness. In the last years, the FDA has allowed several clinical trials with tumor-targeting bacteria, and these human studies show promising antitumor activities. Moreover, there is a treatment with bacteria which is already standardized in the treatment of bladder cancer (Data can be consulted in https://clinicaltrials.gov).

As described in Fig. 1.5, the perfect bacterial anticancer agents should be able to perform several important functions: target tumors, produce and/or transport cytotoxic molecules, self-propel, sense the local environment, be detectable, etc. In this regard, MTB can be considered ideal candidates to be used as cancer treatment biorobots. Since the magnetotactic bacteria incorporate the magnetosome chain, they can be externally detected, guided, and activated using magnetic fields. Moreover, MTB use the Earth magnetic field guidance in order to find the low oxygen concentration regions in water where they prefer to live. This constitutes another synergistic key point for cancer treatment: since the tumor area is low in oxygen, due to the tumor tendency to rapidly outgrow its blood supply, magnetotactic bacteria are inherently attracted towards these hypoxic regions of the tumor. Therefore, targeting the tumor area with these bacteria can become much easier and more efficient than with MNPs and with other non-magnetotactic bacteria. In addition, preliminary tests have very recently shown that these bacteria can navigate in capillaries and penetrate inside multicellular tumors [57]. Moreover, it has also been shown that once the bacteria have finished their biomedical tasks, they will be eliminated through the feces and urine [58], contrary to what happens with the inorganic MNPs, which tend to accumulate in

the liver and spleen with unknown possible long term toxic effects. One of the first studies on the heating efficiency of the whole MTB was carried out by Alphandery *et al.* in 2011 [47, 59]. In that work, the authors compared the heating efficiency of individual magnetosomes, magnetosome chains extracted from MTB, and the whole MTB. The results revealed a much higher heating efficiency from MTB than from extracted chains and individual magnetosomes. In 2017, Tabatabaei *et al.* [60] proposed the use of MTB with attached commercial SPIONs as heat delivering agents to open the blood–brain barrier for brain tumor treatment. In our group we have recently shown [61] that MTB can be adhered or internalized into human lung A549 carcinoma cells. Cancer cells loaded with MTB were subjected to an alternated magnetic field, AMF, of $H = 400$ Oe and $f = 150$ kHz during 45 min. An immediate effect was observed after the treatment: the growth of cancer cells was drastically slowed down, and at the end of the experiment, the number of living cancer cells was three times lower than the control. This is due to the great heating ability of MTB during MFH. These results will be described in more detail in Chapter 4. Additionally, in parallel, Chen *et al.* in 2016 [62], studied the use of MTB to kill *Staphylococcus aureus* via magnetic hyperthermia. *S. aureus* is a pathogen that causes skin and soft tissue infections, and the authors reported that MTB could effectively kill $\sim 50\%$ of *S. aureus* in the medium.

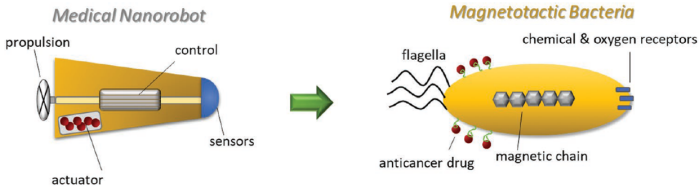

Figure 1.5: *Description of the features that a medical nanorobot must exhibit for cancer treatment and the characteristics of a magnetotactic bacterium functionalized with anticancer drugs.*

1.5. Thesis structure

This Thesis is oriented in three complementary directions: first, the thorough study of the magnetic properties of the magnetosomes and their investigation as model magnetic nanoparticles; second, the magnetic characterization of different species of MTB; and third, the ex-

ploitation of MTB for biomedical applications.

First of all, as commented before, the high quality of magnetosomes makes them a perfect model system, for example, to better understand the relationship between the morphology and magnetic response of MNPs. In addition, an accurate understanding of the magnetic properties of magnetosome chain is an essential point for a proper control, detection, and guidance of the MTB. In Chapter 2, the magnetosomes from *M. gryphiswaldense* will be characterized using macro- and microcharacterization techniques, supported by analytical and modelling methods, in order to assess the influence of the structure, morphology and arrangement of the nanoparticles on their magnetic properties. As a result, we demonstrated that the faceted crystal morphology of the magnetosomes is directly correlated to the magnetic properties of the chains through the magnetic shape anisotropy, and ultimately defines their arrangement in helical-like shaped magnetosome chains. Finally, using a novel nanometric characterization technique, Electron holographic tomography (EHT), we have tried to directly obtain the value and direction of the magnetization of *M. gryphiswaldense* magnetosomes.

On the other hand, we must consider that the size, shape and arrangement of magnetosomes is directly linked to the particular species of bacteria used. Therefore, in Chapter 3 we expand our study to two more species of MTB: *Magnetospirillum magneticum* and *Magnetovibrio blakemorei*. Each of them synthesizes magnetosomes with different sizes and shapes than *M. gryphiswaldense*, and consequently we have studied and compared their magnetic response. In addition, in Chapter 3 we show how the *M. magneticum* growth medium has a great influence on its magnetic properties, and therefore on its future applications.

Finally, in Chapter 4 we study the use of MTB for cancer therapies, in particular, in the field of magnetic hyperthermia, using the previously acquired knowledge to optimize the final *in-vitro* tests. For this study we have focused on the *M. gryphiswaldense* species. Additionally, in order to exploit the use of MTB as remotely controlled microrobots, we have designed and fabricated a laboratory magnetotaxis platform capable of tracking and guiding the MTB in microfluidic environ-

ments, consisting on a 3-axis Helmholtz coil, an optical microscope, and an ad-hoc designed tracking algorithm.

Chapter 2

Magnetosomes as model magnetic nanoparticles or What can we learn from biogenic inorganic nanostructures?

In general terms, today the human hand cannot exceed the quality of the materials produced by nature. Therefore, one of the most innovative and powerful science currents that has emerged in the last few years is to be inspired by nature. Biomimicry is rapidly transforming life on earth [63]. This discipline studies nature's most successful "ideas" over the past 3.5 million years, and adapts them for human use. The results are revolutionizing how new materials are developed and how we carry out different tasks such as: heal ourselves, repair the environment, or feed the world. Biomimicry is the science of applying nature-inspired designs in engineering and invention to solve human problems. It was used to create the first flying machine, inspired by how eagles and owls fly, or architecture like the Eastgate Center in Zimbabwe, which passively self-regulates its internal temperatures mimicking the way termite mounds work [64]. Looking at nature, for example, we can also understand the importance of self-assembly[1]. In

[1]The self-assembly (SA) is a method to fabricate ordered structures. It is a process in which a disordered system of pre-existing components forms an orga-

addition, the delicate control exerted by nature on the manufactured materials allows us to expand our knowledge and discover new possibilities when designing and developing new materials.
To this respect, magnetotactic bacteria exerts a rigurous genetic control on the synthesis of its magnetosome chain [3]. The chain behaves like a compass needle and allows the bacteria to orientate in, and navigate along the geomagnetic field lines, in search of their preferred oxygen concentration regions. The necessary fine control of the magnetosome synthesis implies a high reproducibility in terms of composition, size, shape, and arrangement. This opens the possibility of exploring a very interesting, but frequently ignored, research field regarding magnetotactic bacteria's magnetosomes: their use as ideal magnetic nanoparticle model systems. In fact, the arrangament of the magnetosomes in a chain structure supposes an incomparable opportunity to study the relationship between morphological and magnetic properties on arranged magnetic nanostructures.
Today, due to their outstanding properties, great efforts are being made to build chain-like assemblies of magnetic nanoparticles for different applications, including sensors, nanoreactors and nanomedicine agents [68–70]. In this sense, the magnetosome chain produced by MTB constitutes one of the most fascinating structures to study and take inspiration from. In this Chapter, we will exclusively work with the species *Magnetospirillum gryphiswaldense* MSR-1.

As depicted in Fig 2.1 a, *M. gryphiswaldense* MSR-1 bacteria present spirillum shape (2–5 μm length and 0.5 μm width), with a variable number of magnetosomes forming a chain inside. These magnetosomes are $\sim$ 40–45 nm sized truncated-octahedral magnetite (Fe_3O_4) nanoparticles. In Fig. 2.1 b we show that transmission electron microscopy (TEM) and cryo-tomography techniques reveal that the magnetosome presents faceted morphology, and the [111] axes define the growth directions of the hexagonal faces of the truncated octahedrons. These MTB organize the magnetosomes forming a chain where the hexagonal faces are disposed face to face along the chain direction. Fig. 2.1 c shows the electron diffraction pattern of a [111] zone axis of magnetite. The chain, rather than forming a straight line as has been often assumed, presents a slightly bent helical-like con-

nized structure or pattern as a consequence of specific, local interactions among the components themselves [65, 66]. The most famous example of self-assembly phenomenon is the occurrence of life on Earth [67].

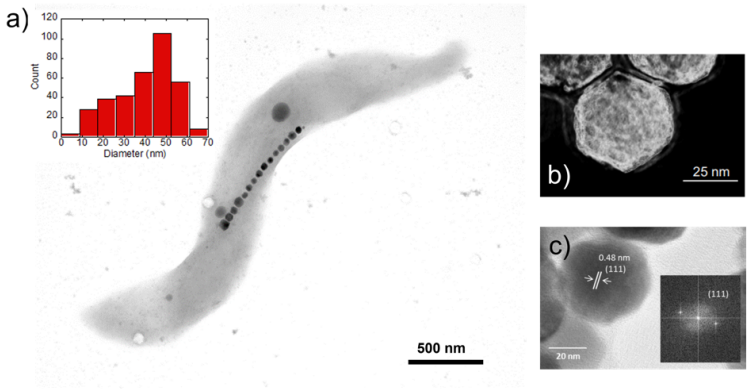

Figure 2.1: *(a) TEM image of M. gryphiswaldense MSR-1 bacteria. A histogram with the size distribution of magnetosomes has been included.(b) Cryoelectron tomography of isolated magnetosomes appeared in [71]. (c) HRTEM and Fourier transform of isolated magnetosomes.*

figuration, as it is shown in Fig 2.2. In Orue *et al.* [71], it was shown that the helical chain configuration is intrincally associated to a 20° tilting of the magnetic moment of each magnetosome out of the chain axis, which corresponds to the [111] easy axis of magnetite. In this Chapter, we will see that the shape anisotropy of the magnetosomes is the key point to understand this magnetic moment tilting. For this, we have employed a combination of standardized magnetic characterization techniques, together with leading experimental techniques in structural characterization such as Electron CryoTomography, ECT, and also modelling techniques such as Finite Element Methods, FEM. Shape anisotropy is of primary importance to understand the magnetic behavior of nanoparticles, but a rigorous analysis in polyhedral morphologies is missing. For this reason, first of all, a model based on finite element techniques has been developed to calculate the shape anisotropy energy landscape for cubic, octahedral, and truncated-octahedral morphologies. In all cases, a cubic shape anisotropy is found that evolves to quasiuniaxial anisotropy when the nanoparticle is progressively elongated. This model will be tested and validated with our model magnetic nanoparticles: magnetosomes, $\sim$ 45 nm truncated octahedral magnetite nanoparticles. As we will see, elec-

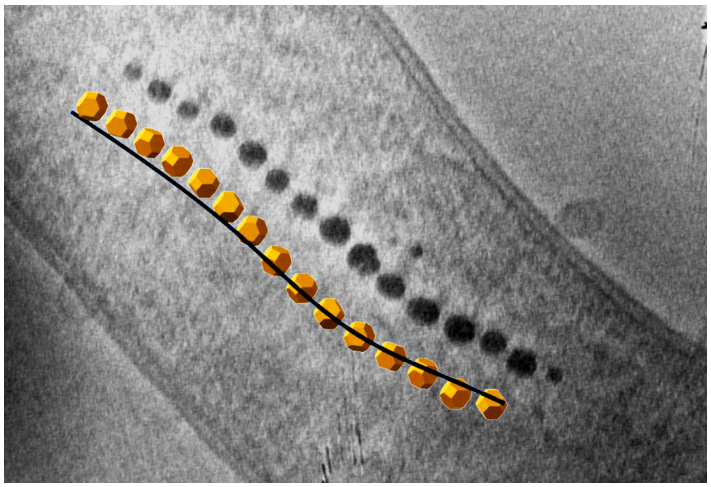

Figure 2.2: *Cryotomography of M. Gryphiswaldense within a simulation of the magnetosome chain appeared in [72] and published in [71].*

tron cryotomography images reveal that these magnetosomes are not ideal truncated-octahedrons but present some extrusion. This deformation gives rise to a quasi-uniaxial shape anisotropy, which is responsible for the 20° tilting of the magnetic moment. Once the shape anisotropy has been accurately determined, a further step would be to directly measure the magnetization vector inside each magnetosome. For this, we have employed a novel characterization technique, Electron Holographic Tomography, EHT, which provides us with a depiction of the induction magnetic field $\vec{B}$ for each magnetosome. Combining magnetostatic modeling with EHT, we demonstrate that in order to precisely determine the magnetization inside magnetosome chain, the exact shape and arrangement of each magnetosome have to be considered.

2.1. Magnetic anisotropy in faceted morphologies

When investigating magnetic nanoparticles intended to be used for any particular application, the role of magnetic anisotropy arises soon as a pivotal question [73]. Important properties of magnetic nanoparticles like the initial magnetic susceptibility, temperature-dependent magnetic relaxation, or the power absorption under AC magnetic

fields depend, to a great extent, on the magnetic anisotropy [2, 74]. The vast majority of modelling efforts found in the literature assume that magnetic nanoparticles, either considered as isolated objects or as part of large clusters, have an intrinsic uniaxial magnetic anisotropy. This anisotropy is often implicitly understood as resulting from the "addition" of diverse contributions such as magnetocrystalline, shape, surface or magnetoelastic effects [66, 75–78].

In general, if particle's size is above certain limits and high crystal purity rules out inner tensions, surface and magnetoelastic effects can be neglected [75, 78–82]. As a consequence, magnetocrystalline and shape anisotropies are expected to be the dominant contributions [73]. However, the relative influence of these two contributions is not usually discussed and many anisotropy calculations work under assumptions that oversimplify this issue [83, 84]. Magnetocrystalline anisotropy mainly depends on the morphology and chemical composition of the material, while shape anisotropy essentially reflects how much the shape of the nanoparticle is deviating from a perfect sphere. The shape anisotropy can be explicitly calculated for ellipsoids and approximately evaluated for prisms, but a rigorous analysis in polyhedral morphologies is far more complicated, being this a research topic of growing interest [85]. In the literature, it is often assumed that the magnetization vector "prefers" to rest along the longest dimensions of the nanoparticle due to the dominant effect of shape anisotropy. However, for strongly faceted magnetic nanoparticles, such as those synthesized by MTB [2, 86] or those obtained via chemical routes [87–89], there is often no clear elongated direction. Improving our understanding of the role of shape anisotropy in magnetic nanoparticles, in general, and in the strongly faceted ones, in particular, is of primary importance in order to develop new hierarchal magnetic nanostructures [90].

In this case, to better understand the importance of shape anisotropy, first we have used electron cryotomography images to accurately reveal the morphology of magnetosomes. Next, we have developed a model to calculate the shape anisotropy energy. And finally, we have validated our model by using the obtained results to simulate, in the framework of the Landau–Lifshitz–Gilbert (LLG) equation, the experimental hysteresis loops measured under an external AC field for *M. gryphiswaldense* bacteria dispersed in water.

2.1.1. Electron cryotomography (ECT) imaging of the magnetosome chain

As has been reported in the literature [91] and shown in Fig 2.1 b, magnesotomes present faceted crystal morphologies. In the case of *M. gryphiswaldense*, the crystal morphology of the magnetosomes is similar to a truncated octahedron (See Fig. 2.3) [71, 92]. In this truncated octahedron, the <001> crystallographic axes define the growth directions of the square faces, while the <111> crystallographic axes correspond to the growth direction of the hexagonal faces. *M. gryphiswaldense* aligns the magnetosomes in a chain according to the <111> crystallographic directions, along the hexagonal faces of the truncated octahedron [91]. In this way, the [111] direction defines the so-called chain-axis. From Transmission Electron Microscopy (TEM) images, it is difficult to obtain information about the specific shape details of these nanoparticles with great accuracy. When we deposit magnetosomes onto a copper grid, they can be found in any orientation, which really complicates the identification of the nanoparticle facet we are working with. Therefore, we have employed Electron Cryotomography (ECT) imaging to obtain more reliable information about the actual shape and orientation of the magnetosomes. This technique allows us to obtain 3D tomograms of the magnetosomes, thereby revealing any shape deviations these nanoparticles may exhibit. Imaging was carried out at CIC bioGUNE | Center for Cooperative Research in Biosciences (Biskay, Spain) in collaboration with Dr. David Gil. Details of sample preparation are specified in Materials and Methods section. In addition, ECT performed on the whole MTB also provides us with an accurate depiction of the arrangement and spatial configuration of the magnetosomes inside the 3D chain [71].

As a reference, in Fig. 2.3 a, on the left, we present the 3D geometric shape of a perfect truncated octahedron, and on the right, we show the corresponding 2D projection. In Figs. 2.3 c–e, we present the reconstructed 3D tomograms corresponding to three different magnetosomes. In addition, below them, we also include images of the slices corresponding to the XY, YZ, and XZ planes, which have been used to make the 3D reconstruction. If we compare these 3D tomograms and slices with the geometric shape of a perfect truncated octahedron, shown in Fig. 2.3 a, we observe that the magnetosomes have indeed a faceted morphology similar to the truncated octahedral one, as previ-

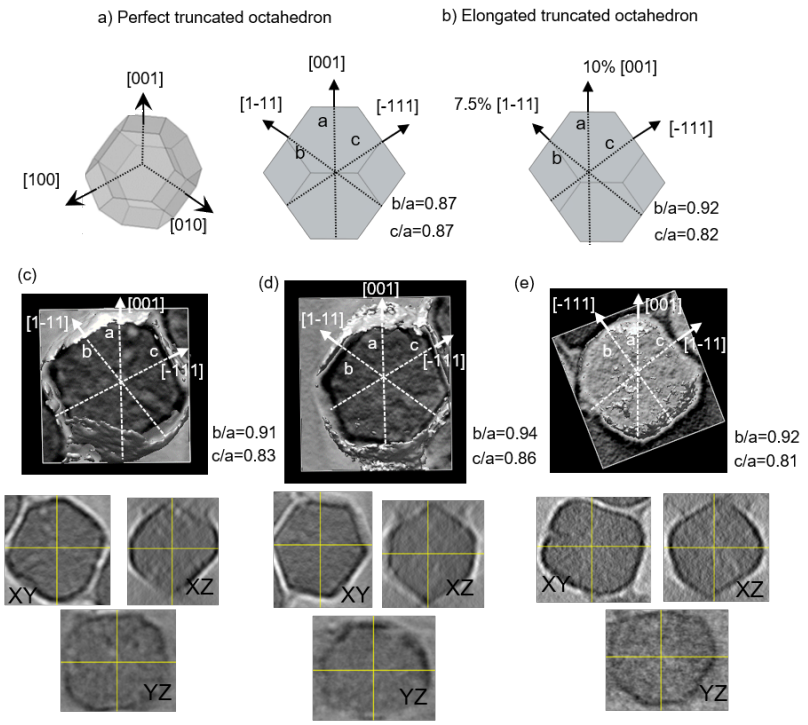

Figure 2.3: *(a) Perfect truncated octahedron. (b) Truncated octahedron with a 10 % extrusion along [1-11] direction, and 7.5 % extrusion along [001] direction. (c–e) Top: reconstructed 3D tomograms of individual magnetosomes. Bottom: central XY, YZ, and XZ slices of the tomograms shown on top.*

ously proposed. However, the ECT images indicate that the shape of our magnetosomes does not exactly correspond to a perfect truncated octahedron, since some deformation is always observed. As shown in Fig. 2.3 a, we can obtain further information about this deformation by measuring the ratio between the distance of two opposing square facets, a, and the distances between two opposing hexagonal facets, either b or c. For a perfect non-deformed truncated octahedron, this ratio should be $b/a = c/a = 0.87$. By analyzing the 3D reconstructed ECT images of magnetosomes, we have identified the square facets, {001}, and the hexagonal ones {111}, Fig. 2.3 c–e. Once we know the specific facets we are working with, we can measure the corresponding distance ratios along these directions within an error of ≈ 0.2 nm. As

depicted in Fig. 2.3, for the three magnetosomes we obtain similar ratios: b/a = 0.92(2), and c/a = 0.82(2). This clearly confirms the deviation of the shape of these magnetosomes from a perfect truncated octahedron. Moreover, these experimental ratios can be accurately explained by a combination of $\approx 7.5\%$ extrusion of one of the {001} square faces and ≈ 10 % extrusion of an adjacent {111} hexagonal face, as shown in Fig. 2.3 b.

2.1.2. Calculation of shape magnetic anisotropy using finite elements method

Once the morphology of the magnetosomes has been accurately determined, we can calculate the associated shape anisotropy. To this respect, we have developed a model, using Finite Elements Method (FEM), to calculate the shape magnetic anisotropy associated to a nanoparticle morphology. Using Comsol Multiphysics [93], we solve an electromagnetic problem on a macroscopic level employing Maxwell's equations subjected to certain boundary conditions. Usually, it is helpful to formulate the problem in terms of the electric scalar potential ϕ, and the magnetic vector potential $\vec{A}$. In our case, there are no currents present, so the equations of interest for us are: $\vec{B} = \nabla \times \vec{A}$ and $\nabla \times \vec{H} = 0$. We solve the model using these expressions together with the constitutive relation: $\vec{B} = \mu_0(\vec{H} + \vec{M})$. In general, a rigorous quantitative analysis of the magnetic shape anisotropy of an object requires the calculation of the magnetostatic energy, E_{magn}, of the given shape, under the constraint that such object is uniformly magnetized in an arbitrary direction. In the simplest case, where the demagnetizing field, $\vec{H}_d$, produced by the magnetization is uniform in the whole object's volume, this magnetostatic energy density is given by:

$$E_{magn} = -\frac{1}{2}\mu_0 \vec{H}_d \cdot \vec{M} = \frac{1}{2}\mu_0 N M^2 \tag{2.1}$$

This applies only to simple geometries like ellipsoids, where H_d can be explicitly calculated, and, as can be seen, E_{magn} is linearly related to the square magnetization by a geometry dependent constant called demagnetizing factor, N [25]. If H_d is not uniform throughout the volume of the object, eqn 2.1 transforms to:

$$E_{magn} = \oint_V -\frac{1}{2}\mu_0 \vec{H}_d \cdot \vec{M}\, dV \tag{2.2}$$

The integral extends to the whole volume of the object and can be numerically calculated by FEM. Just to put the problem into context, it should be recalled that in a typical calculation with macroscopic bodies, the self-demagnetizing action stipulates that magnetization inside the body turns to be nonuniform because the total magnetic field changes from point to point. In contrast, when analyzing single magnetic domain bodies (e.g. magnetic nanoparticles), exchange interaction is assumed to be much higher than Zeeman interaction, so that magnetization can be taken as uniform inside the nanoparticle, which is our first assumption. Given that magnetic poles distribution depends on where the magnetization points to, magnetostatic energy density given by eqn. 2.1 is angle-dependent, and therefore encloses a form of magnetic anisotropy called shape anisotropy.
We will now present the results of performing rigorous numerical calculations of the shape anisotropy in several strongly faceted bodies, and we will then focus on the truncated octahedron morphology characteristic of magnetite single crystals such as magnetosomes.
To calculate the shape anisotropy energy density for a particular morphology, we follow these basic steps:

- The magnetization is kept constant along an arbitrary direction given by unit vector $\hat{u}_m$, $\vec{M}$=M $\hat{u}_m$, where the magnetization module is set as the saturation magnetization of magnetite at room temperature, M = 480 kA $\cdot$m^{-1}.

- The demagnetizing field $\vec{H}_d$ produced by the magnetization is calculated at all points inside the body using Maxwell equations and FEM technique.

- For a single magnetization direction, the total magnetostatic energy density is evaluated as:

$$E_{magn} = \oint_V -\frac{1}{2}\mu_0 \vec{H}_d \cdot \vec{M}\, dV \tag{2.3}$$

- The previous steps are repeated for all orientations of unit vector $\hat{u}_m$, that is, the entire solid angle. Unit vector $\hat{u}_m$, takes the usual form in spherical coordinates as a function of polar and azimuthal angles (θ, ϕ):

$$\hat{u}_m = \sin\theta\cos\phi\hat{i} + \sin\theta\sin\phi\hat{j} + \cos\phi\hat{k} \tag{2.4}$$

This repetition is done in 1° steps, from 0 to 180° for polar angle θ, and from 0 to 360° for azimuthal angle ϕ.
This simulation has been previously validated in ellipsoids, for which shape anisotropy can be easily calculated [94]. Following this procedure, we obtain the energy density landscape, Fig. 2.4, for different particle morphologies. From the analysis of this landscape, we can determine the easy axes, located at the energy minima, and the anisotropy constants, obtained from the energy barrier between the minima and maxima.
To show the potential of the model, first we applied this method for magnetic nanoparticles with regular polyhedral geometry: cubic and octahedral. Truncated octahedral shaped bodies, as our magnetosomes, can be understood as the result of combining a cube and an octahedron in different proportions. Therefore, it is useful to compare the shape anisotropy of these morphologies with the truncated octahedron, which lies midway between both, and is the most probable crystal growing shape for magnetite [95]. Fig. 2.4 shows the magnetostatic energy density landscape calculated by eqn. 2.3 for the three mentioned morphologies: cube (C), truncated octahedron (TO), and octahedron (O).

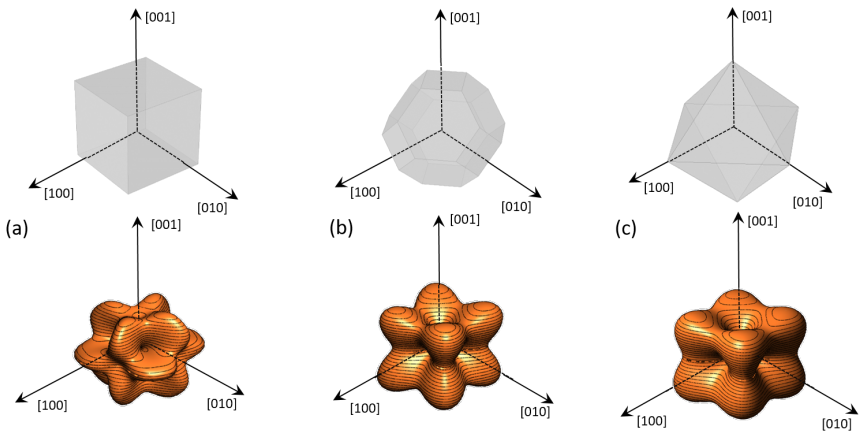

Figure 2.4: *Magnetostatic energy density of the cube (a), perfect truncated octahedron (b) and perfect octahedron (c).*

In the case of the cubic morphology, the absolute energy minima are located at the <111> directions, along the cube diagonals, but 6 additional local minima can be found along the <100> directions

(perpendicular to square faces), giving a total of 8 + 6 = 14 non-equivalent energy minima or, conversely, 14 easy magnetization axes. Note that in this case the longest dimension is along the diagonal line of the cube.

Two anisotropy constants can be calculated, as explained before, from the energy barrier between the absolute <111> minima and the hard axes <110>, $K_1 = 5.2$ kJ·m^{-3}, and between the local <100> minima and the hard axes <110>, K_2 = -52 kJ·m^{-3}. The shape anisotropy energy density for the cube, C, can be expressed in terms of the general cubic expansion in powers of the direction cosines of the magnetization [25], taking K_1 and K_2 as the first and second anisotropy constants:

$$E_{cube} = K_1(\alpha_1^2\alpha_2^2 + \alpha_2^2\alpha_3^2 + \alpha_1^2\alpha_3^2) + K_2(\alpha_1^2\alpha_2^2\alpha_3^2) + ... \qquad (2.5)$$

For the other two regular polyhedrons of Fig. 2.4 b,c, TO and O, the easy axes correspond to the <100> directions, which are perpendicular to square faces in the TO and along the octahedron vertices in the O. In these cases, only absolute minima are found in <100> directions. The hard axes correspond to the <111> directions. From the energy barrier between these minima and the maxima in <111> directions, we get an anisotropy constant $K_1 = 6.7$ kJ·m^{-3} for O, and $K_1 = 1.5$ kJ·m^{-3} for TO. As expected, given that the octahedron is strongly nonspherical (higher aspect ratio), the anisotropy constant for the O is much higher than for the TO.

At this point, it must be reminded that TO shape is the basic morphology for magnetosomes of *M. gryphiswaldense*. Therefore, when magnetocrystalline anisotropy of magnetite, with K_{crys}= -10/-11 kJ·m^{-3} and easy axes <111>, is combined with TO shape anisotropy, with $K_{sh} = 1.5$ kJ·m^{-3} and easy axes <100>, the magnetosome is, in principle, expected to retain a negative cubic anisotropy character but with reduced energy barriers. However, in real cases, including magnetosomes in bacteria and chemically synthesized magnetite nanoparticles, a magnetic behavior indicative of cubic anisotropy is hardly observed [96]. This can be associated to distortions of the perfect TO shape. Obviously, non-regular shapes are much more likely in reality, and in this way, the resultant shape anisotropy will end up being uniaxial rather than cubic. The central question is how much "distortion" is needed to overcome the highly symmetric cubic behavior, and give rise to an uniaxial anisotropy.

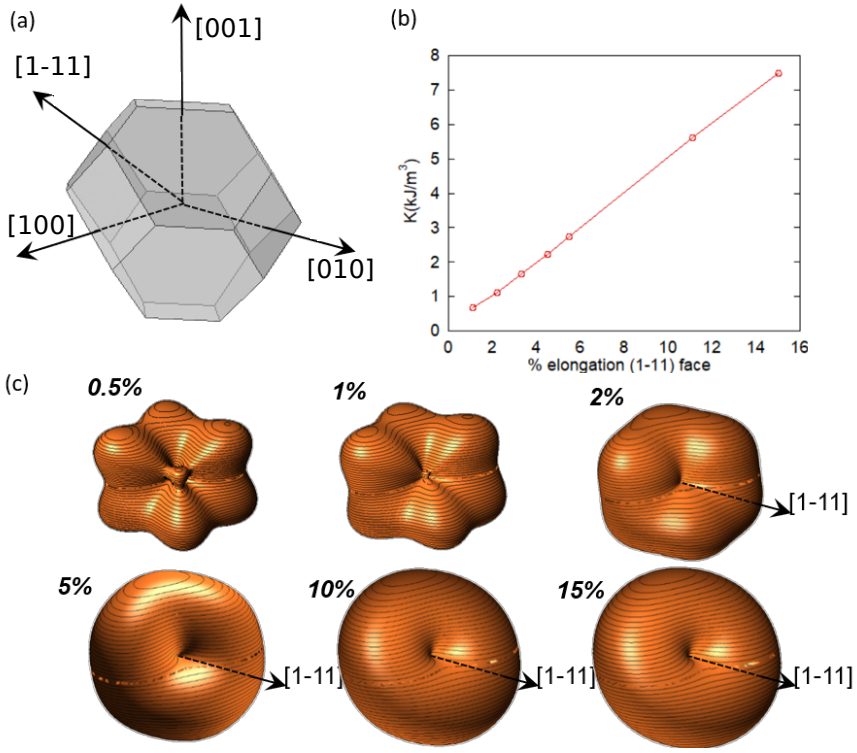

Figure 2.5: *(a) Truncated octahedron with an extrusion directed along the [1–11] direction. (b) Shape anisotropy energy landscape for different extrusion values, from 0.5 to 15 %. (c) Linear relationship between the elongation and the shape anisotropy constant.*

As we mentioned before, in the case of *M. gryphiswaldense*, it has been established that each magnetosome in the chain possesses its own uniaxial anisotropy, with a well-defined easy axis that should be oriented close to the chain direction, in order to maximize the chain net magnetic moment [71] [91] [97]. Given that the chain axis direction corresponds with the crystallographic <111> direction of each magnetosome, the first option to analyze the effect of the distortion is to explore what happens to the shape anisotropy energy landscape when lengthening the <111> directions of a TO. To this purpose, we have calculated the surface energy for a TO in which one of the <111> directions is progressively extruded while keeping the relative orientation of all faces unchanged, Fig. 2.5a. The corresponding en-

ergy landscapes are represented in Fig. 2.5 b.
As we increase the extrusion along the [1–11] direction, we can clearly see how we move from a cubic energy landscape to a quasi-uniaxial landscape with the energy minima located along the [1–11] axis. As indicated in Fig. 2.5 c, there is a linear relationship between the elongation along the extruded direction and the value obtained for the shape anisotropy constant.
At this point, we would like to remark that:

1. Extrusions as small as 2 % already give rise to this single easy axis anisotropy.

2. With increasing extrusion, the energy landscape acquires a toroidal-like shape, which would in principle suggest uniaxial anisotropy, but the cubic contribution to the shape anisotropy cannot be neglected, and hence we are referring to it as a "quasi-uniaxial anisotropy".

Therefore, the calculated shape anisotropy energy density for a deformed TO can be approximated to the following analytical function:

$$E_{elong.TO} = -K_{sh-u}(\hat{u} \cdot \hat{u}_m)^2 + K_{sh-c}(\alpha_1^2\alpha_2^2 + \alpha_2^2\alpha_3^2 + \alpha_1^2\alpha_3^2) \quad (2.6)$$

where $\hat{u}_m$ is the unit vector director of the magnetization $\vec{M} = M\hat{u}_m$. The first term corresponds to the uniaxial anisotropy, and is related to the extrusion in the direction of $\hat{u}$ (in this case $\hat{u}$ is along the [1–11] direction), and the second term corresponds to the underlying cubic anisotropy, characteristic of the unextruded TO, being K_{sh-c}= 1.5 kJ·m^{-3}. Depending on how much we elongate the nanoparticle model, K_{sh-u} can take different values, as shown in Fig. 2.5 c.
Therefore, up to this point, we have shown the characteristics of the developed finite element model for the calculation of magnetic shape anisotropy in faceted nanoparticles. Before continuing, we would like to remark that the procedure for the calculation of the shape anisotropy described here in the particular case of truncated octahedral magnetosomes can be applied to any other morphology. We could simply do this by drawing the particle model and using our standardized calculation model. Furthermore, through the calculations made and the energies obtained, we have managed to formulate the analytical expression that would model the shape anisotropy of an elongated truncated octahedron (equation 2.6). A similar expression

could be obtained analogously for any other proposed morphology. In general, this type of analytical expressions are essential for better understanding and modeling the magnetic behavior of different magnetic nanoparticles.

2.1.3. Shape anisotropy of *M. gryphiswaldense* magnetosomes

Now we are going to apply the described FEM model to calculate the shape anisotropy energy for the magnetosomes of *M. gryphiswaldense* MSR-1, incorporating the extrusions experimentally observed by ECT, 7.5% along the [001] direction and 10% extrusion directed along [1–11] direction, as it is shown in Fig. 2.6 a.

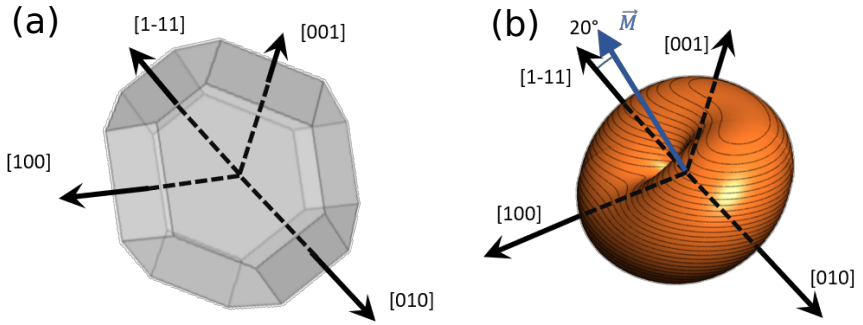

Figure 2.6: *(a) Truncated octahedron with 10% extrusion directed along [1–11] and 7.5% along the [001] direction. (b) Shape anisotropy energy density landscape of the magnetosome system calculated by FEM method.*

As shown in Fig. 2.6 b, for a truncated octahedron with 10% extrusion directed along [1-11] and 7.5% along the [001] direction, the effective quasi-uniaxial easy axis lies near 20° tilted from the [1–11] direction (this would be the direction of $\hat{u}$ in eqn. 2.6), and the shape anisotropy constant values obtained to analytically reproduced the shape anisotropy energy using eqn. 2.6 are $K_{sh-u} = 7$ kJ·m^{-3} and K_{sh-c}= 1.5 kJ·m^{-3}. Again, all this information is directly obtained from the shape anisotropy energy density landscape calculated by FEM method. These 20° of deviation that we find in the magnetosome shape anisotropy perfectly fit with the tilting of the magnetization proposed in [71], as had been commented before. In that work, it is

stated that rather than straight lines, magnetosomes are arranged in helical-shaped chains. This geometry stems from the fact that the effective magnetic moment of individual magnetosomes is 20° tilted out of the chain axis.
Therefore, we can conclude that using our FEM model, we have been able to calculate the shape anisotropy energy of the magnetosomes, to confirm the origin of the 20° tilting of the magnetization vector. From these results, we can ascertain that although it is difficult to understand the exact way in which the magnetosome is biomineralized so that the chain structure is formed, what is certain is that, during the biomineralization process, the *M. gryphiswaldense* bacteria stretch two of the magnetosome faces to generate a magnetic anisotropy that tilts out the magnetic moment, facilitating in this way the subsequent formation of the helical magnetosome chain. Thus, the magnetosome chain matches the spirillum-shaped morphology of the bacterium. In the end, the net magnetic moment points along the chain axis but this magnetic configuration helps accommodating the magnetosome chain to the helical shape of the microorganism.

2.2. AC Magnetometry model

The last step in our analysis is to corroborate the validity of our model by using the calculated shape anisotropy energy to reproduce experimental data. In particular, we have focused on the simulation, within the framework of the Landau-Lifshitz-Gilbert (LLG) equations, of the AC hysteresis loops measured for *M. gryphiswaldense* bacteria dispersed in water. The energy density landscape of each magnetosome in the chain can be reproduced by the following equation:

$$\begin{aligned} E_i = E_{crys} + E_{shape} + E_{dip} + E_{Zeeman} = \\ K_{crys}(\alpha_1^2\alpha_2^2 + \alpha_2^2\alpha_3^2 + \alpha_1^2\alpha_3^2) - \\ K_{sh-u}(\hat{u}_m \cdot \hat{u}_{m,i})^2 + \\ K_{sh-c}(\alpha_1^2\alpha_2^2 + \alpha_2^2\alpha_3^2 + \alpha_1^2\alpha_3^2) - \\ \sum_{j\neq i}^{N} \frac{\mu_0 M^2 V}{4\pi a^3}[3(\hat{u}_{m,i} \cdot \hat{a}_{i,j})(\hat{u}_{m,j} \cdot \hat{a}_{i,j}) - (\hat{u}_{m,i} \cdot \hat{u}_{m,j})] - \\ \mu_0 MH((\hat{u}_H \cdot \hat{u}_{m,i}) \end{aligned} \tag{2.7}$$

The first term, E_{crys}, corresponds to the magnetocrystalline anisotropy energy density of magnetite, and is given by the typical cubic anisotropy

expression. Since magnetosomes are pure magnetite crystals, we have used the expected bulk value for the magnetocrystalline anisotropy constant K_{crys} = -10 kJ·m^{-3} [25]. The second term, E_{shape}, corresponds to the shape anisotropy energy density of the magnetosome (eqn. 2.6), being $K_{sh-u} = 7$ kJ·m^{-3} and $K_{sh-c} = 1.5$ kJ·m^{-3} as we explained before. In this case, $\hat{u}_{m,i}$ is the unit vector director of the magnetization $\vec{M} = M\hat{u}_{m,i}$, and $\hat{u}$ corresponds to the direction of effective quasi-uniaxial easy axis, which lies 20° tilted out of the [1-11] direction, as explained before. The third term, E_{dip}, corresponds to dipolar energy due to interactions between magnetosomes inside the chain. Electron cryotomography performed on the whole bacteria allows us to determine the XYZ positions and relative orientations of each magnetosome inside the chain, see Fig. 2.7 a. In this third term, $\hat{a}_{i,j}$ is the unit vector along the line joining particles i and j, located at a distance given by $a = 60$ nm, and $V = 381 \cdot 10^3$ nm^3 is the volume of each particle, considering a mean size of 45 nm, the same for all for simplicity, see Fig. 2.7 a. Finally, the last term, E_{Zeeman}, corresponds to the Zeeman energy, where H is the alternating magnetic field.
Then, the AC hysteresis loops can be modeled solving the quite general Landau–Lifshitz–Gilbert equation for the magnetization dynamics of a single domain subjected to an arbitrary effective field, $\vec{B}_{eff} = -(1/M) \cdot \partial E/\partial \hat{u}_m$, being E is the energy density of a single nanoparticle and:

$$\frac{d\hat{u}_m}{dt} = \gamma \hat{u}_m \times \vec{B}_{eff} - \alpha \hat{u}_m \times \frac{d\hat{u}_m}{dt} \tag{2.8}$$

In this equation $\alpha = 0.05$ is the so-called Gilbert damping constant (dimensionless constant) [98, 99], $\gamma = 2$ is the gyromagnetic ratio of free electron and $\vec{M} = M\hat{u}_m$ is the magnetization. Some limitations should be noted. In this model thermal fluctuations are completely neglected ($T = 0$ K), so it is expected to work fine when magnetization is anchored to energy minima. In our case, since magnetosomes are particles with a mean size $\sim$ 45 nm, the anisotropy energy, KV, is much higher than the thermal energy, K_BT, at 25° C, and, consequently, the magnetization is strongly anchored to energy minima. Moreover, as we work with energy densities, the volume of particles only enters explicitly the LLG model through the dipolar interactions, so this approach is mostly size-insensitive. In Fig. 2.7 b, we show the experimental AC hysteresis loops of bacteria dispersed in water, measured at 300 kHz, and the simulated hysteresis loops, using

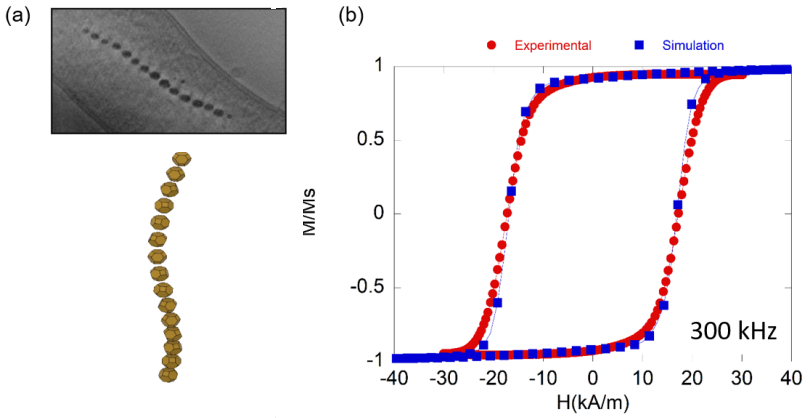

Figure 2.7: *(a) Up: ECT image and down: 3D reconstruction of the chain of magnetosomes of M. gryphiswaldense obtained from [71]. (b) AC hysteresis loops, M vs. H, measured for bacteria dispersed in water (25°), and simulated hysteresis loops obtained from solving eqns 2.7 and 2.8.*

eqns. 2.7 and 2.8. As can be observed, the simulated hysteresis loops nearly overlap the experimental ones, indicating that the model we have developed to determine the shape anisotropy energy landscape allows us to accurately reproduce the magnetic behavior of the chain of magnetosomes in *M. gryphiswaldense*.
It must be noted that in Marcano's doctoral thesis [72], the experimental DC hysteresis loops of 2D and 3D arrangements of *M. gryphiswaldense* bacteria were accurately reproduced by setting the magnetic moment at 20° with respect to the chain axis and values for the anisotropy constants of K_c = -11 kJ·m^{-3} and K_{uni} = 12 kJ·m^{-3}. In this case, a Stoner-Wohlfarth based model was used and dipolar interactions were considered as a part of the uniaxial effective anisotropy constant. Despite the great differences that exist between both models[2], these results could indicate that the value of the dipolar interactions density energy may be around of E_{dip}= 5 kJ·m^{-3}.
Although, with our previous calculations, we have phenomenologically explained the magnetic behavior of the magnetosome chain, in next section we are going to try to *experimentally* determine the magnetization value and direction for the magnetosomes inside the chain, by

[2]Stoner-Wohlfarth based model will be explained in detail in next chapter

using a combination of Electron Holography (EH), Electron Tomography (ET) and FEM simulations.

2.3. Electron Holographic Tomography (EHT) of the magnetosome chain

In order to investigate the magnetic properties of the magnetosome chain in *M. gryphiswaldense*, we have employed a novel technique: Electron Holographic Tomography (EHT). The measurements and experimental analysis were carried out by Dr. Daniel Wolf at the Institute of Structural Physics, Technische Universitat Dresden (Germany). The technique receives its name because it combines Electron Holograpy (EH) with Electron Tomography (ET).
Using Electron Holography (EH), the magnetic induction can be measured in projection by means of the phase of the electron wave at the nanoscale [100–102]. However, in most cases, the presence of stray fields, which depend on the morphology and also the arrangement of nano-structures, prohibit a direct interpretation of the phase image in terms of magnetization vector [103, 104]. In general, a separation of the magnetization from stray fields in phase images requires to determine the exact shape and arrangement of the studied structure, which can be obtained by ET and also to use magnetostatic simulations. Therefore, the idea in our EHT study is to first use EH to obtain the magnetic induction value of an individual magnetosome and then reconstruct the magnetization value by using the morphology of the magnetosome obtained by ET. For this, we have employed a magnetostatic FEM model, which relates both results through an optimization algorithm.
In Fig. 2.8 a we present a TEM image of *M. gryphiswaldense* magnetosome chain, while Fig. 2.8 b show the ET reconstruction of this chain. For this study, we have focused the EHT experiment on three NPs forming a part of the complete magnetosome chain, labelled as: NP 3, NP 4, and NP 5, in the corresponding TEM and ET reconstructed images, shown in Fig. 2.8 a, b. In Fig. 2.8 c, we show High Resolution Transmission Electron Microscopy (HR-TEM) images of the selected magnetosomes and their corresponding Fourier Transform. These have allowed us to identify the [111] direction of each magnetosome, which has been schematically drawn in Fig 2.8 d. The corresponding vector components are indicated in Table 2.1. We see that the crystallographic <111> directions of each magnetosome

inside the chain are not perfectly aligned along the chain axis, as has been typically assumed [105, 106]. The <111> directions are separated $\sim 10^{\circ}$ between NP 3 and NP 4, and $\sim 3^{\circ}$ between NP 4 and NP 5. Nevertheless, since these differences are quite small, nearly within the technique resolution, we cannot discard that they could be related to some artifact introduced during sample preparation, although it is true that similar deviations have been previously reported in other MTB species [107]. This slightly tilted arrangement could favor the accommodation of the entire magnetosome chain, like beads in a string, in the spiral-shaped microorganism [71]. Once we have

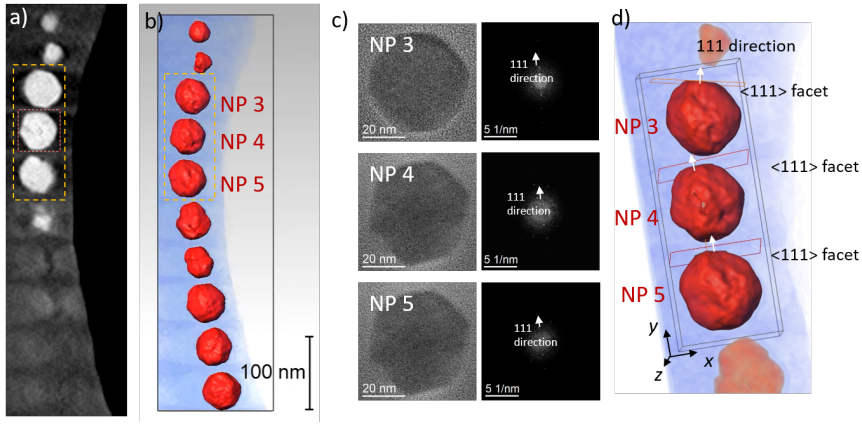

Figure 2.8: *(a) Slice of a tomograph of the chain of magnetosomes inside M. gryphiswaldense MSR-1 bacteria. (b) ET reconstruction of magnetosomes and their chain assembly. (c) HR-TEM images of the magnetosome and their Fourier Transform Images showing crystallographic orientation of NPs within the assembly. (d) ET reconstruction of the three selected NPs showing their corresponding <111> facet direction.*

determined the crystallographic orientation of each magnetosome inside the chain, we have used off-axis electron holography (EH), to investigate the magnetization of the magnetosome chain under virtually magnetic field free conditions. EH allows us to experimentally measure the $\vec{B}$ magnetic field direction of each magnetosome without disturbing the chain configuration during the measurement. This represents a huge advantage in comparison to other magnetization measurement techniques. Moreover, since the magnetization vector

$\vec{M}$ is collinear with $\vec{B}$, EH also can provide the direction of the magnetization. In this way, we can compare this direction with the previously obtained [111] direction to determine the deviations between both vectors for each magnetosome. In Fig. 2.9 a, we have included two different projections of the magnetosomes (XY and ZY) together with their out-of-plane magnetic field component (represented by a color scale) as obtained from EH. For convenience, we have also depicted with arrows the XY component of $\vec{B}$ at different points inside and outside the magnetosomes. From these measurements, we can obtain the average magnetic field vector $\vec{B}$ direction for each one of the selected magnetosomes: NP 3, NP 4, and NP 5, as summarized in Table 1. Interestingly, for all magnetosomes, the average $\vec{B}$ field direction (and therefore, the average $\vec{M}$ direction), is slightly deviated from the corresponding <111> direction. Therefore, not only the magnetosomes are not perfectly aligned along the same direction, as we saw before, but also their magnetization vectors $\vec{M}$ are slightly deviated from the crystallographic <111> direction of each individual magnetosome. This supports our previous results which indicated that in the helical-like shaped arrangement of magnetosomes in these bacteria, the effective magnetic moment of each individual magnetosome should be slightly tilted out of the [111] crystallographic easy axis of magnetite due to the deformation of the truncated octahedral shape of magnetosomes. Of course, this deviation can vary from one magnetosome to another, depending on their shape distortion. This is precisely shown in Table 2.1, in which the angle between average magnetic field $\vec{B}$ and the [111] axis for each magnetosome presents values between 8.5° - 19.7°. Nevertheless, we must take in account that the experimental technique has an associated error of $\sim 5°$ in the determination of this angle.

2.3.1. Magnetostatic modelling

In order to finally obtain the magnetization value (M_s) for each magnetosome, we have compared the experimentally obtained B values (B_{exp}) with those reproduced using FEM simulations (B_{calc}). In addition, we have assumed that $\vec{B}$ and $\vec{M}$ vectors point along the same direction.

For this, first we import the ET reconstruction of the magnetosome chain to our FEM program: Comsol Multiphysics [93]. In the present magnetostatic model, we have used the experimental 3D reconstruction performed through ET images shown in Fig. 2.8 d. This is

	<111 >direction	*Average* $\vec{B}$	*Angle between both vectors*
NP1	$\vec{n} = \begin{pmatrix} 0.196 \\ 0.980 \\ 0 \end{pmatrix}$	$\vec{B} = \begin{pmatrix} 0.036 \\ 0.247 \\ 0.01 \end{pmatrix}$	19.7
NP2	$\vec{n} = \begin{pmatrix} -0.060 \\ 0.991 \\ -0.120 \end{pmatrix}$	$\vec{B} = \begin{pmatrix} -0.025 \\ 0.287 \\ -0.035 \end{pmatrix}$	8.5
NP3	$\vec{n} = \begin{pmatrix} 0 \\ 0.993 \\ -0.122 \end{pmatrix}$	$\vec{B} = \begin{pmatrix} -0.052 \\ 0.274 \\ -0.06 \end{pmatrix}$	11.5

Table 2.1: *Summary of Electron Tomography and Holography results*

a fundamental point since it allows us to accurately reproduce the shape and relative position of the NPs in the simulated magnetostatic model. In the past section, we have shown that the shape of magnetosome has a huge influence on the final properties of the whole bacteria. Importing the ET reconstruction to our FEM program is a great advantage in order to obtain the most realistic values of $\vec{B}$.
Once we have imported the reconstruction of each magnetosome to our model and set the direction of the $\vec{B}$ vector, we try to obtain the M_s value (set as a fitting parameter) by minimizing the following expression:

$$\frac{1}{V_{NP}} \oint_V \left(\frac{B_{calc}}{B_{exp}} - 1\right)^2 \tag{2.9}$$

where V_{NP} is the volume of the nanoparticle, B_{calc} is the value of the field calculated by FEM, which depends on the fitting value of M_s, and B_{exp} is the experimentally obtained magnetic field value (e.g. $B_{exp} = 0.293$ T for NP 4). In Fig. 2.9 a we show the XY and YZ projections of B_{exp}, as obtained from EH technique, while in Fig. 2.9 b, we present the XY projection of the B_{calc} for the 3 selected magnetosomes. As depicted, B_{calc} is non-uniform because the total demagnetizing field changes from point to point. This can also be seen in Fig. 2.9 c, in which we present a 3D depiction of B_{calc} for several ZY slices of the NP 4. The M_s value obtained for studied magnetosome is much lower than expected. For example, for central magnetosome (NP4) M_s=318 kA/m. This is a surprising result as it

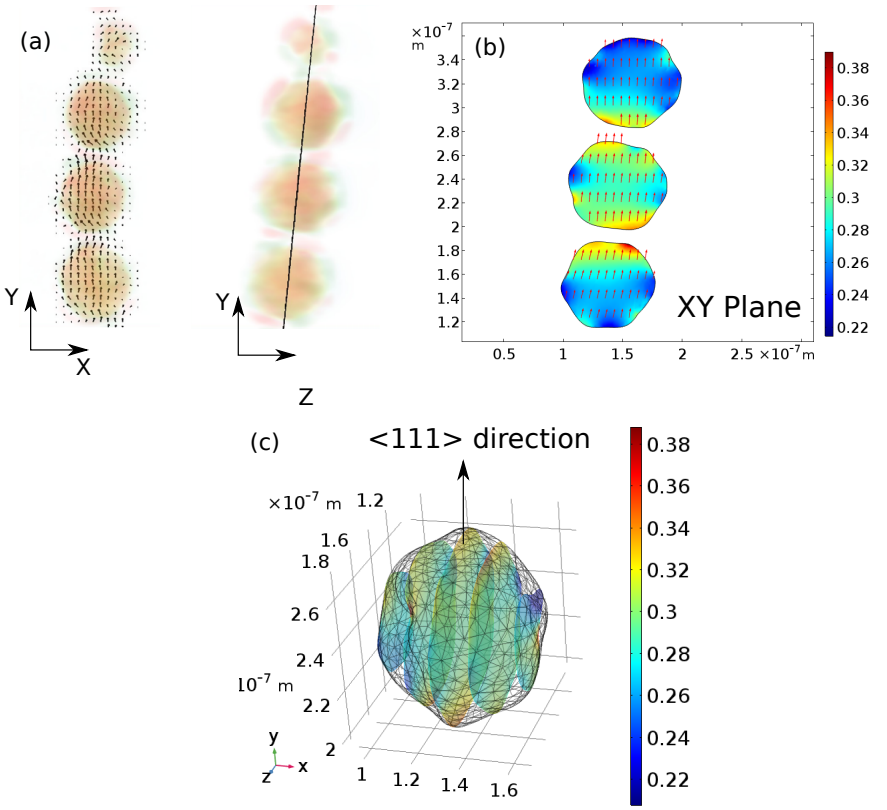

Figure 2.9: *(a) XY and YZ projections showing the $\vec{B}$ vector plot reconstructed using EH. The arrows represent the XY component of $\vec{B}$. (b) XY projection of the B vector plot and the $\vec{B}$ field obtained from simulations. (c) 3D view of 5 ZY slices of the B field calculated within the particle.*

represents only 66% of the expected M_s value for bulk magnetite at room temperature (480 kA/m). From our inquiries with Dr Wolf, this mismatch could be related to some issues with the way in which the gradient in the experimental EHT technique, but further work will be needed to pinpoint and correct this issue. Despite not having been able to obtain a reliable value for the M_s module of our magnetosomes at this moment, we would like to stress that EHT is a very promising and powerful technique which can provide high resolution information about the magnetic field generated by individual nanoparticles. This

experimental information, together with our FEM simulations, should allow us to accurately determine the magnetization vector for each magnetosome in the magnetosome chain. In addition, these results also showcase the potentiality of magnetosomes to be used as standard testing samples in novel experimental techniques such as EHT.

2.4. Summary

In this Chapter, we have proven that shape anisotropy plays a crucial role in the configuration and magnetic behavior of faceted nanoparticles, such as magnetosomes synthesized by *M. gryphiswaldense*. Moreover, our results indicate that the chain of magnetosomes constitutes a perfect playground to check the importance of shape anisotropy in hierarchical nanostructures. We have designed a model to calculate the shape anisotropy energy density for a particular morphology of the nanoparticle using a Finite Element Methods approach. In the case of magnetosomes, their morphology has been analyzed by using electron cryotomography, revealing that it slightly deviates from a perfect truncated octahedron, due to $\sim$ 7.5% extrusion of one of the [001] directions and $\sim$10% extrusion of an adjacent [111] direction. This deformation defines the shape anisotropy energy landscape of the magnetosome, with a unique quasi-uniaxial character, arising from the competition between the cubic shape anisotropy associated to the truncated-octahedral shape, and an uniaxial shape anisotropy associated to the deformation. We have validated our calculations by using the analytical expression of the shape anisotropy obtained by finite elements to simulate, within the framework of the Landau–Lifshitz–Gilbert model, the experimental AC hysteresis loops measured for these magnetotactic bacteria at 25°C.
Finally, we have shown the potential of EHT technique, which has allowed us to experimentally observe the deviation angle between <111> direction and the magnetic moment of magnetosome. Moreover, we have shown that the combination of EH and ET with a FEM optimization method should eventually allow us to reproduce the magnetization of each individual magnetosome in an accurate and precise way, once the mentioned issues are solved.

Materials and Methods

Electron Cryotomography Imaging (ECT)

ECT was carried out at CIC bioGUNE | Center for Cooperative Research in Biosciences (Biskay, Spain) in collaboration with Dr. David Gil. The images were obtained on whole bacteria and isolated magnetosomes, both mixed with 10 nm Au nanoparticles (Aurion®BSA gold tracer) employed as markers. The mixture was deposited onto a TEM grid and frozen-hydrated following standard methods, using a Vitrobot Mark III (FEI Inc., Eindhoven, The Netherlands). The cryotomographic acquisition was performed with a JEM-2000FS/CR field emission gun transmission electron microscope (Jeol, Europe, Croissy-sur-Seine, France) working at 200 kV. Different single-axis tilt series images were acquired using an UltraScan 4000, 4k × 4k CCD camera (Gatan Inc., Pleasanton, CA, USA), over a tilt range of ±64° with 1.5° increments, using the data acquisition software SerialEM. [108]. CCD Images were collected at a magnification of 25 000× and a binning factor of 2 (2048 × 2048 pixel micrographs), producing a pixel size of 0.95 nm. The images in each tilt-series were obtained under the same underfocus and lowdose conditions. For the alignment and 3D reconstruction, we used IMOD software [109]. We employed the Au markers during the alignment process, and 3D reconstruction was carried out by weight back-projection and using a Simultaneous Iterative Reconstruction Technique (SIRT). The obtained tomograms were visualized with ImageJ [110] as a sequence of cross sectional slices in different orientations. Tomograms were then processed using a median filter and visualized as 3D electron density maps using UCSF Chimera software [111].

AC Magnetometry

The AC hysteresis loops were measured in a homemade AMF magnetometer available at the University of Basque Country, UPV/EHU (Biskay, Spain) previously described by Garaio *et al* [39]. It consists of an air-core inductor part of a resonant circuit fed by a power amplifier. The dynamic magnetization, M_t, is measured by a pick-up coil system composed of two coils wound in opposite directions. The signal is filtered using a low-pass filter with the cutoff frequency at 3 MHz. For the AC hysteresis loops measurements the bacteria were dispersed in deionized water. The magnetite mass concentration was c $\sim$0.2 mg $\cdot$ ml^{-1}, as determined from saturation magnetization, measured using

the VSM, and considering as reference the saturation magnetization value of 92.3 A $\cdot$ m^2 $\cdot$kg^{-1},corresponding to pure magnetite. The dynamic hysteresis loops were measured at room temperature (25 °C) at selected frequencies, 302 kHz, and with an applied magnetic field ranging from 0 to 30 kA$\cdot$ m^{-1}.

Electron Holographic Tomography (EHT)

The holographic tilt series was recorded at the Institute of Structural Physics, Technische Universitat Dresden (Germany), using the FEI Titan 80–300 Holography Special TEM instrument operated at 300 kV in collaboration with Dr. Daniel Wolf. A two electron bisprism setup is employed for the image acquisition [112] that was adjusted by an upper biprism voltage of 35 V, a lower biprism voltage of 100 V, and an intermediate X-lens (extra lens between the two biprisms) excitation of -0.36 V. For acquisition of electron holograms, a 2 k by 2 k slow scan CCD camera (Gatan Ultrascan 1000 P) was used. The high tilt angles and the manual in-plane rotation of the sample in between the two tilt series (one to reconstruct B$_x$ and one to reconstruct B$_y$) were achieved by means of a dual-axis tomography holder (Model 2040 of E. A. Fischone Instruments, Inc.). The acquisition process is performed semi automatically with an in-house developed software package for an efficient collection of holographic tilt series consisting of object and object-free empty hologram [113]. To reconstruct and process the projection data, treatment was mainly accomplished using in-house developed scripts and software plugins for Gatan Microscopy Suite.

Chapter 3

Comparative magnetic and morphological study of different MTB species

The magnetosome production for biotechnological applications has been considered difficult because of the fastidiousness and complexity of the cultivation medium and growth conditions required for MTB. To produce enough magnetosomes for biotechnological applications, magnetotactic bacteria must be grown under controlled conditions that favor both cell growth and magnetite biomineralization. Various research groups have been trying to push forward the mass cultivation of MTB strains [114–119]. In all the cases, the culture media composition and the incubation conditions have been optimized to increase the growth yield and magnetosome production. In fact, a substantial obstacle for the extensive research on MTB has been the difficulty of growing them in the laboratory. Moreover, the great diversity of MTB implies that different strains will need different types of chemical gradients and nutrients to achieve optimal growth. With all this, the effort to cultivate new species in the laboratory is of great importance, since increasing the number of successfully grown species can help improving and expanding the applicability of both MTB and magnetosomes.

As we shown in Figs. 1.2 and 1.3, the structure of the magnetosome chain and the morphology and size of the magnetosomes are genetically controlled and specific to each species of bacteria. To this respect, when working with magnetosomes their morphology cannot

be easily tuned, since it is directly linked to the particular species of bacteria used. Similar difficulties can be found when trying to modify the structural characteristics of magnetosome chain. In Chapter 2, this specificity and fine control allowed us to employ the magnetosomes to develop theoretical and experimental models capable of being extrapolated to other MNPs systems. However, when it comes to specific applications, this rigorous genetic control can become a limitation, as specific applications may require specific properties. In order to overcome these issues, the group plan to expand the research to two more species of MTB; *Magnetospirillum magneticum* AMB-1 and *Magnetovibrio blakemorei* MV-1 (TEM images of these MTB and their magnetosomes can be found in Fig. 1.4) by cultivating them under different growth conditions. This task was performed by Lucia Gandarias. By characterizing their morphology and studying their magnetic properties, we aim to select the best bacterium for every specific application. Some of the main reported characteristics of both species are:

- *Magnetospirillum magneticum* AMB-1 is a freshwater species with spirillum morphology that synthesizes truncated-octahedral nanoparticles with a slight distortion and a mean size of $\sim$ 40 nm. The main reported difference with *Magnetospirillum gryphiswaldense* MSR-1 is the formation of fragmental chains instead of a long continous chain.

- *Magnetovibrio blakemorei* MV-1 is a marine species with vibrioid to helicoid morphotype, which biosynthesizes elongated magnetite nanoparticles with a crystal morphology that has been described as truncated hexa-octahedra with $35 \times 35 \times 65$ nm dimensions [120].

In order to characterize the magnetic properties of both species, we will also use different cultivation methods. In this regard, we are going to make special emphasis on the importance of controlling the growth medium during the MTB culture, as the magnetic properties of magnetosomes such as coercivity, remanence, and Verwey transition temperature systematically change with it.
The changes in magnetosome chain morphology and magnetic properties throughout the different cells will be carefully studied by a combination of transmission electron microscopy (TEM), magnetometry and synchrotron experiments: X-ray Magnetic Circular Dichroism

(XMCD). Thanks to the experience gathered in the Group of Magnetism and Magnetic materials regarding the magnetic characterization of *M. gryphiswaldense*, throughout the chapter, this specie will be used as a reference to compare with the obtained results. Finally, we will discuss the significance of the changes in the magnetic properties and how this can expand the future applications of the MTB and their magnetosomes.

3.1. *Magnetospirillum magneticum*

Several works have described the use of different favorable culture media for the growth of species of the genus *Magnetospirillum*, such as Magnetic Spirillum Growth Medium (MSGM) [121], Optimized Flask Medium (OFM) [116], or the Flask Standard Medium (FSM) [122]. In the literature, the most extensively reported medium for the growth of *M. magneticum* is the MSGM enriched with a Wolfe's mineral solution (WMS) [123]. But there is a problem that has been ignored until now: this supplement contains low concentrations of transition metal chlorides and sulphates, such as $MnSO_4$, $FeSO_4$, $CoCl_2$, $ZnSO_4$ or $CuSO_4$, and *M. magneticum* strain has demonstrated the ability to incorporate transition metals into the magnetosomes [123, 124]. Therefore, we have focused on the impact of the employed growth medium in the magnetic properties of the *M. magneticum* AMB-1, by culturing them in: a MSGM Medium with a Wolfe's mineral solution (MSGM+W), and a MSGM medium without this solution (MSGM-W). In addition, we have also studied the magnetic properties of *M. magneticum* cultured in FSM medium, the same employed for the *M. gryphiswaldense*.

3.1.1. *M. magneticum* grown in MSGM

M. magneticum AMB-1 was grown in three-fourths 1L-bottles loosely capped at 28°C without shaking in a modified magnetic spirillum growth medium (MSGM) [121] enriched with a Wolfe's mineral solution (MSGM+W) and without it (MSGM-W). A magnetic inoculum with cells at early stationary phase was employed. After 48 h-incubation, when bacteria present well-formed magnetosomes chains, cells were fixed with 2% glutaraldehyde, harvested by centrifugation, washed three times and finally concentrated up to 10^9-10^{11} cell/mL in ultrapure water.

3.1.1.1. Transmission Electron Microscopy (TEM)

Fig 3.1 displays representative TEM images of bacteria grown in MSGM+W and MSGM-W and the corresponding size histograms of the magnetosomes. The particle size distribution was analysed using a standard software for digital electron microscope image processing, ImageJ [110] (See Table 3.1). In all cases, we observed the formation of magnetosomes with a truncated octahedron morphology, as in the case of *M. gryphiswaldense*.

As we can see in Fig. 3.1 and Table 3.1, under the used growth conditions, all the cells formed fragmental chains. The fragmental chain commonly consists of 1-7 short chains separated by large gaps (hereafter referred to as *subchains*). Each subchain contains 2–8 closely aligned magnetosomes. As it was the case with *M. gryphiswaldense* MSR-1 strain, smaller magnetosomes are usually formed at the end of the subchains. The subchains are aligned along the long axis of the cell. No relevant morphological differences are observed between the bacteria grown in MSGM+W and MSGM-W. Regarding the magnetosome size distribution, MSGM-W length distribution is centered at $< L >= 40$ nm with a standard deviation $\sigma = 12$ nm, while MSGM+W distribution has a mean value value of $< L >= 44$ nm with a standard deviation $\sigma = 15$ nm.

Growth Media	*N*	*L(nm)*	*S*	*M/S*
MSGM-W	15±3	40±12	4±1	5 ± 1
MSGM+W	15±3	44±15	5±1	5 ± 1

Table 3.1: *Data of magnetosome and subchain formation of AMB-1 grown in different culture media. N, the averaged number of magnetosomes per cell. L, magnetosome mean size. S, average number of subchains. M/S, average number of magnetosomes per subchain.*

3.1.1.2. X-ray Absorption Spectroscopy (XAS) and X-ray Magnetic Circular Dichroism (XMCD)

M. magneticum strain has demonstrated the ability to incorporate transition metals into the magnetosomes [123, 124]. To study the possible incorporation of the transition metals found in the growth media

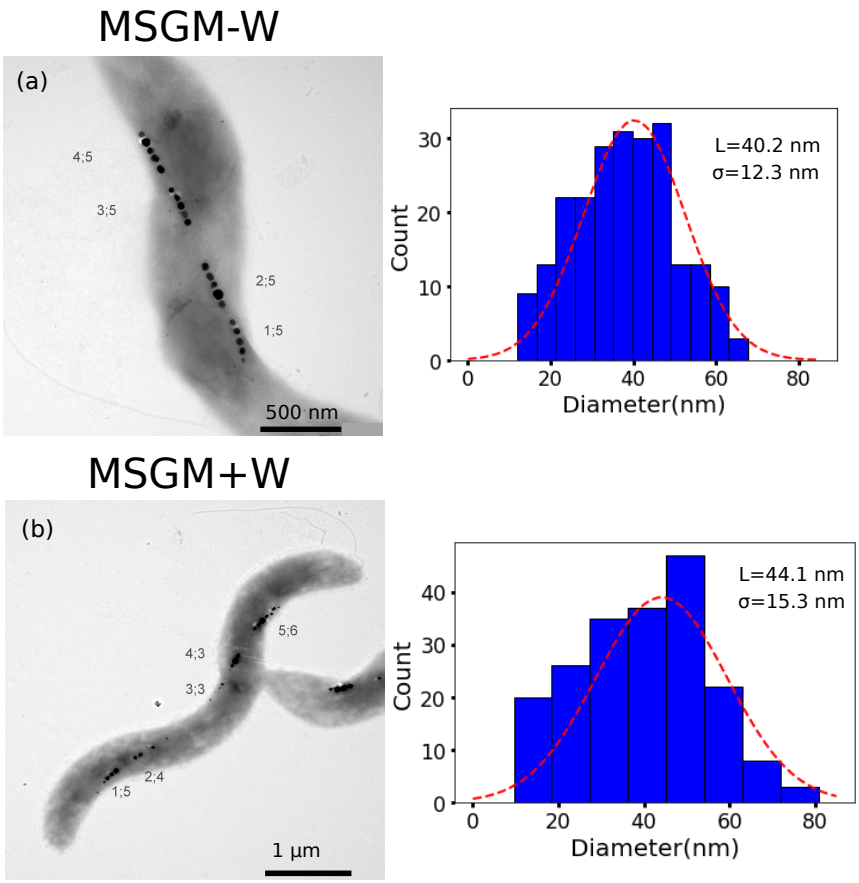

Figure 3.1: *(Left Column) TEM image of M. magneticum grown in MSGM-W (a) and MSGM+W (b). The numbers in the images refer to chain-label and the number of magnetosomes per subchain. (Right column) The corresponding size distribution histograms. L, magnetosome mean size. σ, standard deviation of each histogram.*

(Co, Mn and Cu) within the spinel structure of magnetosomes, both X-ray Absorption Spectroscopy (XAS) and X-ray Magnetic Circular Dichroism (XMCD) at Fe, Co, Mn and Cu $L_{2,3}$ edges were performed on the MSGM+W bacteria. Both are very powerful element-sensitive techniques that can provide accurate information on the oxidation state and site occupancy of the different ions present in the spinel structure of magnetite. The experiments were carried out on whole cells grown in MSGM+W supplemented medium using the ALICE

station [125, 126] at the PM3 beamline of BESSY II in Berlin, Germany (More information about the technique can be found in Materials and Methods section).
Figs. 3.2 a-d show the room temperature normalized absorption spectra at magnetic remanence at the Mn, Fe, Co, and Cu $L_{2,3}$ edges measured in transmission mode at remanence after applying a magnetic field of ± 0.74 T (I+-) along the beam propagation direction. For all the measurements, X-rays circularly polarized with right helicity, impinge at normal incidence with respect to the sample surface. Only in the case of Co, and of course in the case of Fe, clear absorption peaks are detected in these spectra. This already indicates that if Mn and Cu ions are incorporated into the magnetosomes structure, they must be in a very low content, lower than the resolution limit of the technique ($<$ 2000 ppm). The corresponding XMCD spectrum (I^+-I^-) at Fe L_3 is shown on Fig 3.2 e. As depicted, the spectrum consists of three main components related to the three different iron occupations of magnetite. The sign of the magnetic dichroism for each component is defined by the direction of its magnetic moment. Negative intensities correspond to the Fe^{2+} and Fe^{3+} in octahedral places which are aligned ferromagnetically, while the peak for Fe^{3+} placed in tetrahedral sites, coupled antiferromagnetically shows a positive intensity. When comparing with the theoretical spectra of magnetite [127, 128], XMCD measurements reveal a decrease in the Fe^{2+} peak intensity, which suggests the substitution of Fe^{2+} ions by other doping elements, probably Co^{2+}. Unfortunately, the Co signal obtained in the XAS spectra is not large enough to obtain a reliable XMCD spectra for this element. By comparing XMCD data with theoretical spectra for each peak, the site occupancies of the Fe cations can be estimated, being the ratio of Fe^{2+}Oh : Fe^{3+}Th : Fe^{3+}Oh, 0.84(5) : 0.95(5) : 1.00(6). The expected ratio for stoichiometric magnetite is 1 : 1 : 1. For undoped magnetosomes of *M. gryphiswaldense* a ratio of 1.00(4) : 1.02(5) : 0.96(5) has been reported, close to the one of stochiometric magnetite [92]. This reduction of the Fe^{2+}Oh peak intensity indicates the substitution of Fe^{2+} ions with Co^{2+} ions in octahedral positions. Moreover, by scaling the intensity of the XAS spectra at Co $L_{2,3}$ edges with respect to the spectra at Fe $L_{2,3}$ edges, we estimate that cobalt accounts for approximately 4% of the total metal ion content of the MSGM+W magnetosomes.

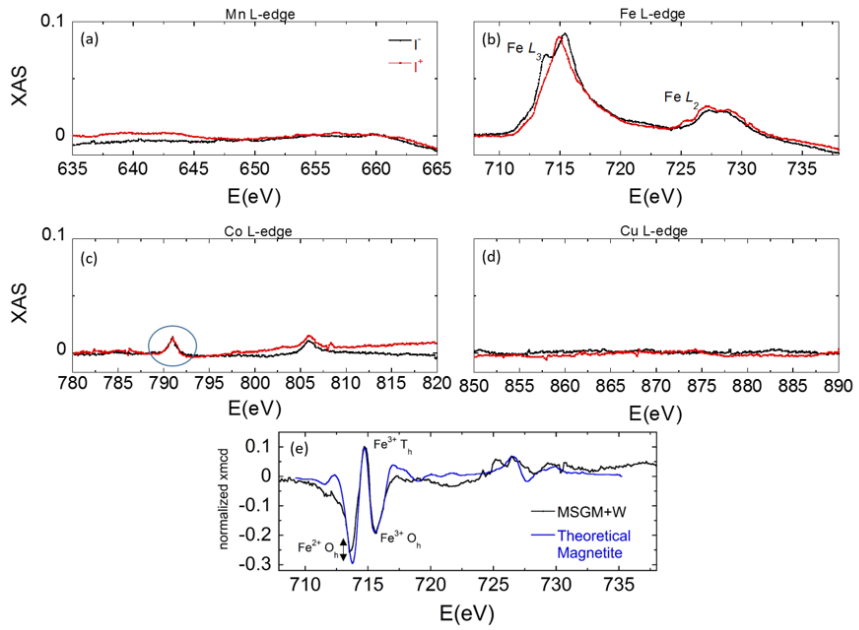

Figure 3.2: *X-ray absorption spectra (XAS) at (a) Mn, (b) Fe, (c) Co and (d) Cu L-edges acquired in transmission mode at 300K and at remanence. (e) XMCD signal at Fe L-edge, I^+-I^-, where the theoretical spectrum of magnetite has been superimposed.*

3.1.1.3. Magnetic Characterization

The presence of metallic ions in the magnetosomes (e.g Co) can modify their magnetic response. This change of the magnetic properties can enhance the applications of MNPs in general and magnetosomes in particular. Previous works have shown that the cobalt integrated within the structure of the magnetosomes significantly increases the magnetocrystalline anisotropy contribution and therefore the coercivity and remanence [92, 123]. Thus, in this section we will carefully proceed to analyze and compare the magnetic response changes appearing for *M. magneticum* grown in MSGM+W and MSGM-W, using different experimental methods.

3.1.1.3.1. Magnetization vs. temperature, M(T)

$M(T)$ measurements were carried out in freeze-dried cells encapsulated in gelatin capsules. Zero-field-cooling/field-cooling (ZFC/FC)

magnetization curves were measured in a superconducting quantum interference device, SQUID, magnetometer (Quantum Design MPMS-3). Samples are cooled in absence of any external field from 300 K down to 5 K. At 5 K a fixed magnetic field of 10 mT is applied and the magnetization is measured upon warming to 300 K (ZFC). With the field still on, the sample is cooled down again to 5 K and the magnetization is measured upon warming to 300 K (FC). Fig. 3.3 shows the ZFC/FC curves of bacteria grown on both media, MSGM+W and MSGM-W. Data are compared with those of *M. gryphiswaldense* for reference.

In the case of cells grown without Wolfe's mineral solution (MSGM-W) both FC and ZFC curves present an irreversibility in the whole studied temperature range and show a clear Verwey transition around 103 K. The fact that the Verwey transition is so abrupt is an indicative of the homogenous stoichiometry of magnetite in magnetosomes and reflects the precise biological control exerted by MTB during the biomineralization process [72]. As depicted, the ZFC/FC curves are very similar to those measured for *M. gryphiswaldense*. However, in the case of cells grown with the Wolfe's mineral solution (MSGM+W) the ZFC/FC curves show again clear irreversibility, but the shape of the curves is different. The Verwey transition is less sharp and only barely discerned at around 100 K. This effect becomes more evident if we compare the derivatives of the ZFC curves for the three samples (see the inset). As it can be seen, the peak of the derivative, which marks the onset of the transition, is broader, less intense, and displaced towards lower temperatures for the MSGM+W. This strongly indicates an overall decrease of magnetite purity and/or increase of crystalline disorder. In fact, this behavior is a well-known characteristic of cobalt doped magnetosomes [92, 123, 129]. This effect further supports the fact that cobalt doping occurs when we grow *M. magneticum* in a MSGM+W medium, changing the magnetosomes magnetic properties.

3.1.1.3.2. Magnetometry on 3D bacterial arrangements

Macroscopic oriented hysteresis loops of *M. magneticum* cells have been measured by VSM magnetometry at room temperature. 3D arrangements of aligned bacteria have been obtained by pouring the cells, under an applied "aligning" uniform magnetic field of 1T, into liquid agar that hardens upon cooling. A schematic representation of

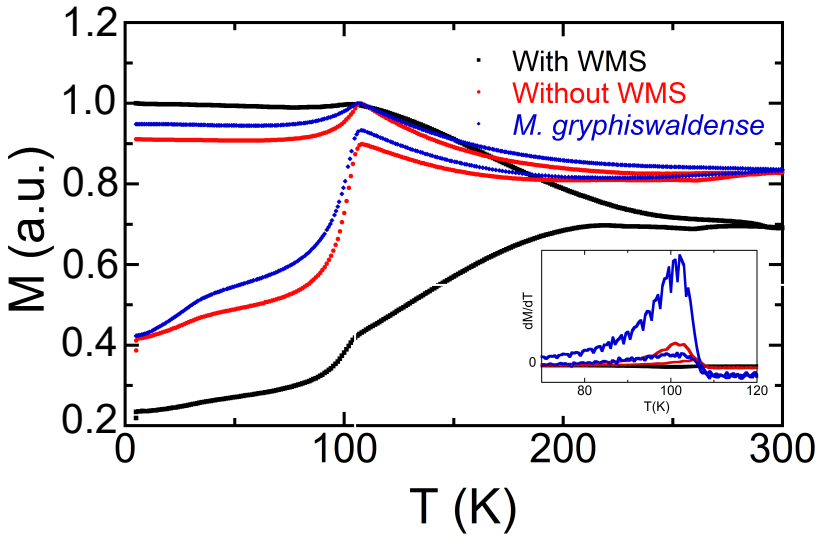

Figure 3.3: *ZFC/FC magnetization curves measured at 10 mT for M. Magneticum grown in MSGM+W and MSGM-W media. The magnetization curve of M. Gryphiswaldense is also included as reference. The inset displays the derivative of ZFC/FC curves for the three samples.*

the method is shown in Fig. 3.4 a. To achieve this, we resuspend 500 μL of a bacterial colloid (10^{11} cell/mL) in 500 μL of an agar solution (2% agar and 98% water) at 80°C to maintain the solution in a liquid state. To align the bacteria, a uniform magnetic field of 1 T was applied. After 3 minutes, the field was turned off, and the sample was cooled using liquid nitrogen until the temperature reached around 0° C. This caused the agar to solidify, trapping the bacteria, and keeping this solidified state at room temperature, as it is shown in Fig. 3.4 a. Further details are found in Materials and Methods section.
As we already know, MTB are highly anisotropic magnetic objects. Therefore, their hysteresis loops measured at different angles depend strongly on the relative direction between the applied field and the alignment direction. The hysteresis loops of oriented bacteria have been measured, at room temperature, at different angles Ω (See Fig. 3.4 b), which is the angle between the applied magnetic field and the

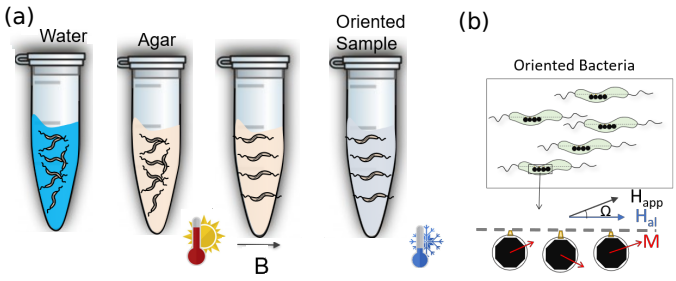

Figure 3.4: *(a) Schematic representation of the oriented MTB sample preparation. (b) Up: Oriented bacteria under an aligning field. Down: Schematic representation of the angle between the aligning and measurement field (Ω) and of the magnetic moment tilting of the chain.*

alignment direction. We have measured these hysteresis loops from 0° to 90° in steps of 10 degrees. Fig. 3.5 a, b shows the hysteresis loops obtained at two different angles, 0 and 90°. At a glance, we see that the hysteresis loops of the 3D bacterial arrangements do not match to the Stoner-Wohlfarth model of a single uniaxial domain, with the easy axis perfectly oriented along the chain axis [130], since the hysteresis loops perpendicular to the chain axis (referred as 90°) are not anhysteretic as expected. This could be attributed to the tilting of the magnetic moments of the magnetosomes out of the chain axis, as represented in Fig. 3.4 b. This was already revealed in Chapter 2 for *M. gryphiswaldense*. In Fig. 3.5 c-f, the experimental normalized remanence and coercivity of bacteria in the 3D arrangements are plotted for the different orientation angles between 0° and 90° in a polar representation. For the MSGM+W bacteria, the coercive field decreases from 28.3 mT at 0° down to 15.8 mT at 90°, while for the MSGM-W range between 25.6 mT at 0° to 9.9 mT at 90°. On the other hand, the M_r/M_s value for the MSGM-W bacteria, evolve from from 0.95 at 0° down to 0.15 at 90°, while for MSGM+W range between 0.83-0.27.

More information on the magnetism of the magnetosome chains and changes between MSGM+W and MSGM-W samples has been gathered from the theoretical modelling of the hysteresis loops as a function of angle Ω. Unlike in Chapter 2, we don't have ECT images of *M. magneticum* AMB-1 chain to determine the XYZ positions

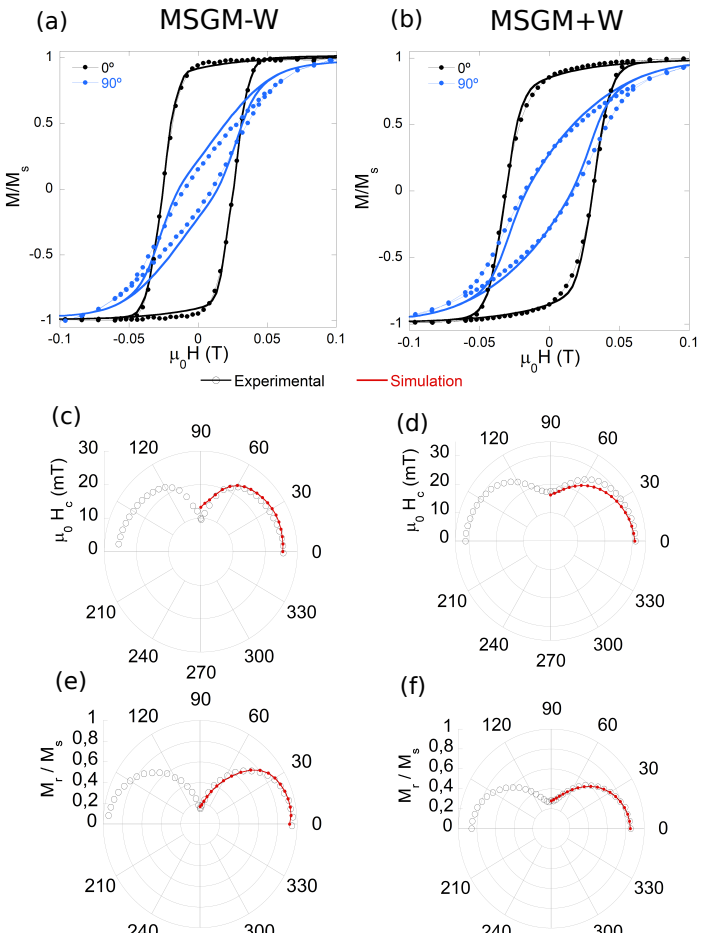

Figure 3.5: *Hysteresis loops of magnetotactic bacteria M. magneticum for MSGM-W (a) and MSGM+W (b) forming 0° and 90° with the aligning field. Polar plots of the coercivity (c, d) and remanent magnetization (e, f) for both cultures. The solid lines correspond to the values obtained from the simulation considering a mean uniaxial anisotropy constant of K_{uni} = 12 kJ/m^3 and K_c = -10 kJ/m^3 for MSGM-W and; K_{uni} = 16 kJ/m^3 and K_c = 3 kJ/m^3 for MSGM+W.*

and relative orientations of each magnetosome inside the whole chain. Therefore, in this case, the inter-particle dipolar interactions cannot be calculated independently, and they are considered as an additional uniaxial anisotropy added to the shape anisotropy, resulting an ef-

fective uniaxial anisotropy. In this regard, the approach followed to simulate the hysteresis loops essentially consists on the resolution of a Stoner-Wohlfarth based model. This method was developed explicitly by Carrey *et al* [131] for the case of uniaxial single domain magnetic particles (See Fig. 3.6 b). However, the approach can be generalized for more complex problems as those involving cubic, mixed or multiaxial anisotropies.

Following the same approach that our group has employed before to carry out hysteresis loops calculations for *M. gryphiswaldense* (see L. Marcano doctoral thesis [72] and Orue *et al.* [71]), the magnetosomes chain have been considered as a collection of independent single domain particles which are large enough to be thermally stable and thereby having the magnetization firmly anchored at the energy minima. The functional form of the energy density for a magnetic single domain depends on the orientation of magnetization given by two variables (polar and azimuthal angles in spherical coordinates). Such energy density landscape $E\ (\theta,\ \phi)$, in the presence of arbitrary external magnetic fields, is determined by the cubic magnetocrystalline anisotropy of magnetite, the effective uniaxial magnetic anisotropy (which includes shape and dipolar interactions effects) plus the Zeeman energy:

$$\begin{aligned} E(\theta,\phi) = E_{anisotropy}(\theta,\phi) + E_{zeeman}(\theta,\phi) = \\ E_{cubic} + K_{uni}[1-(\hat{u}_{uni}\cdot\hat{u}_m)^2] - \mu_0 MH(\hat{u}_H\cdot\hat{u}_m) \end{aligned} \tag{3.1}$$

For a given function $E\ (\theta,\ \phi)$, determination of M_H (magnetization projection over $\vec{H}$) is performed by a simple dynamical approach in which the single domain magnetization can switch between the available energy minima states at a rate determined by a Boltzmann factor v_{ij} [131, 132],

$$v_{ij} = v_0 e^{-\Delta E_{i,j} V/K_B T} \tag{3.2}$$

where v_0 is the natural frequency of jumps attempts of electron spins (10^9 Hz), of the order of the Larmor precession frequency, denoted by $v_0 \sim 10^9$ Hz, and $\Delta E_{i,j}$ V are the energy barriers between such minima ($\Delta E_{i,j}$ is the energy density barrier between minima i and j, and V is the particle volume) and can be calculated from the field dependent energy landscape. Therefore, the magnetization is given by:

$$M_H(\vec{H}) = \sum_i p_i(\vec{H})\hat{u}_i(\vec{H})\cdot\hat{u}_H \tag{3.3}$$

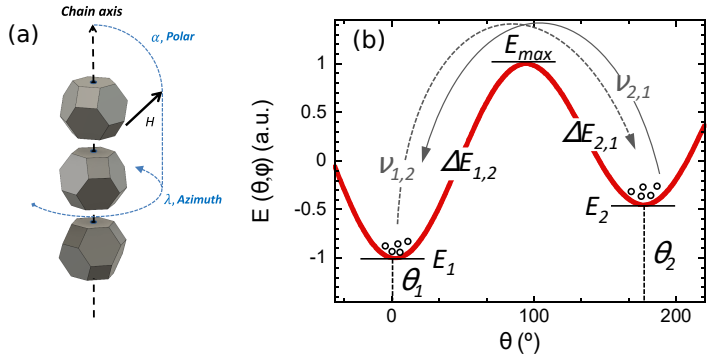

Figure 3.6: *(a) Polar (α) and azimuthal (λ) angles defining the orientation of the external field relative to the chain axis. (b) Illustration of the energy landscape of an uniaxial single domain magnetic particle as function of θ in the presence of an arbitrary fixed external magnetic field obtained from [72].*

where $p_i(\vec{H})$ are the probabilities of finding the magnetization at state i (i = 1, 2,3,4...etc, depending on the number of energy minima), $\hat{u}_i(\vec{H})$ are the director vectors that defines the position of the energy minima, dependent on the external field $\vec{H} = H\hat{u}_H$.
The quasistatic condition for the externally applied magnetic field in DC magnetometry can be reproduced by a slowly varying sinusoidal field ($H(t) = H_0$ sin $(\omega t)\hat{u}_H$), of frequency much smaller ($v \sim 1$ Hz) than the natural frequency of jumps attempts of electron spins $\sim 10^9$ Hz. In this way, probabilities $p_i(\vec{H})$ become time-dependent functions $p_i(t)$ that can be calculated by numerically solving ordinary differential equations:

$$\frac{dp_i}{dt} = \sum_{j \neq i} w_{ji} p_j - (\sum_{j \neq i} w_{ij}) p_i \tag{3.4}$$

This continuity equation reflects the simple fact that the increment of population i results from the balance between incoming jumps (first term) and outcoming jumps (second term) to or from the rest of the minimum states, with the conservation of magnetization condition given by $\sum p_i = 1$. This is represented schematically for an uniaxial single domain magnetic particle in Fig. 3.6 b.
Either because the whole chain is free to rotate around itself or because magnetosomes can be rotated relative to each other, simulations

for the whole chain for a given orientation between the external field H and the chain axis (angle α, in the scheme of Fig. 3.6 a) must be averaged for the equally probable azimuthal orientations, between 0° and 360°, relative to the polar axis defined by the chain (angle λ, in the scheme of Fig. 3.6 a). Possible misalignments of the chains with respect to the aligning field, angle α, occurring during sample preparation have been considered by including a Gaussian angular distribution of the chain axes, P(α). We tested distributions of different widths, being finally the corresponding one to a standard deviation of 10° the one that best fits to the experimental data, in agreement with misalignment values reported previously [97]. Moreover, to take into account the size dispersion existing in the NPs, shown in Fig. 3.1, a gaussian distribution for the uniaxial anisotropy constant is also included, P(K). As we explained earlier, smaller magnetosomes are formed at the end of the subchains and, in general, morphological differences lead to a change in the energy density landscape E (θ, ϕ). We have thus used a gaussian anisotropy distribution considering different values of $K_{uni} \in$ [6 kJ/m^3, 24 kJ/m^3]. These differences in K_{uni} observed among the magnetosomes can thus be ascribed to either changes in the elongation ratio and/or the dipolar interactions between magnetosomes. Therefore, the final expression for the calculation of the hysteresis loop, obtained for a certain angle Ω is:

$$M(H) = \int_0^{90} P(\alpha)d\alpha \int P(K)dK \int_0^{\pi} M_H(H, K, \alpha, \lambda)d\lambda \qquad (3.5)$$

where $M_H(H, K, \lambda, \alpha)$ is the magnetization projection along the applied magnetic field corresponding to a single value of the effective anisotropy constant K and a single orientation of the easy axis, relative to the applied magnetic field. Except for the case of external field applied parallel to the chain ($\alpha = 0$), where all particles are equivalent by symmetry, the resultant hysteresis loop is calculated by averaging 18 single loops from $\lambda = 0°$ to λ= 180° in steps of 10°.
Employing this model, our group [72] managed to fit *M. gryphiswaldense* hysteresis loops, using the magnetocrystalline anisotropy constant, K_c = -11 kJ/m^3, and magnetization, $M_s = 48 \times 10^4$ A $\cdot$ m^{-1}, values of magnetite; and considering for each magnetosome an effective easy axis deviated 20° from the chain axis, with a value of K_{uni} = 12 kJ/m^3 to account for both shape anisotropy and magnetic interactions. As it was shown in Chapter 2 for *M. gryphiswaldense*, this tilting of the magnetization with respect to the chain axis is inherent

to the truncated octahedron magnetosome morphology. In the case of *M. magneticum*, we have been able to simulate quite accurately the hysteresis loops of MSGM+W and MSGM-W bacteria by setting the uniaxial axis, $\hat{u}_{uni}$ at 20° with respect to the chain axis. By setting this angle, the effective easy axis is found to lie at 15° out of the chain axis. Following what we learned in the previous chapter, this could be indicating a different elongation degree in the case of the truncated octahedron of this species. From the simulations, shown in Fig. 3.5 a-b, we obtain the following values for the magnetocrystalline (K_c) and uniaxial (K_{uni}) anisotropies: K_c = -10 kJ/m^3 and K_{uni}= 12 kJ/m^3 with $\sigma = 4$ kJ/m^3 for MSGM-W, while $K_c = 3$ kJ/m^3 and $K_{uni} = 16$ kJ/m^3 with $\sigma = 4$ kJ/m^3 for MSGM+W. The accuracy of the fittings is more evident in the polar plots of the reduced remanent magnetization and coercivity, shown in Fig. 3.5 c-f. The increase of K_{uni} for the magnetosomes grown in MSGM+W in comparison to those in MSGM-W could be related to the small changes in the subchains that we reported in the TEM analysis (Table 3.1), and/or to a slightly higher deformation of the magnetosomes in the MGSM+W sample. In addition, for the specie *M. gryphiswaldense*, using the same Stoner-Wohlfarth approach, the value for K_{uni} was 12 kJ/m^3. These results would suggest that MSGM+W magnetosomes tend to exhibit a greater elongation rate than those from *M. gryphiswaldense*, something that has been proposed before [133]. However, from TEM images, it is very difficult to observe any differences, and for a proper study, an ECT analysis or similar, as the one carried out in Chapter 2, would be necessary. Moreover, in this case we had to consider a gaussian distribution to account for size dispersion, something that was not necessary in our previous simulations of *M. gryphiswaldense*. With respect to the magnetocrystalline contribution, in the case of the MSGM-W sample, which does not have cobalt, we use K_c = -10 kJ/m^3, which is the typical value for bulk magnetite crystal (K_{crys}= -10/-11 kJ/m^3). In this case, however, we have not considered the presence of an additional positive cubic anisotropy contribution related to the truncated octahedral morphology of magnetosomes, as was explained in Chapter 2 ($K_{sh-c} \sim 1.5$ kJ/m^3). To test the impact of this extra contribution in our results, we carried out several simulations changing the cubic constant between -7 kJ/m^3 and -11 kJ/m^3, and within these values no major differences were observed in the hysteresis loops. On the other hand, in the case of MSGM+W,

we found a huge change in K_c compared to MSGM-W, revealing a positive value of 3 kJ/m^3. This great increase of cubic magnetocrystalline contribution is a very strong confirmation of the incorporation of cobalt ions to the spinel structure of magnetite [92].

3.1.1.3.3. Magnetization vs. magnetic field, M(H)

$M(H)$ measurements were also performed on freeze-dried encapsulated cells for both batches at different temperatures. In this case, MTB are randomly arranged. Magnetization loops were measured between 1 and -1T at different temperatures between 300 and 5 K. In Fig. 3.7 a we see how at 300 K the M(H) loops of MSGM+W and MSGM-W magnetosome chains overlap, being the M_r/M_s values, shown in Fig. 3.7 e, of both samples close to 0.45. However, as the temperature decreases clear differences in the shape of the loops of these 2 samples arise. We can better track these differences by plotting the coercive field ($\mu_0 H_c$) and reduced remanence (M_r/M_s) versus temperature, as shown in Fig. 3.7 d, e. Again, we add the corresponding curves for *M. gryphiswaldense* as reference. For the MSGM-W bacteria, the coercive field is constant from 300 K down to T_V with $\mu_0 H_c \sim 20$ mT. Then, below T_V, the coercivity raises up to 57 mT at 5 K. On the contrary, the M_r/M_s value is nearly constant, around 0.44-0.49, throughout the whole temperature range. This behaviour is very simillar to the one obtained for *M. gryphiswaldense*. However, in the case of MSGM+W bacteria several changes take place. The values of the coercive field at room temperature are similar, but then, as we decrease the temperature, the coercive field reaches higher values, up to 108 mT at 5K. The value of the remanence for MSGM+W is also nearly constant from 300 K down to 230 K at 0.45, similar to the control magnetosomes, but below that temperature greatly increases up to a value of $M_r/M_s = 0.6$ at 30 K and drops steeply afterward, down to 0.53 at 5 K.

These results clearly reveal that *M. Magneticum* AMB-1 bacteria grown in MSGM-W present similar magnetic reponse to that obtained for *M. Gryphiswaldense*. However, by changing the medium, and incorporating Wolfe solution, that magnetic response of *M. Magneticum* AMB-1 greatly varies. This has been related to the incorporation of Co ions present in Wolfe medium into the magnetosome structure.

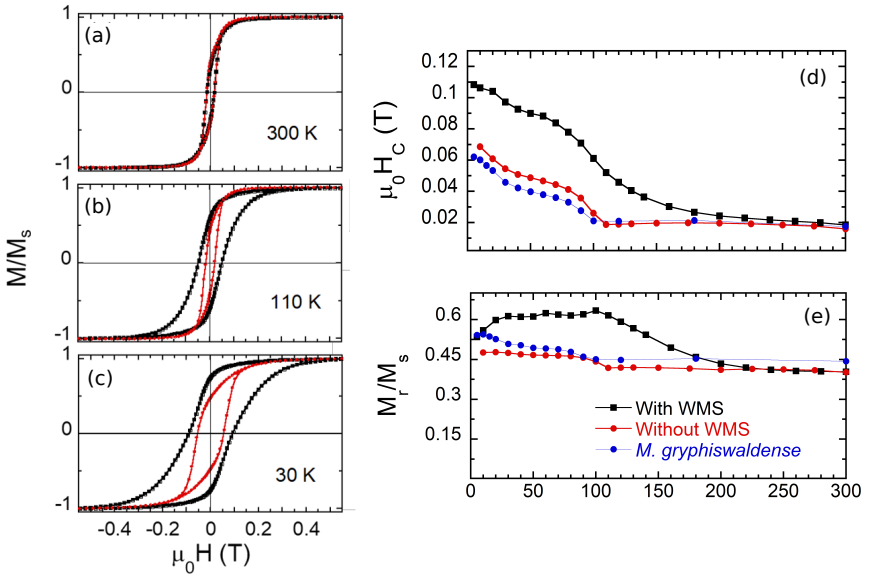

Figure 3.7: *Hysteresis loops of M. magneticum grown in MSGM-W and MSGM+W media at random measured at (a) 300 K, (b) 110 K and (c) 30 K. d) Coercive field ($\mu_0 H_c$) and e) reduced remanence magnetization (M_r/M_s) comparison as a function of temperature with M. gryphiswaldense included*

In conclusion, we have carried out a systematic study on the magnetosome formation within *M.magneticum* AMB-1 grown in MSGM by the combination of TEM, bulk magnetic measurements, element- and site-specific XMCD analyses and magnetic modelling. The study has revealed that:

- Both culture media (MSGM+W and MSGM-W) can be employed to grow *M. magneticum* with different magnetic response. Depending on the target application, the most appropriate medium can be selected.

- The amount of cobalt within the initial growth medium enriched with a Wolfe's mineral solution does not significantly change the cell growth and/or the magnetosome formation.

- Co^{2+} ions are incorporated into Oh sites of magnetosome magnetite through the replacement of Fe^{2+} ions.

- The incorporation of Co^{2+} results in a pronounced increase in magnetocrystalline anisotropy and magnetic coercivity. This modification of magnetosome magnetic properties opens the door to extend their applicability.

3.1.2. *M. magneticum* grown in FSM

So far we have worked with the standard MSGM culture medium usually employed to grow *M. magneticum* AMB-1. However, since 2011 the group mantains a regular culture of *M. gryphiswaldense* grown using a Flask Standard Medium (FSM). This growth medium is simpler than MSGM in its elaboration. For this reason,we tried to culture *M. magneticum* AMB-1 using FSM medium instead of MSGM. After succeeding in growing this species in FSM, we tried to evaluate if the new medium was affecting the structural and/or magnetic properties of *M. magneticum* AMB-1. For this, we analyzed TEM imaged of the bacteria at different harvest times (48, 72, and 96 h) and studied their magnetic response.

3.1.2.1. Transmission Electron Microscopy (TEM)

We have employed TEM to analyze the magnetosome biomineralization process within *M. magneticum* grown in FSM. Fig. 3.8 displays a series of TEM images with the corresponding size histograms at specific times after culture incubation. As shown in the histograms, the number and size of magnetosomes increase with increasing biomineralization time. These histograms present 2 size distributions, as has also been typically reported for magnetosomes measured inside *M. gryphiswaldense* bacteria. This reflects that magnetosome nucleation and growth takes place simultaneously in different regions of the cell, in such a way that we can roughly divide the magnetosomes in 2 groups: small magnetosomes, with size < 25 nm, and large magnetosomes, with size > 25 nm. At 48 hours, we can fit these histograms to a double Gaussian curve centered at 17 ± 4 nm and 38 ± 8 nm, corresponding to the size distribution of the small and large magnetosomes, respectively. If we compare the area of both curves, 22 % of magnetosomes are small magnetosomes. After 72 hours, we observed a growth in the amplitude of the Gaussian curve of smaller size, indicating a slight increase in the relative population of small magnetosomes, up to 26%. After 96 h, however, the number of small magnetosomes is very low, 3%, most of the magnetosomes are large, and the average size displaces towards 46 nm. At this time, the size distribution re-

sembles those previously reported in the literature for *M. magneticum* grown in MSGM media [123] and also the one we found in the previous section. Therefore, we can consider that at 96 h the formation and growth of *M. magneticum* magnetosomes in FSM is completed. To this respect, it is worth highlighting the discrepancies observed in

Time	L_1 *(nm)*	L_2 *(nm)*	*S*	*M/S*
48h	17±4	38±8	3±1	6 ± 2
72h	17±4	39±9	3±2	6 ± 2
96h	19±4	46±11	4±1	8 ± 4

Table 3.2: *Data of magnetosome and subchain formation of AMB-1 grown in FSM at different times.* L_1 *and* L_2 *indicates the center of the small magnetosome region and large magnetosomes region respectively, according to the gaussian fit. S, number of subchains. M/S, average number of magnetosomes per subchain.*

the literature for the rates of magnetosome formation. Even for the same bacteria strain, biomineralization times can vary widely from one laboratory to another. In our case, while with MSGM well-formed magnetosomes were evidenced after 48 h, with FSM we needed 96 h to see fully formed magnetosome chains. However, we cannot attribute these differences only to the medium employed, since several works with the same MTB species cultured in the same medium also report different number of hours needed to obtain fully grown magnetosomes. For example, Staniland *et al.* [124] reported the presence of full-sized magnetosomes and well-formed chains 15 min after the iron addition in *M. gryphiswaldense*, while our previous work evidenced long chains only after 240 min [32]. Therefore, additional factors such as environmental conditions, flask volume, etc could also be playing a role.

3.1.2.2. Magnetic Characterization

Our previous results indicate that we are capable of growing *M. Magneticum* AMB-1 bacteria in FSM medium, even if the time required to obtain fully grown magnetosomes is larger than with MSGM medium. In order to ascertain if the magnetic properties of the *M. Magneticum* grown are altered by the new medium; $M(T)$, $M(H)$ and $M(H)$ in 3D bacterial arrengements were performed, using same procedures as in the case of *M. magneticum* grown in MSGM. First, in Fig 3.9, we present the ZFC-FC and the evolution of remanence and coercivity as

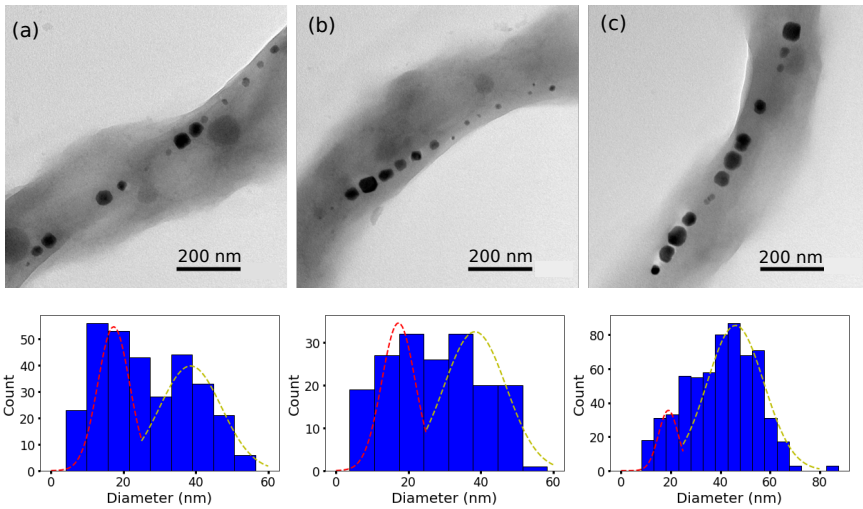

Figure 3.8: *TEM images together with their corresponding size histograms for M. Magneticum grown in FSM medium after (a) 48h, (b) 72h and (c) 96h.*

a function of the temperature for the bacteria randomly arranged and harvested at 48, 72 and 96 h. From the ZFC/FC curves, we can see that the Verwey transition is observed for the three times analyzed, although at longer times it becomes better defined. Regarding the thermal evolution of coercive field ($\mu_0 H_c$) and remanence magnetization (M_r/M_s), we can observe some differences between the three samples (48, 72, and 96 h). The coercive field for the 48 h and 72 h bacteria overlap, being constant from 300 K down to T_V with $\mu_0 H_c \sim$ 13 mT. Then below T_V coercivity raises up to 55 mT at 5 K. Same behaviour is found for 96 h bacteria but changing from 30 mT above T_V to 70 mT below T_V. On the contrary the M_r/M_s values are very simillar and constant, around 0.41-0.49. The most notable difference is the greater coercivity found in the sample harvested at 96h, which can be associated to two things: on the one hand, a larger particle size and on the other hand a greater maturation in the morphology, which basically means the anisotropy of the magnetosome is better defined.

On the other hand, isothermal magnetization curves were measured at magnetic field between -1 and 1 T for bacteria harvested at 96 h and previously oriented in a magnetic field as described in section

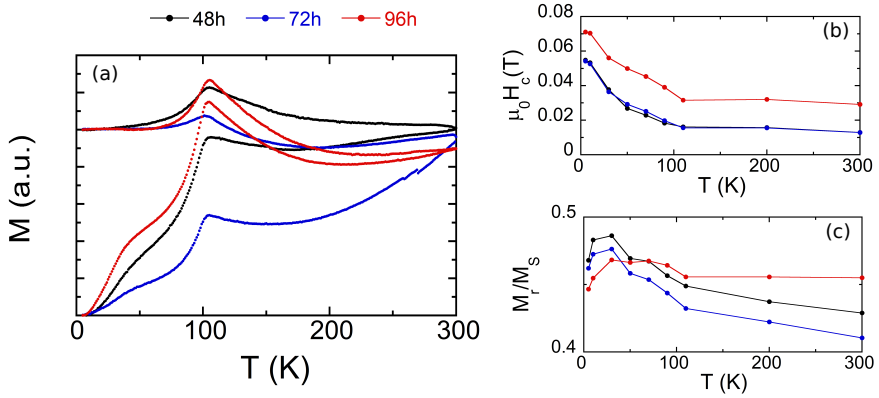

Figure 3.9: *(a) ZFC/FC Magnetization curves measured at 100 mT for the FSM magnetosome chains at different biomineralization times. (b) Coercive field (μ_0 H_c) and (c) reduced remanence magnetization (M_r/M_s) comparison as a function of temperature.*

3.1.1.3.2. In Fig. 3.10 a-b, we present the hysteresis loops of the oriented bacteria at $\Omega = 0$ and and $\Omega = 90$, while in Fig. 3.10 c,d we show the remanence and coervity with respect to the orientation angle of these 3D arrangements.

The simulations carried out, using the same model as in the case of the *M. magneticum* bacteria grown in MSGM, indicate that the best match between simulation and experimental data for FSM hysteresis loops corresponds to a effective easy axis at 15°, a value of K_{uni}=16 kJ/m^3, with a standard deviation of 4 kJ/m^3 and K_c = -10 kJ/m^3. Again the obtained values for the easy axis direction (15°) and the anisotropy constants are close to those calculated for the MSGM-W samples: K_c = -10 kJ/m^3 and K_{uni} = 12(4) kJ/m^3, although the uniaxial anisotropy is greater in the case of FSM medium. This points out differences in the magnetosome morphology depending on the used growth media.

Therefore, the study reveals:

- The overall magnetic properties of the *M. Magneticum* grown in FSM medium are similar to those obtained for the MTB grown in standard MSGM-W medium.

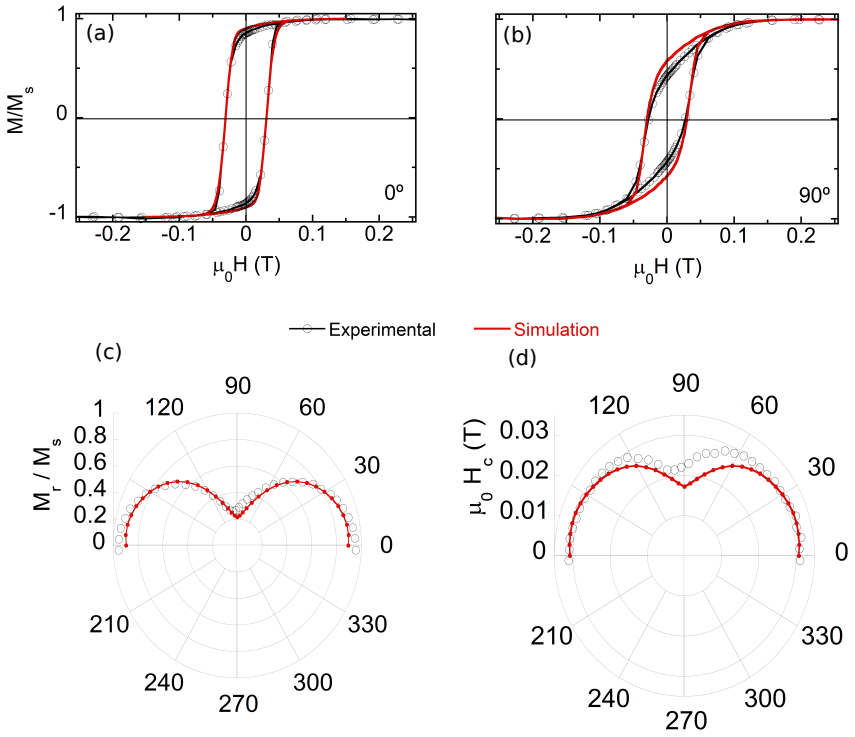

Figure 3.10: *(a) Hysteresis loops of magnetotactic bacteria M. magneticum grown in FSM and harvested at 96h forming Ω=0°(a) and Ω=90°(b) with the aligning field. Polar plots of the (c) remanent magnetization and (d) coercivity for 96 h culture. The red solid lines correspond to K_{uni}=16 kJ/m^3 and K_c = -10 kJ/m^3.*

- The slight differences observed (e.g. K_{uni}) could be related to a higher elongation in the case of *M. magneticum* grown in FSM medium, and put the emphasis again on the importance of the medium to control and tune the magnetic response of the MTB.

3.2. *Magnetovibrio blakemorei*

MTB studies have been mainly focused on a very limited number of strains of the genus *Magnetospirillum*, mostly *Magnetospirillum gryphiswaldense* strain MSR-1 and *Magnetospirillum magneticum* strain AMB-1, due to their relatively facile culture in the laboratory in comparison to other strains of MTB. As we have shown, both species synthesize truncated octahedral crystals of magnetite. Little informa-

tion exists on other cultivated magnetotactic strains which synthesize magnetosomes with different shapes and sizes. As we have been explaining, size and shape are important parameters when designing nanoparticles for numerous biomedical applications. These morphological properties of magnetosomes affect the hysteresis loop shape, changing, for example, their heating efficiency and also their response to guiding magnetic fields, very important points for the targeted drug delivery approximation. Nevertheless, as we have been commenting, magnetosome morphology cannot be easily tuned as it is genetically controlled and linked to the particular bacterial specie used. Therefore, in order to obtain magnetosomes with a different morphology than the truncated cube-octahedron, we have cultured a new species, *magnetovibrio blakemorei* strain MV-1, which produces chains of elongated prismatic hexaoctahedral magnetosomes, as shown in Fig 1.4 c. In addition, we have tried to analyze the differences in their magnetic response compared to *M. gryphiswaldense* and *M. magneticum*. Moreover, by employing the figures and references available in the literature [117, 134–136], we will try to obtain the shape anisotropy of this particles, as we have done with truncated octahedral magnetosomes in Chapter 2.
Unfortunately, the precise culture conditions for *M. blakemorei* are tricky, since the number of variables that influence magnetosome synthesis and microbial growth is large, making it very difficult to establish an optimum culture protocol. At the moment of writing the thesis, an appreciable number of the *M. blakemorei* bacterium in our culture medium do not synthesize magnetosomes. This means that, at the end of the different culture process trials, we do not have enough magnetic mass to carry out a complete magnetic study like we did for *M. gryphiswaldense* and *M. magneticum*. Nevertheless, under the latest growing conditions, we have been able to obtain some initial results on their magnetic response. Therefore, below we will present these magnetic results that, even if preliminary, have allowed us to discern some important magnetic characteristics of this species and can be of interest for future research.

3.2.1. Growth conditions

M. blakemorei strain MV-1 was grown anaerobically at 30°C in a modified Magnetic Spirillum Growth Medium (MSGM) [121] enriched with a Wolfe's mineral solution (MSGM+W). The medium was distributed into Hungate tubes and fluxed with nitrous oxide (N_2O) for

20 minutes prior to autoclaving (15 minutes, 121°C). Finally, after the medium was cooled down to room temperature, 0.58 mM of cysteine was added [117]. After 144 h of incubation, when formed magnetosome chains were observed, the cells were harvested by centrifugation, washed three times in mQ water and fixed in 2% glutaraldehyde.

3.2.2. Transmission Electron Microscopy (TEM)

Fig. 3.11 a shows a TEM image of a number of cells of *Magnetovibrio blakemorei* MV-1. Most of the cells in this TEM image exhibit clearly visible chains of magnetosomes, but we have also observed a significant number of them that do not synthesize magnetosomes or have poorly formed chains. The number of cells without magnetosomes is high compared to the other cultures of MTB, *M. gryphiswaldense* and *M. magneticum*, something that had already been previously reported for *M. blakemorei* [136]. The low number of magnetosomes observed in the TEM images has prevented us from obtaining a reliable size distribution in order to compare it with the one obtained for the other 2 species. In addition, in Fig. 3.11 a, we can also observe the presence of some residues (likely extracellular material and/or rests from the culture medium) in the vicinity of the MTB.
Fig. 3.11 b shows a TEM image of *M. blakemorei* with a fully formed magnetosome chain. *M. blakemorei* strain MV-1 cells present vibroid to helicoid morphology and are motile with a single polar flagellum [137]. In agreement with what has been reported in the literature, the cells possess a single chain containing a variable number of truncated hexa-octahedral magnetite magnetosomes with approximate dimensions of 35×35×65 nm, see Fig. 3.11 c, d [5, 120]. Magnetosomes in the chain are aligned closely parallel to their axis of elongation, the <111> crystallographic direction of magnetite, along the motility axis of the cell [120, 137–139]. Considering that there is an appreciable number of cells that do not present magnetosomes, we can wonder if the magnetosomes we observe in the TEM images have reach the end of the biomineralization process. We will try to answer this question with the magnetic characterization of the specie.

3.2.3. Magnetic Characterization

Due to the small number of cells with a well-formed magnetosome chain, the only way to characterize *M. blakemorei* strain magnetic properties in the laboratory was to prepare 2D samples with the bac-

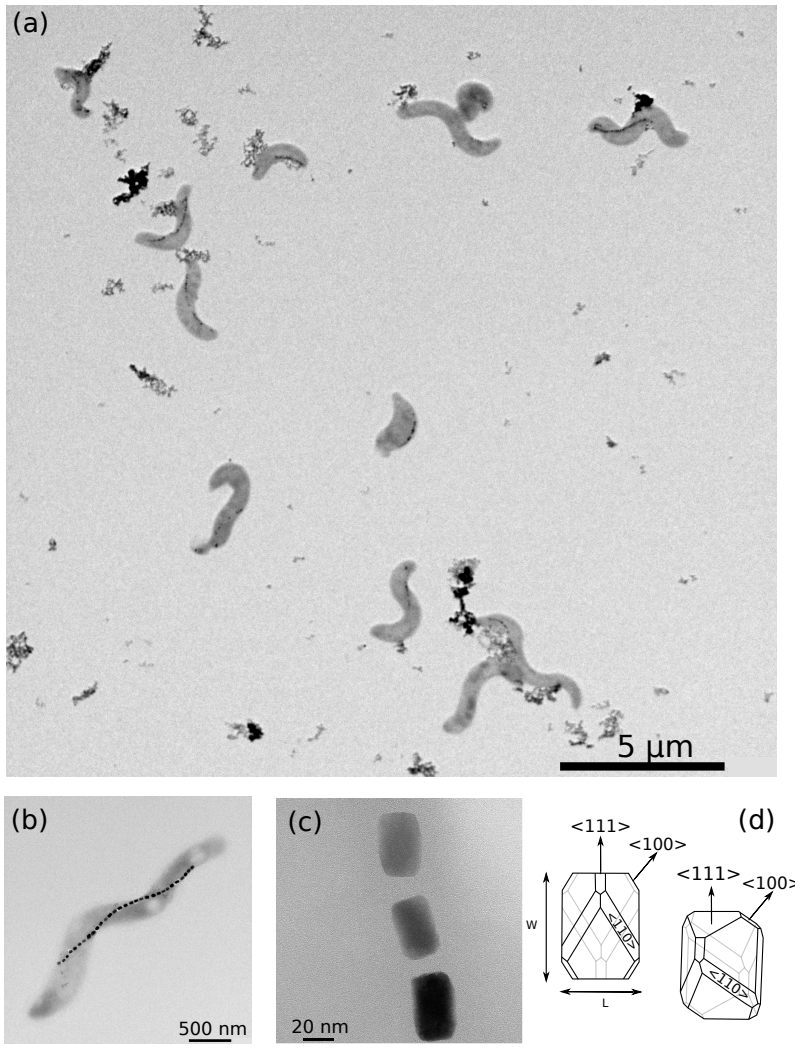

Figure 3.11: *TEM images of M. blakemorei at diferent magnifications (a), (b) and (c) a zoom of the magnetosomes (d) Schematic representations of a truncated hexa-octahedron, crystal habit of M. blakemorei magnetosomes from the strain MV-1, showing the different facets.*

teria randomly arranged. In this case, we pour 10 μl drops of washed cells on a glass rod which is directly inserted in the SQUID magnetometer.This method has allowed us to measure the $M(T)$ and $M(H)$ curves, as before. The protocols we follow to perform magnetic mea-

surements are identical to the ones explained in above sections for *M. magneticum*.

3.2.3.1. Magnetization vs. temperature M(T)

Fig. 3.12 shows the ZFC-FC curves of *M. blakemorei* sample. We must remind here that the samples were grown in MSGM+W medium. As depicted, a high temperature irreversibility is obtained, with the ZFC and FC curves well separated. However, this time, no evidence of the Verwey transition is observed. While in the case of MSGM+W *M. magneticum* cells the Verwey transition could be barely discerned, for *M. blakemorei* the transition has completely dissapeared. This would suggest again that Co ions, coming from transition metal sulphate $CoCl_2$ of Wolfe's mineral solution, are being incorporated to the magnetosomes of *M. blakemorei*, but this time, the incorporation seems to be higher than in the case of *M. Magneticum* (MSGM+W). In addition, at very low T (< 20 K), there is an upturn of the magnetization in both curves. Regarding this paramagnetic like behaviour (highlighted in blue in Fig. 3.12), it can be associated to the bacterioferritin present in the sample [32]. This is a clear indication that the biomineralization of the magnetosomes has not finished in the most of the bacteria, as has been observed at TEM.

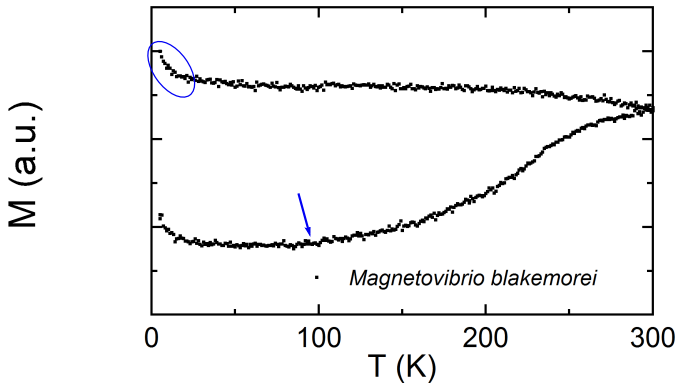

Figure 3.12: *Magnetization curves measured at 100 mT for magnetovibrio blakemorei magnetosome chains.*

3.2.3.2. Magnetization vs. magnetic field, M(H)

Isothermal magnetization loops were also measured at magnetic fields between 6 and -6 T at different temperatures, from 5 to 300 K.
The M(H) loops of *M. blakemorei* magnetosome chains performed at 300, 30, and 10 K are shown in Fig. 3.13 a-c. As can be observed, there are some clear differences between these loops and those measured for the *M. Magneticum* grown in MSGM+W media (also shown in Fig. 3.13). This can be clearly seen if we compare the thermal evolution of both the coercive field and remanence. We can better track significant differences in the plots of the coercive field ($\mu_0 H_c$) and reduced remanence (M_r/M_s) versus temperature shown in Fig. 3.13 d,e. We compare them with *M. gryphiswaldense* grown in FSM (control culture) and *M.magneticum* grown in MSGM+W (the other doped culture). For the *M. blakemorei* bacteria, the coercive field greatly differs from the other two species. It raises up from 23 mT at 300 K to 300 mT at 40K. Then, below 40 K, the coercivity decreases from 300 mT to 220 mT at 5 K. The M_r/M_s value goes from 0.5 at room temperature to 0.8 at 40 K and then decreases to 0.35 at 5 K. These data would suggest that *M. blakemorei* takes notably more Co than the other two. This makes this species of MTB the best candidate for been detoxifying agents scavenging metal ions, another possible role suggested for MTB [19, 20]. At the same time, as we have already commented several times, an increase in coercivity and remanence at room temperature is a way to increase the hyperthermic efficiency of MNPs.
Finally, in order to obtain more information about the anisotropy contribution in these magnetosomes, we have simulated the $M(H)$ loop at 300 K, using the Stoner-Wohlfarth approach. As we have already explained, we cannot perform magnetometry on 3D aligned cells with the MV-1, due to the lack of magnetic material. However, we can adapt the eqn. 3.5 for the random case (un-oriented bacteria) by setting P(α)=1, that is considering all orientations equally probable.
Moreover, to expand the knowledge about the truncated hexaoctahedral magnetosomes synthesized by this species, we have calculated the shape anisotropy density energy corresponding to this morphology, shown in Fig 3.11 d. For this, we have used the FEM calculations described in Chapter 2 and followed the same procedure. In this case, since we don't have ECT images we have based our calculations on the morphology described in the literature for this kind of magneto-

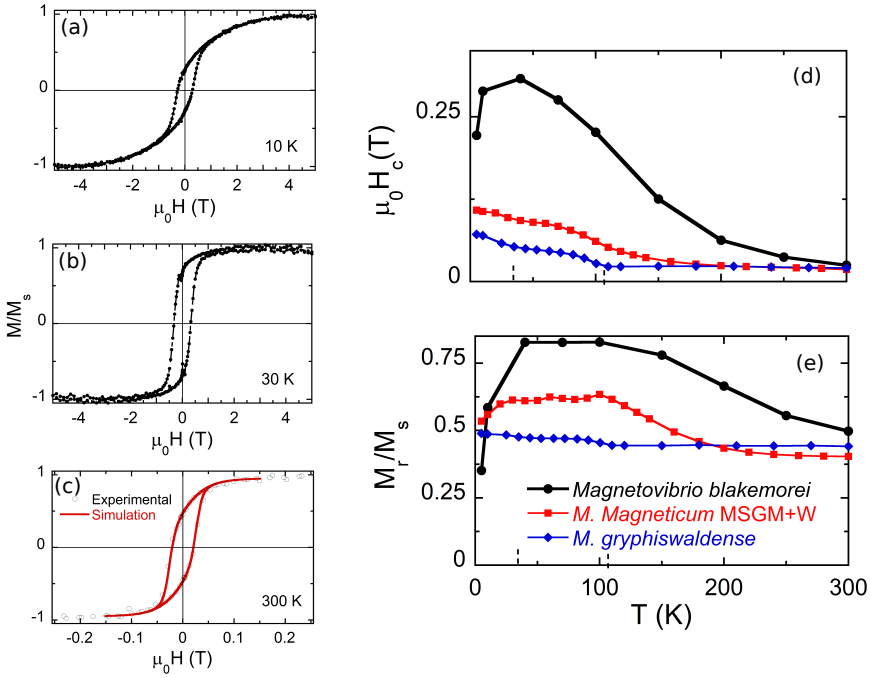

Figure 3.13: *Hysteresis loops of the magnetovibrio blakemorei magnetosome chains measured at (a) 10 K, (b) 30 K and (c) 300 K. In the case of the 300 K hysteresis loops, we also include the simulation corresponding to K_{uni}=14 kJ/m^3 and K_c = 3 kJ/m^3. d) Coercive field ($\mu_0 H_c$) and e) reduced remanence magnetization (M_r/M_s) comparison as a function of temperature.*

somes [120, 138, 139]. From our model, we obtain the energy density landscape presented in Figure 3.14 a. From the analysis of this energy landscape, we can determine the easy axes, and the value of the anisotropy constants. Our inquiries suggest that in the case of the truncated hexa-octahedron morphology, there is only an absolute energy minima located at the <111> direction, which is the elongated axis, as we can see in Fig. 3.14 a. As it happened with the deformed truncated octahedron morphology, the energy barrier between the minima and maxima, and hence, the shape anisotropy of the truncated hexaoctahedral magnetosomes, shown in Fig. 3.11 d, depends on its elongation degree, Width/Length (W/L). As it is shown in Fig.3.14 b, we found that the shape anisotropy constant scales lin-

early with the degree of elongation of the truncated hexa-octahedron morphology and varies between $K_{shape} \sim 30$ kJ/m^3 (W/L=0.6) and $K_{shape} \sim 11$ kJ/m^3(W/L=0.9).

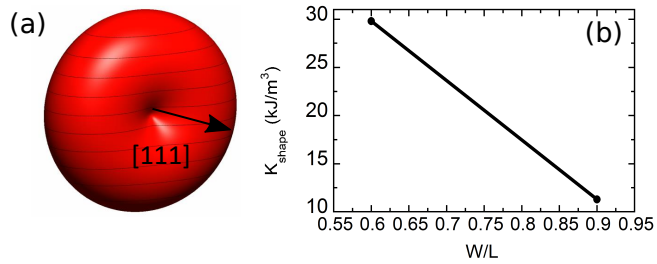

Figure 3.14: *(a) Shape anisotropy energy landscape of the truncated hexa-octahedral magnetosome calculated by FEM method appeared in Chapter 2. Linear dependence on the shape anisotropy constant with the W/L ratio of the truncated morphology.*

Going back to the Stoner-Wohlfarth model, for the case of *M. blakemorei* magnetosomes, we set the uniaxial axis $\hat{u}_{uni}$ at 0° with respect to the [111] crystallographic direction, and we found that the best possible fit for *M. blakemorei* 300 K hysteresis loops corresponds to a value of K_{uni}=14 kJ/m^3, with a standard deviation of 4 kJ/m^3. The quality of the fit can be seen in Fig. 3.13 c. According to Fig. 3.14 b, this would correspond to a W/L ratio around 0.85. The value of $K_c = 3$ kJ/m^3 is the same found for MSGM+W *M. Magneticum* magnetosomes at room temperature.
In conclusion:

- The shape anisotropy of truncated hexaoctahedral morphology has been examined using FEM calculation, showing the linear dependence with the W/L ratio and the significant differences with respect to the truncated octahedron morphology.
- The addition of Wolfe supplement again provokes the controlled doping of magnetosome magnetite resulting in an increase in magnetic coercivity. This increase is notably more pronounced than the one found for *M. magneticum* grown in MSGM+W. In a first approximation, the increase in coercivity and normalized remanence make these magnetosomes promising candidates for hyperthermic cancer treatment, and can enhance their applicability for other potential applications.

3.3. Summary

Specie/Growth Medium	K_c [kJ/m^3]	$K_u(\sigma)$ [kJ/m^3]	*Easy axis with respect to <111>[°]*
M. gryphiswaldense FSM	-11	12	20
M. magneticum FSM	-10	16(4)	15
M. magneticum MSGM-W	-10	12(4)	15
M. magneticum MSGM+W	3	16(4)	15
M. blakemorei MSGM+W	3	14(4)	0

Table 3.3: *Magnetotactic bacteria grown in different culture media, the corresponding magnetic anisotropies and the angle that the easy axis form with the chain axis found with the Stoner-Wohlfarth simulation at 300 K. The data of M. gryphiswaldense has been obtained from [72]*

In this Chapter, we have studied the magnetic response of *M. magneticum* AMB-1 under three different culture media (MSGM+W, MSGM-W and FSM), and *M. blakemorei* MV-1 in MSGM+W. We have seen how the use of different culture media can influence the magnetic properties of the magnetosome chain. In this way, we have studied the changes in the magnetic properties induced by the different cultures with the help of a modified Stoner-Wolfarth model which has allowed us to accurately reproduce their magnetic behaviour by considering different anisotropy contributions. As we summarize in Table 3.3, first of all, regarding the cubic magnetocrystalline anisotropy constant, for *M.magneticum* grown without Wolfe supplement (MSGM-W), the obtained K_c= -10 kJ/m^3 corresponds to the magnetocrystalline anisotropy value typically obtained in bulk magnetite at room temperature. On the other hand, for both *M. magneticum* and *M. blakemorei* grown with Wolfe supplement (MSGM+W), the Co ions in the medium gives rise to a doping of the magnetosomes with this element, increasing the magnetocrystalline constant to $K_c = 3$ kJ/m^3. In particular, for MSGM+W *M. magneticum* using XMCD we have seen that Co ions are incoporated as Co^{2+} into the magnetosome structure substituting Fe^{2+} located in octahedral places. The presence of Co^{2+} adds a large positive contribution to the magnetocrystalline anisotropy of magnetosomes, which enhances their remanence and coercivity, especially at low temperatures.

Second, the larger uniaxial anisotropy constant values obtained for *M. magneticum* grown in MSGM+W and FSM and for *M. blakemorei* grown in MSGM+W magnetosomes, indicate that these species synthesize magnetosomes with a greater elongation rate than those from *M. gryphiswaldense*.
Finally, we would like to highlight that while the *M. magneticum* and *M. gryphiswaldense* species have the effective anisotropy axis at similar angles, at 15° and 20°, with respect to the <111> direction, in the case of the *M. blakemorei* magnetosomes, their truncated-hexaoctahedral shape imposes a direction of easy magnetization in the [111] direction, $\hat{u}_{uni}$ at 0°, which is the chain direction.
In summary, although further work will be needed concerning certain aspects within the morphological and magnetic characterization (doping effect, ECT of magnetosome chain structure, ECT analysis of new magnetosome morphology, standardization of optimal culture conditions for *M. blakemorei*...etc), we believe that the rigorous analysis we have carried out can give an overall description of the differences in the magnetic response of the magnetosomes from different species, and opens the door to extend this analysis to other species of MTB and to expand future biomedical applications of the MTB and their magnetosomes.

Materials and Methods

Transmission Electron Microscopy(TEM)

Electron microscopy was performed on unstained cells adsorbed onto 300 mesh carbon-coated copper grids. TEM images were obtained with a JEOL JEM-1400 Plus electron microscope at an accelerating voltage of 120 kV. The particle size distribution was analyzed using a standard software for digital electron microscope image processing, ImageJ [110].

X-ray Magnetic Circular Dichroism (XMCD)

XMCD experiments were carried out on whole bacterium using the ALICE station [125, 126] at the PM3 beam line of BESSY II in Berlin, Germany. All XAS spectra were collected at room temperature. A drop of 5 μL of bacteria in aqueous solution with a concentration of c=1 $\times$ 10^{11} cell/ml was deposited onto silicon substrates. Data acquisition was done in transmission mode with the incoming circularly polarized (right helicity) x-rays impinging at normal incidence with

respect to the sample surface. A magnetic field of around ± 0.3 T was applied along the beam propagation direction. X-ray absorption spectra (I) were obtained across the Mn, Fe, Co and Cu edges with a step size of 0.2 eV. At each photon energy data was acquired at magnetic remanence after applying positive (I^+) and negative (I^-) magnetic fields to yield the XMCD signal given by $I^+ - I^-$.

Magnetometry on 3D bacterial arrangements

To orient the bacteria in 3D we prepared the agar solution with 2% of agar and 98% of water, keeping it at 80° C to mantain its liquidity. Then, we use a homemade VSM which is equipped with an oven. We introduce a metallic piece in the center of the two polar pieces of the VSM which will contain the eppendorf and we control the temperature through a thermocouple. Using the oven, temperature will be put at 80° C. 500 μl of magnetotactic bacteria with a concentration of around c=1 $\times$ 10^{11} cell/ml were resuspended inside 500μl of the agar solution, making a total volume of 1 ml. This eppendorf was then placed inside the VSM, which produces a uniform magnetic field of 1T orienting the bacteria while maintaining the temperature of the suspension at 80° C, thus preventing the polymerization of the agar. After 3 minutes, the field was turned off, and the sample was cooled using liquid nitrogen until the temperature reached around 0°. This caused the agar to solidify, trapping the bacteria, and keeping this solid state at room temperature. The magnetic mass of the concentration used is sufficient to measure the hysteresis loops in the eppendorf itself in the VSM and in this way we do not have to resort to more sophisticated techniques like the SQUID where the preparation of the sample is more complex by the own characteristics of the experimental technique.

Chapter 4

MTB as biorobots: Magnetic hyperthermia and remote control applications

MTB can in principle be better candidates for biomedical applications than the traditionally investigated non-magnetotactic bacteria and MNPs, since they combine the advantages of both worlds: the sensing, motility and other similar skills of the bacteria together with the magnetic control and heat release capacity of the MNPs. At the same time, they also exhibit some inherent properties, such as the hypoxic region targeting, that enhance their applicability for cancer therapy [37, 140].

We begin this Chapter by showing that MTB present high potential as magnetic hyperthermia agents for cancer treatment. To prove this, first their heating efficiency or specific absorption rate (SAR) is determined using both calorimetric and AC magnetometry methods at different magnetic field amplitudes and frequencies. In addition, the effect of the alignment of the bacteria in the direction of the field during the hyperthermia experiments is also investigated. The experimental results demonstrate that the biological structure of the magnetosome chain of magnetotactic bacteria is perfect to enhance the hyperthermia efficiency. Their improved heating efficiency together with the magnetic guidance, preference for low oxygen concentration regions, self-propulsion, etc. makes MTB ideal candidates to be used

as cancer treatment biorobots.
Afterwards, we study the guidance and response to magnetic fields of the MTB. In order to test their validity as biorobots, we need to make sure we can track them and guide them so that they target specific areas. For these tasks, we have designed and fabricated a laboratory station (Magnetotaxis platform) that combines guiding and tracking of the bacteria (See schematic representation in Fig. 4.1).
The workstation has been designed with the aim of being able to remotely control the MTB in a microfabricated maze with microfluidic channels. The guiding of MTB has been performed using a three-axis Helmholtz coil while the tracking has been carried out with optical microscopy. In order to better understand their motility behaviour, we have applied *ex situ* a detection and tracking algorithms.

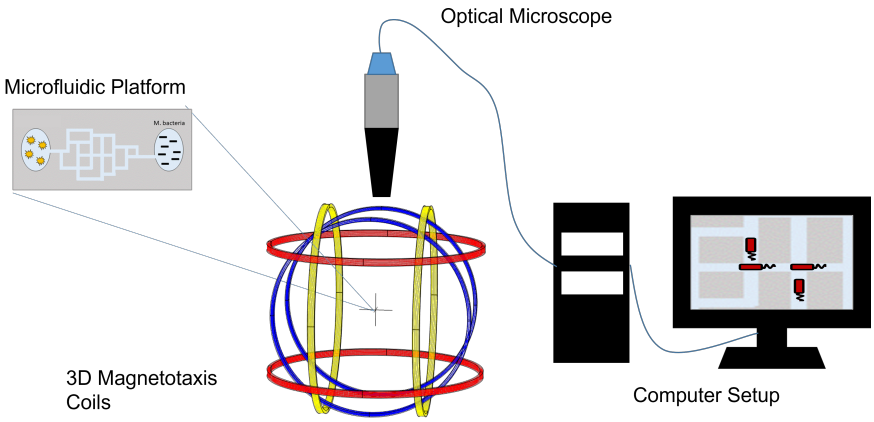

Figure 4.1: *Scheme of the design proposed for the workstation in order to control and monitor the movement of the magnetotactic bacteria under external applied fields.*

4.1. Magnetic hyperthermia

The main idea in hyperthermia mediated treatment of cancer is that, by raising the temperature of cancer cells up to a "therapeutic window", typically between 40 and 44°C , they can be deactivated (dead or driven to apoptosis) without affecting the healthy tissue. This is possible because in this range of temperatures, cancer cells have been shown to be more susceptible to heat than healthy ones [141]. In addition, it has also been shown that by rising the temperature, cancer cells become more susceptible to radio and chemotherapy [142, 143], thus improving the efficiency of these therapies. If we raise the temperature up to values higher than 50°C, a more violent (and less safe) cancer cell death is induced through thermal ablation [144]. Since 2011, the use of MNPs in cancer therapy through magnetic hyperthermia has been authorized in Europe, as a combined therapy with conventional radio and chemotherapies for the treatment of brain tumors. Currently, clinical trials are being carried out by MagForce AG® [145] on patients with brain, pancreatic, prostate, breast, and esophageal cancer. In 2014, the Food and Drug Administration (FDA) in USA also approved this procedure for the treatment of glioblastoma and prostate cancer.

In magnetic hyperthermia, the heat that increases the temperature of the tumor is produced by using magnetic nanoparticles under alternating magnetic field (AMF) with a define amplitude, H, and frequency, f. Under the action of the AMF, the magnetic moment of nanoparticles describes a hysteresis loop, whose area A is proportional to the dissipated energy. In this regard, the most important parameter in the quantification of the heating efficiency of any magnetic structure is their Specific Absortion Rate (SAR), also sometimes named as Specific Loss Power (SLP). This parameter is defined as the absorbed power normalised by the mass of nanoparticles under an applied alternating magnetic field. In other words, SAR denotes the ability of a sample to absorb energy from the magnetic field and transform it into heat. Commonly, the SAR units are given in W/g.

SAR depends on multiple factors [146–149]. First, it depends on the physicochemical properties of the nanoparticles such as size, shape, saturation magnetization, and magnetic anisotropy. Additionally, the interparticle magnetic interactions, which are closely related with the MNP concentration used, also affect their heating performance, generally tending to reduce the obtained SAR values. However, in special

arrangements as chain-like structures, it has been demonstrated that dipolar magnetic interactions can enhance the heating rates [150]. Last but not least, the MNPs dispersion medium also plays an important role in the heating performance, as the particles mechanical rotation with the magnetic field (Brownian rotation) can be highly suppressed within media with higher viscosity, such as biological environments.

Two different approaches are commonly used for SAR determination: calorimetric and magnetometric measurements. Calorimetry is the most widely used method because of its simplicity. As we have already explained, when a MNP sample is placed in an AMF, the sample absorbs energy from the field and directly transforms it into heat. This generated heat raises the temperature of the sample. Hence, under nearly adiabatic conditions, the SAR can be estimated from the initial heating rate of the sample, as given by equation [151]:

$$SAR = \frac{m_s}{m_n} C_p \frac{\Delta T}{\Delta t} \tag{4.1}$$

where C_p is the specific heat of the solvent, m_s is the mass of the solvent, m_n is the mass of the nanoparticles, and $\Delta T/\Delta t$ is the initial slope of the heating curves.

An alternative method to measure the heating efficiency is AC magnetometry. As commented before, SAR values can be directly obtained from the area A of the measured AC hysteresis loops, according to next equation:

$$SAR = \frac{f}{c} A = \frac{f}{c} \oint \mu_0 M_t \, dH_t \tag{4.2}$$

with M_t being the instantaneous magnetization at time t, H_t the sinusoidal magnetic field of frequency f at time t, and c the magnetic material weight concentration in the dispersing medium. The integration is done over a period of the oscillating magnetic field, $T = 2\pi/f$. In this Chapter we will use both methods to characterize the hyperthermic response of MTB. The combination of calorimetry and AC magnetometry allows us not only to check the performance of magnetotactic bacteria as heating agents (calorimetric method) but also to better understand the mechanisms behind their heating efficiency and how to optimize it (AC magnetometry).

Last but not least, it is important to mention that there are safety

clinical restrictions related to the application of an AMF during magnetic hyperthermia. According to the Faraday´s Law of induction, a radio frequency magnetic field generates associated electric fields. Since biological tissues have a certain electrical conductivity, these electric fields produce *eddy currents*. These eddy currents can give rise to a non specific heating, which above a certain limit can heat up healthy tissues and give rise to undesired damage. A good approximation to quantify the safety limit regarding the intensity of these eddy currents is considering the product of the applied magnetic field amplitude and frequency, $H \cdot f$. Brezovich and Atkinson [152] experimentally determined, by using a large coil surrounding the patient's torso, that a person was able to withstand without any pain AC magnetic fields for 1 hour if $H \cdot f < 4.85 \times 10^8$ Hz·A· m^{-1}. However, other authors [153, 154] have proposed that for clinical application, smaller coils could be employed, thereby increasing this limit. For example, Hergt *et al* [155] proposed a less restrictive limit of $H \cdot f < 5 \times 10^9$ Hz·A·m^{-1}. Therefore, in order to achieve an efficient magnetic hyperthermia treatment, magnetic nanoparticles should generate as much heat as possible, within the clinically acceptable $H \cdot f$ limits, at low particle dosages.

4.1.1. The potential of Magnetotactic bacteria as hyperthermia agents

In the present section, we want to test magnetotactic bacteria as nanobiots for cancer treatment by analyzing their performance as magnetic hyperthermia agents. As we have explained before, magnetic hyperthermia is a process in which controlled heating of magnetic nanoparticles located in the tumor can kill or deactivate cancer cells [141, 156, 157]. The superior magnetic properties of magnetosomes in magnetic hyperthermia have already been reported [43, 46]. However, as was mentioned in Chapter 1, there is only a couple of works that study the heating of the "whole" MTB, and the data presented is quite preliminary. Therefore, we have carried out a comprehensive study of the hyperthermic response of *Magnetospirillum gryphiswaldense* MSR-1 strain under different conditions: amplitude and frequency of the AMF, alignment of the bacteria, and medium viscosity. For the alignment studies, see Fig. 4.2, we employed suspensions of bacteria with a total magnetite concentration of ~ 0.15 mg $\cdot$ ml^{-1} in distilled water and in 2% w/v agar. To align the bacte-

ria, we resuspended 500 μl of the bacterial colloid in 500 μl of the agar solution at 80°C to maintain the solution in a liquid state, applied a uniform magnetic field of 0.5 T and finally cooled down the sample using liquid nitrogen, trapping the bacteria in a solidified state. The agar is used to restrict the physical rotation of the bacteria by increasing the viscosity of the medium [150], and also to align and fix them in different orientations allowing us to study the effect of the alignment on their heating efficiency. For the magnetic hyperthermia studies, a combination of calorimetric and AC magnetometry methods were employed [88, 156]. Further details about both methods can be found in Materials and Methods section. The AC hysteresis loops were measured by Dr. I. Rodrigo, using a homemade setup designed by the Group Mimaspec at the UPV/EHU. The measurements were carried out at room temperature (25°C), at selected frequencies, 149, 302, and 500 kHz, with an applied magnetic field ranging from 0 to 400 Oe. The calorimetric measurements were carried out by Dr. R. Das at the Functional Materials Lab, University of South Florida, using AC fields 0–600 Oe and 300 kHz.

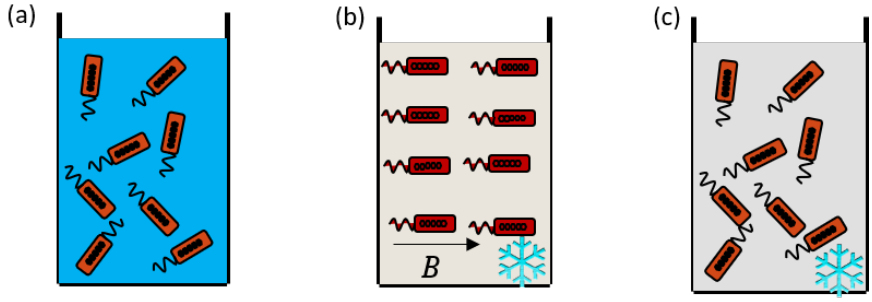

Figure 4.2: *Samples prepared for SAR measurements: a) bacteria dispersed in water; b) aligned bacteria in agar; c) random bacteria in agar.*

In Fig. 4.3 A we show the calorimetric measurements carried out at 300 kHz in bacteria dispersed in water clearly indicate that MTB can easily raise the temperature of the medium in a short amount of time, reaching the therapeutic window in just 3 min, by applying AC fields $\geq$ 300 Oe and considering an initial body temperature of 37 °C. Below 200 Oe, the heating is practically negligible for the bacteria concentration used ($\sim 9\times10^9$ bacteria $\cdot$ ml^{-1} $\simeq$ 0.15 mg$_{Fe_3O_4}$ $\cdot$ ml^{-1}).

This indicates that MTB can be used as efficient heating agents close to the Hergt safety limit ($H \cdot f < 5 \times 10^9$ Hz·A·m^{-1}). If a more drastic destruction of the cancer cells through thermal ablation was desired, higher fields and longer exposure times would let us increase the temperature above 50 °C (Δ T > 13°C), as shown in Fig. 4.3 A (although safety limits should be again taken into consideration [152–154]).
Once the MTB are inside the tumor area, their movement would be more restricted than in the blood vessels or in water, due to the higher viscosity of the medium and likely agglomeration issues. In order to investigate how this could affect their heating properties, we have repeated the magnetic hyperthermia measurements, this time in a more viscous medium, made of water with 2% agar. Moreover, we have also compared how the heating in this viscous medium varies if the bacteria are randomly dispersed or aligned parallel to the applied magnetic field (Fig. 4.2). The corresponding heating curves are also presented in Fig. 4.3 A.
We can see that, when the MTB are dispersed in the 2% agar medium and aligned parallel to the AC field, the obtained heating curves are very similar to those previously measured in water. This suggests that the bacteria dispersed in water tend also to align in the direction of the applied field, as expected due to magnetotaxis effect. However, heating rates decrease when the bacteria are randomly oriented and cannot align with the field. This indicates that in order to optimize the heating of magnetotactic bacteria for their use as hyperthermic nanobiots, they need to be as aligned as possible in the direction of the AC field applied during the hyperthermia treatment. Despite this, it must be remarked that even when the bacteria are randomly oriented, the obtained heating rates are comparable to those reported in the literature for high quality iron oxide nanoparticles (including magnetosomes), and we can reach temperatures inside the tumor within the therapeutic window for AC fields $\geq$300 Oe at 300 kHz. In order to compare the heating efficiency of MTB with those reported in the literature for other similar magnetic nanosystems, we can calculate the SAR. As can be seen in Figure 4.3 A, the SAR values obtained from calorimetric measurements reach over 2000 W·g^{-1} for the highest AC field amplitude applied, 600 Oe, at a frequency of 300 kHz when measured in water (or aligned in agar).
It is clear from these hyperthermia measurements that the alignment plays an important role in the heating efficiency of our MTB. In or-

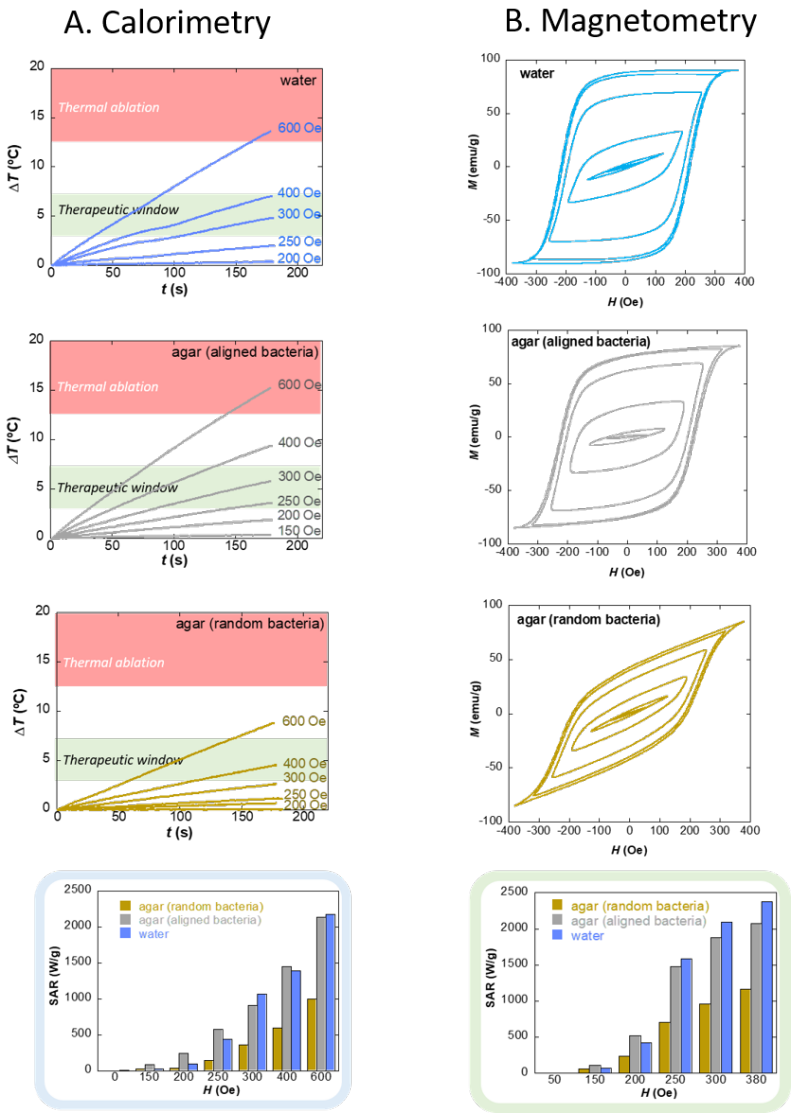

Figure 4.3: *Left column: Heating curves, Increase of temperature vs time; right column: AC hysteresis loops, M versus H, of magnetotactic bacteria in water, aligned bacteria in agar, random bacteria in agar, measured at AC fields 0–600 Oe and 300 kHz. In addition, the SAR values obtained from the heating curves and hysteresis loops are also represented.*

der to better understand the role of the alignment and the mechanisms behind the high heating efficiency of our bacteria, we have also carried out AC magnetometry measurements. Since the SAR is directly proportional to the hysteresis losses given by the area of the AC loops, in principle, the bigger this area, the better the heating efficiency. Therefore, it is easy to realize that the optimum shape of the AC loops in order to maximize the hysteresis losses would be a rectangular shape with high squareness, i.e., high coercivity and remanence for the AC field applied. Computer simulations carried out by different groups [69, 150, 158] suggest that aligned chain-like structures of magnetic nanoparticles, exhibiting a well-defined anisotropy axis, could give rise to AC loops that resemble this optimum shape. This has also been supported by the experimental results obtained in highly anisotropic nanostructures, such as magnetite nanorods [159]. Unfortunately, assembling this kind of chains and preventing them from collapsing is not an easy task, due to, among other factors, the presence of attractive magnetic interactions between chains. To this respect, MTB present a clear advantage: they already have a stable chain of magnetosomes, and since these magnetic chains are "embedded" inside the bacteria, they are efficiently separated from one another by the bacterial mass, thereby minimizing the effect of magnetic interactions.

The AC hysteresis loops measured for MSR-1 bacteria have been represented in Figure 4.3 B. There are several interesting issues to point out concerning the evolution of the AC loops. With increasing field, the AC loops evolve from the typical lancet shape of a minor loop at $H \leq 100$ Oe (extremely narrow, with low squareness and low maximum magnetization), to a more rectangular shape, for $H \geq 250$ Oe, as the field increases eventually resembling the optimum shape described before when the bacteria are parallel to the field. This confirms that MTB, when aligned in the direction of the AC field, behave as a ideal magnetic hyperthermia mediators. When the bacteria are randomly oriented, the AC loops are less squared and do not saturate, giving rise to lower hysteresis losses [88, 159, 160].

In addition, AC loops of MTB dispersed in water greatly resemble those of oriented MTB in agar: coercive field is virtually the same and magnetization remanence is only a little bit smaller in agar. This confirms, as already pointed out by calorimetric measurements, that an AC field of hundreds of kHz acts as a very efficient mechanical an-

chor for MTB: magnetization reversal in bacteria dispersed in water is driven by intrinsic dynamical processes, just like in fixed or nearly immobilized bacteria. Small differences between bacteria dispersed in water and oriented in agar would reflect basically different orientation degree. As a consequence, physical rotation (Brownian relaxation) of the chain of magnetosomes seems to play a very minor role in the heating efficiency of magnetotactic bacteria. This is not surprising, noting that magnetosome chains are embedded inside bacteria whose response velocity to external fields is much lower than that required to follow kHz excitations. This feature indicates that, contrary to what frequently happens with inorganic magnetic nanoparticles [157], MTB will still be able to provide high heating efficiency after penetrating and getting immobilized inside the tumor.

It must be noted that the SAR value obtained from AC magnetometry, $\sim$ 2400 W$\cdot$g^{-1} at 380 Oe, is appreciably higher than the one estimated from the calorimetric measurements, $\sim$ 1400 W$\cdot$g^{-1} at 400 Oe, both measured at the same frequency of 300 kHz. This divergence can be easily understood considering the difference between the temperature reached on the surface of the nanoparticles and the one reached in the medium. In these calorimetric measurements , we are deriving the heating efficiency of the nanoparticles from the average temperature measured in the medium. If there is enough concentration of magnetic material, the temperatures reached in the medium and on the surface of the nanoparticles are going to be similar. However, at low concentrations of magnetic material, the temperature in the medium can be appreciably lower than the one on the surface of the nanoparticles, and thereby, the SAR values obtained from measuring the temperature of the medium are going to be smaller than those indicated by AC magnetometry measurements. In our case, even if the concentration of bacteria employed is relatively high, 9 $\times$ 10^9 cells $\cdot$ ml^{-1}, the concentration of magnetic material is quite small, only 0.15 mg$_{Fe_3O_4}$ $\cdot$ ml^{-1} since these bacteria occupy a much larger volume than the one occupied by the nanoparticles. Increasing the applied field or the concentration of bacteria would diminish this problem. Another strategy to overcome this issue would be to increase the number of chains and/or magnetosomes per cell, something that in fact, is already being investigated [29, 161].

We commented before that using MTB instead of inorganic nanoparticles for magnetic hyperthermia treatment had a series of advantages,

mainly related to their capacity to self-propel, sense the local environment, be remotely guided, etc. It is important to remark that, on top of that, the heating efficiency we obtain from MTB is appreciably higher than the one we would obtain from the isolated magnetosomes. This can be clearly seen if we compare the SAR results obtained from AC magnetometry measurements for both MTB and isolated magnetosomes dispersed in water, for the same conditions of magnetic material concentration, 0.15 $mg_{Fe_3O_4} \cdot ml^{-1}$ (see Figure 4.4)

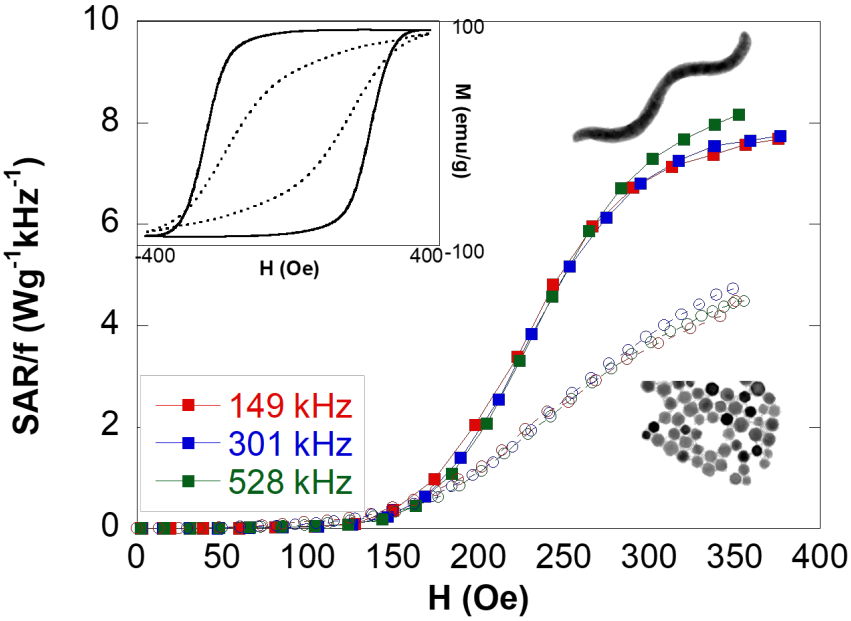

Figure 4.4: *SAR normalized by the frequency, SAR/f, measurements at different frequencies, 149, 301, and 528 kHz, for bacteria and magnetosomes dispersed in water. In the inset, AC hysteresis loops are presented corresponding to the bacteria (continuous line) and magnetosomes (dashed line) as obtained from AC magnetometry measurements (300 kHz).*

Figure 4.4 displays the evolution of the SAR values normalized by the frequency, *f*, for different magnetic field frequencies, as a function of the applied magnetic field amplitude, *H*, for MTB and magnetosomes dispersed in water (data has been taken from [43]). We can obtain relevant information from this comparison. First of all, we

see how the SAR values for both MTB and magnetosomes increase linearly with the magnetic field frequency, since the normalized magnetic losses, SAR/f, are almost independent of the applied frequency, as have already been observed in previous works on isolated magnetosomes [43]. Second, the SAR values for the magnetosomes dispersed in water are clearly lower than those obtained for MTB. While with magnetosomes we reach values of SAR/f close to 5 $W \cdot g^{-1}$ kHz^{-1}, with magnetotactic bacteria we can reach values up to around 8 $W \cdot g^{-1}$ kHz^{-1}. As we have explained, this can be associated to the easy alignment of the bacteria with the applied AC magnetic field, which increases the squareness of the hysteresis loops, as clearly depicted in the inset to Figure 4.4. And third, the evolution of the SAR curves as a function of the applied field for both magnetosomes and magnetotactic bacteria follows a similar trend, being negligible below ∼200 Oe and rapidly increasing above this value until it becomes saturated for field values around 380 Oe. As pointed out in [43] and [71], this is a clear hallmark of intrinsic hysteresis losses which can be modeled by a Stoner–Wohlfarth approach.

It must be remarked that the SAR values we are obtaining for these MTB compare very well with some of the highest SAR values reported in the literature for iron oxide based nanoparticles [157]. For example, Guardia *et al.* reported SAR values (from calorimetric measurements) of 1000 $W \cdot g^{-1}$ for magnetite nanocubes measured at 275 Oe and 325 kHz, and we are also obtaining similar SAR values at 300 Oe and 300 kHz [154]. This indicates that magnetotactic bacteria can heat as well as some of the best iron oxide based nanoparticles reported in the literature for magnetic hyperthermia applications.

Concerning the field amplitudes and frequencies we are applying in this study, if we want to work below the safety limit of $H \cdot f < 5 \times 10^9$ $Hz \cdot A \cdot m^{-1}$ [155], for example at 150 kHz, we should not apply more than 400 Oe for clinical hyperthermia. This would reduce the heating capacity of our nanobiots, being still high $\sim$ 1400 $W \cdot g^{-1}$ (obtained from calorimetric measurements). However, it must be noted that there is still an ongoing discussion about the validity of these limits, and some works have suggested that, depending on the area of the tissue treated, the safety limit can be increased up to 5×10^{10} $Hz \cdot A \cdot m^{-1}$, the same order of magnitude than most of our measurements [141].

To this day, very large efforts are being made to try to improve heating

efficiency by controlling the synthesis techniques, such as modifying the size of the particles, their shape, trying to improve the saturation magnetization of the particle, etc. In our opinion, our results clearly demonstrate that the biological structure of the magnetosome chain of magnetotactic bacteria is perfect to enhance the hyperthermia efficiency. This not only supports the use of these bacteria as biological nanobiots with high efficiency for magnetic hyperthermia but also allows the study of the adequate parameters to increase the SAR values in other types of nanostructures with controlled arrangement [162, 163].
In addition, we would like to remark that MTB have also high potential in other biomedical applications, such as magnetic particle imaging (MPI) agents. MPI is a novel medical imaging technique that relies on the nonlinearities of the time varying magnetization, and high order harmonics are used to map the position of the magnetic nanoparticles [164]. The suitability of isolated bacterial magnetosomes as MPI tracer has already been reported in the literature [165]. The highly squared AC hysteresis loops measured for the aligned bacteria (see Figure 4.3 B) present a high harmonic distortion on odd harmonics (3rd, 5th, 7th, ...), thus making these magnetotactic bacteria very promising candidates for MPI. This opens up the possibility of a combination of mapping and heat treatment using MTBs. In the next section, we are going to to explore the self-propulsion abilities and magnetic guidance of MTB.

4.2. Magnetotactic bacteria as microrobots

A major challenge in cancer therapy is the specificity of the delivery of the therapeutic agent to the target site, thereby minimizing any possible side effect. In this regard, MNPs have been extensively studied as an emerging technology in the last years [166, 167]. The main proposed idea is the use of magnetic field gradients in order to attract the MNPs to the region of interest (i.e. the tumor area) and latter act on it. For successful targeting, MNPs will need to counteract, among other things, the drag and buoyancy forces of the fluid. The magnetic force generated to do that depends on the field gradient and the magnetic moment of the MNPs [168]. For a given field gradient, this force is maximum when we reach magnetization saturation. In the case of the nanoparticles most commonly employed nowadays in these aplications, superparamagnetic iron oxide nanoparticles (SPI-

ONs), saturation only occurs at very high fields. In addition, producing the field gradients necessary to control the movement of the MNPs in deep tissues is challenging.

In this context, MTB present a number of advantages in comparison to MNPs that make them good candidates to implement therapy strategies locally addressed at the tumor site such as targeted drug delivery or magnetic hyperthermia. Indeed, we can take advantage of the self-propulsion capabilities provided by their flagella, and the magnetic moment of the magnetosome chain, made up of the sum of those of the individual magnetosomes, is high enough to allow the MTB to passively align along magnetic fields as small as the Earth's magnetic field (50 μT) in water environments. MTB can swim along the magnetic field lines (magnetotaxis), and therefore, no magnetic field gradients are necessary to guide them. Therefore, the navigation of the MTB can be controlled by torque-based actuation on the magnetosome chain, with low magnetic field amplitudes. In addition, it is less challenging to create a uniform magnetic field in a predefined direction than to create a magnetic field gradient between two points. The clinical platforms to guide MTB are much easier to implement than the gradient field approaches necessary for MNPs [169]. Finally, the navigation direction of the bacteria is also driven by the oxygen gradients present in the medium (aerotaxis) which favor their preference for hypoxic regions such as those in the tumors.

The majority of the guidance and motility studies on MTB have been carried out in artificially patterned microfluidic channels, where the movement of the bacteria is analyzed under optical microscopy [170–172]. However, it is worth mentioning that there are already a few *in vivo* experiments, using MTB in mice. Preliminary works in this field have shown that *M. magneticum* can navigate in capillaries and target mouse tumor xenografts [57] and that *Magnetococcus marinus* carrying drug-loaded nanoliposomes can be magnetically guided toward hypoxic regions of colorectal xenografts [140]. Here, 55% of the injected MTB penetrated into the hypoxic regions of the tumor, which is a large improvement in comparison to the targeting efficiency of other nanocarriers. However, to this day, the applicability of magnetotactic bacteria as biological microrobots is still in its very early development [173]. There are several other factors that must be taken into account for understanding the movement of MTB, i.e, how the magnetoaerotaxis works inside the blood vessels or how the hydro-

dynamic interactions between the flagellar propulsion and the flow within the blood vessels take place [174]. Once those are delimited, it will be more feasible to set up a successful strategy for MTB guidance.
In order to push forward the implementation of MTB as biological microrobots, we will show in the next sections the design and fabrication of the initial prototype of a Magnetotaxis Platform, shown in Fig. 4.5, that combines the tracking and the guiding of MTB. Our aim is to develop the setup needed for guiding and tracking those fast swimming microorganisms using optical feedback, and to present some preliminary data to validate this platform.

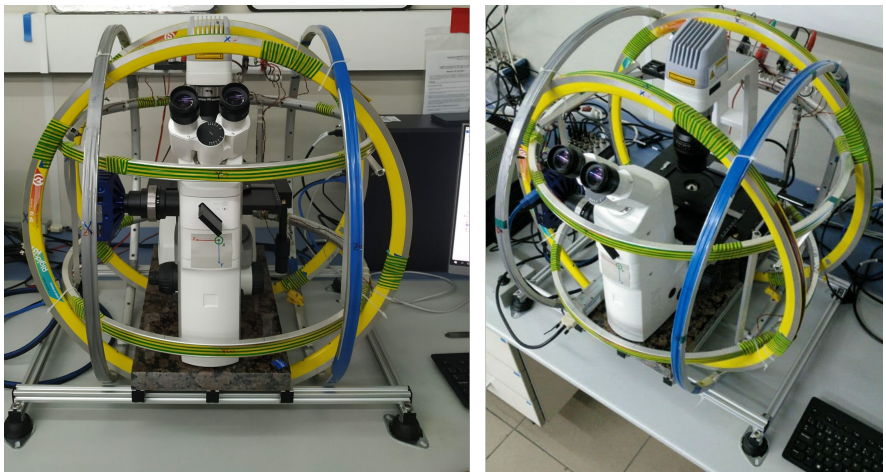

Figure 4.5: *Magnetotaxis Platform showcasing the triaxis coils and the optical microscope placed inside.*

4.2.1. Magnetotaxis Platform

Different sensitive parts make up the magnetotaxis platform we have designed and fabricated. In the following sections we summarize each one of the main parts, explaining their significance on the motility analysis of MTB. We divide the magnetotaxis platform in 3 key parts:

1. 3D Helmholtz Coils

2. High-Speed Optical Microscope

3. Microfluidic Platforms

3D Helmholtz Coils

Guidance of MTB is carried out using 3 pairs of Helmholtz coils. This allows us to induce static magnetic fields independently in the three axes, resulting in a 3D steering and alignment of the MTB. In the case of MTB, as we have explained, there is no need for field gradients. The direction of motion is controlled using the magnetic torque exerted on the bacterium. Compared to other systems that derive their propulsion energy from the magnetic field, the applied field in the magnetotaxis platform can be quite small in magnitude [172]. In table 3.1 the main characteristics of the coils are shown. The idea of having a 3D structure is not only to apply a magnetic field in any direction but also to be able to compensate the background magnetic field in the area where we have the sample. This background field is a combination of the Earth's magnetic field and the possible disturbance of magnetic elements close to the sample area. The calibration of the magnetic field is performed in the sample area (center of magnetotaxis coils) with a *Bartinton* three-axis fluxgate. We can reproduce the $\vec{H}$ field produced by the current I circulating in the coils using a matricial equation $H = H_0 + M \cdot I$, where H, H_0 and I are vectors and M is a 3×3 matrix. The main coefficients of matrix M are on the diagonal and range from $\sim$250 to 350 μT/A. The elements that are outside the diagonal help us to take into account possible geometric imperfections of the setup. The vector H_0 represents what we call background field (for $I = 0$) and it is convenient to calibrate it before each experiment. First, we apply the necessary proportional current to cancel this background field H_0, and then, through the calibrated value of M and the desired $\vec{H}$ field, we apply the proportional current I generating a magnetic field in the sample area able to orient and guide the MTB. All this process, where the gaussmeter is constantly communicating with the magnetic coils, has been properly automated using LabVIEW software [175]. However, although with the gaussmeter we can measure the local field at the center of the sample, it is difficult to know if this field is sufficiently homogeneous throughout the whole sample (microfluidic platforms where bacteria navigate). The homogeneity of the field at the sample location is important to optimize the control of the MTB and has been investigated using finite element simulations. Three dimensional FEM simulations with *COMSOL Multiphysics* [93] have been carried out to inspect the magnetic field homogeneity of our three axis Helmholtz coil system as well

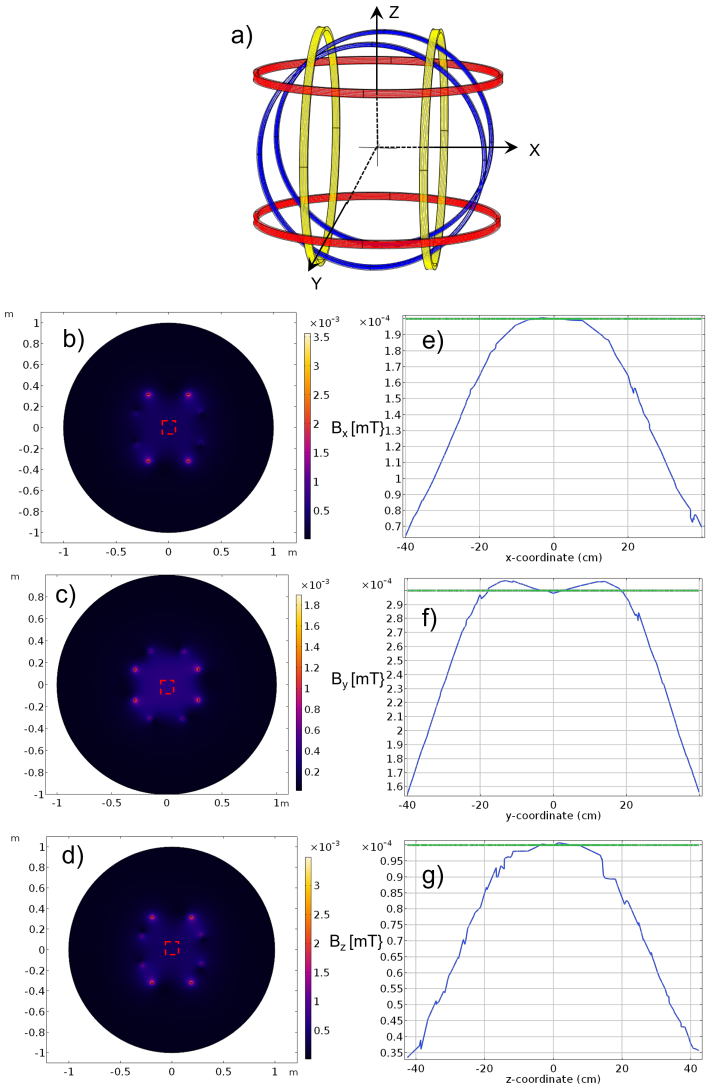

Figure 4.6: *(a) 3D coils. Left: YZ(b), XZ(c) and XY(d) magnetic field intensity [mT] obtained by FEM. Dashed box indicates the volume where the field is homogeneous (variation less than 5%). Right: B_x(e), B_y(f) and B_z(g) FEM magnetic field profiles along the center of the three-axis Helmholtz Coils. In green we show the target magnetic field.*

as to illustrate the viability of magnetic field compensation. Using the characteristic values shown in table 4.1, we have designed a 3D FEM model to reproduce the Helmholtz coils, which is presented in Fig. 4.6 a. Fig. 4.6 b-d represent the calculated magnetic field distribution for each plane of the 3D system. Our FEM simulations show that within a 10×10×10 cm^3 volume (marked in red), the field is very homogeneous with variations less than 5 % in intensity. Moreover, in Fig 4.6 e-g we see the magnetic field profile along the X, Y and Z coordinates. As an example, the green lines show a random magnetic field we want to reach: $\begin{pmatrix} 2 \\ 3 \\ 1 \end{pmatrix}$ Oe on the center of the coils. According to our FEM simulation, applying an intensity of $\begin{pmatrix} 0.66 \\ 1.28 \\ 0.35 \end{pmatrix}$A in the Helmholtz coils we would be able to reach the desired magnetic field value. More importantly, from these graphs, we can check that the obtained field is homogeneous enough in the region of interest (the maximum length of the microchannels where bacteria navigate is no greater that 1.7 cm). The good homogeneity generated by the magnetic field of our 3D Helmholtz Coils system, verified through FEM simulations, ensures the alignment and navigation of MTB in the desired direction along the microfluidic platform.

Coil	V(V)	R(Ω)	I_{max}(A)	B_{max} (μT)	ϕ_{Cu} (mm)	N	R (mm)
X	30	6-7	5	350	0.8	300	14
Y	30	6-7	5	350	0.8	300	19
Z	30	6-7	5	350	0.8	300	15

Table 4.1: *Features of the 3D Helmholtz coils. V represents the voltage of the power supplies. R the resistance of the copper coils. I_{max} the maximum current. ϕ_{Cu} the copper wire diameter. N is the number of turns of each Helmholtz Coil. R is the radius of the coil.*

High-Speed Optical Microscope

Optical microscopy has been proven to be an effective non-invasive method to study bacteria and other microorganisms and characterize their motility. However, tracking fast-swimming bacteria can be extremely challenging with current optical techniques. Due to the small physical size of MTB (approx. 2-5 μm length and 0.5 μm width for M. gryphiswaldense), imaging them requires high magnification and

large numerical aperture objectives. The limited working distance and depth of field associated with such lenses can make tracking MTB very challenging. Therefore, to track MTB it is essential to use a microscope that allows us to follow the trajectory of the fast moving MTB along large enough distances, without losing focus. To optimize this task, we have had to carefully select the following parameters in our microscope: Resolving power, magnification, working distance, depth of field (DOF), coherence of illumination, degree of aberration correction...
Considering all these factors, we installed in our magnetotaxis platform an inverted Zeiss Axio Vert.A1 FL Stand microscope, combined with a "Plan-Apochromat" 20X/0.8 objetive, and an AxioCam 506 camera. These components are summarized in Table 4.2. The selected configuration allowed us to obtain a good compromise between high magnification and large enough field of view (FOV) for the observation and subsequent analysis of magnetotactic bacteria's trajectories. A 20X magnification and 0.8 numerical aperture (N.A) provides us with an optimum resolution ($r \sim 0.5\mu$ m) of bacteria's size while at the same time, the FOV (624×510 μm) is large enough to be able to follow bacteria's trajectories for long time periods and distances while they navigate along the microfluidic channels.

Optical Features	
Magnification	20 X
Numerical Aperture (N.A)	0.8
Depth of Field (DOF)	5 μm
Working distance	550 μm
Field of View (FOV)	624x510 μm
Maximum frame rate	20 frames/s
Pixel size	4.54×4.54 μm
Bits depth	16 bits

Table 4.2: *Main features of the objective "Plan-Apochromat" 20X/0.8 and AxioCam 506.*

Microfluidic Platforms

The microfluidic platform on which MTB are going to navigate during the tests is a fundamental part of this investigation. Building microchannels which can simulate or emulate the blood vessels of the

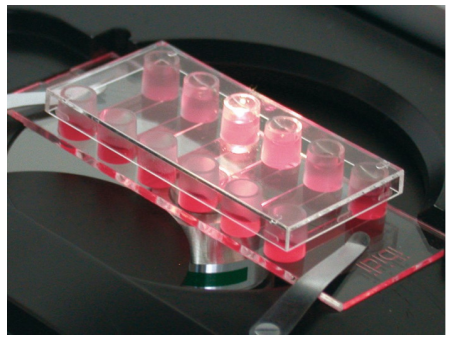

Figure 4.7: *Microfluidic platforms fabricated by Ibidi.*

human body and in which we can impose different conditions, such as flow velocity or oxygen concentration, is necessary for properly asserting the use of the MTB as microrobots. In our case, for this preliminary investigation and considering we are just setting up the first milestones of the magnetotaxis platform, we used commercial microfluidic channels, shown in Fig.4.7, from Ibidi company (*μ-Slide VI 0.1*). As depicted, several parallel channels are available, with a 40 μl reservoir at the end of each channel, where the MTB are initially placed. These channels present high optical quality, similar to that of glass, exhibiting extremely low birefringence and autofluorescence. This allows us to perform our experiments with uncompromised resolution and choice of wavelength. The lower part of the slide is covered by a polymer coverslip with a thickness of 180 μm. Since we are using a long working distance objective, we can focus at any stop along the whole microchannel's depth. However, we must take into account that bacteria can also swim upwards or downwards, and since these microfluidic channels have a channel height of 100 μm and the DOF of our objective is only 5 μm, it is possible to occasionally lose sight of MTB if they move up and down during the navigation. In order to paliate this issue, we have employed a robust tracking algorithm as will be described later.

4.2.2. Cell tracking

Cell tracking is an important tool for understanding the individual behavior of moving cells, as it allows intimate observation of the cell interaction with its surroundings and under different environmental conditions. In this sense, computational tools that can follow cells in

a time-lapse movie and quantify their dynamics are crucial for experiments involving live-cell imaging.
With our initial experimental set-up assembled, next we are going to demonstrate in detail how to use image processing and tracking algorithms to analyze large bacterial tracking data sets. Our aim is

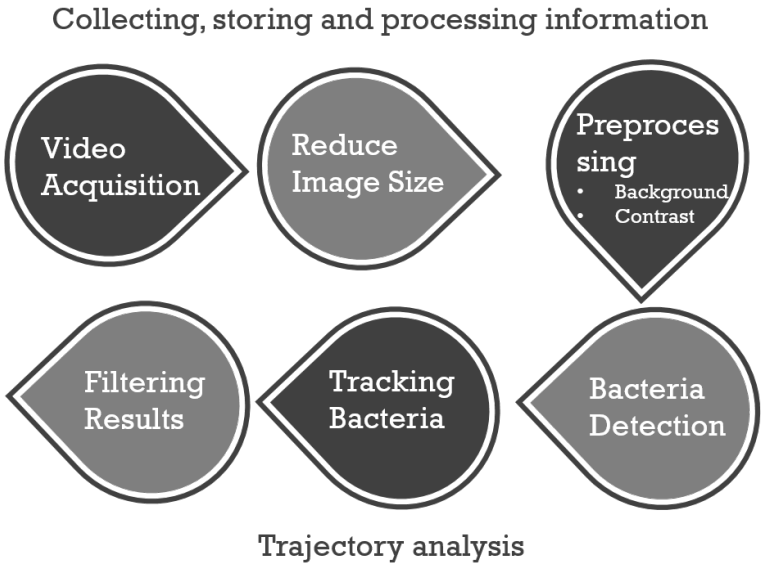

Figure 4.8: *The process of MTB detection, tracking and subsequent analysis.*

to actively track the MTB for relatively sufficiently long time periods and distances. There are several natural limits to adequately track fast swimming MTB under optical microscopy. For example, tracking of a single cell will be carried out with other motile bacteria in the vicinity. As such, the tracking algorithm must be able to operate efficiently within such environment. Also, as commented before, bacteria can swim upwards or downwards, complicating their tracking. Therefore, the system needs to be sufficiently robust not to lose the tracked bacterium in the presence of neighboring bacteria and when they swim out of the microscope's focal plane. Following the schematic process described in Fig. 4.8, we have implemented an optimized tracking process which provides us with a fast, high-throughput method for characterizing the motility of microorganisms based on standard imaging microscopy. Setting up a procedure for

the tracking of MTB is a very important point for the future analysis of the MTB trajectories under different experimental conditions such as flow speed, oxygen concentration, different microchannel patterns...etc.

4.2.3. Image processing

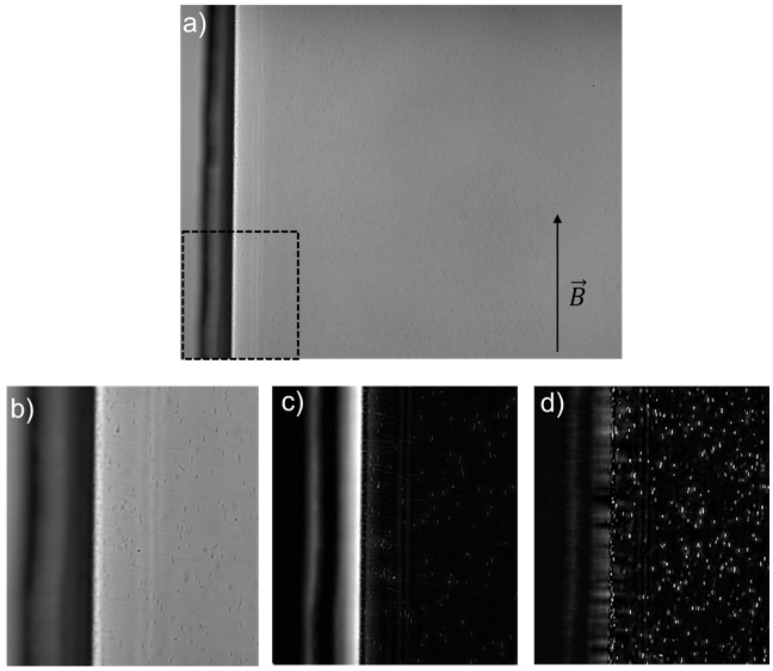

Figure 4.9: $624 \times 500 \mu m$ *frame of M. gryphiswaldense navigating within the microfluidic channels. The detail dashed box indicates the place where we apply digital magnification. (b) Crop of initial image without processing. (c) Background of the video. (d) Processed Video.*

The first step in our *ex-situ* tracking process is to optimize the video acquisition. This includes adjusting the brightness and contrast of the image, averaging images to reduce image noise, and correcting non-uniformities in the illumination. In Fig. 4.9 a we show the image of a microfludic channel with MTB as captured under the largest FOV that we can reach with our optical microscope (624 x 500 μm) (see section 4.2.2). Magnetotactic bacteria are navigating with an applied magnetic field of 1 mT parallel to the microchannel. To the left of the

image we see the edge of the microfluidic channel. The FOV captured with the camera is large enough to see many MTB navigating along long distances. To properly show the effects of our preprocessing, we can focus on the Region of interest (ROI) delimited by the dashed box. The obtained image is presented in Fig. 4.9 b. As depicted, this digitally magnified images allows to observe dozens of MTB navigating along the magnetic field lines. In order to improve and facilitate the tracking, we need to further process the previous images. As shown in Figs. 4.9 c-d, we use two basic processing techniques:

- Apply filtering for background noise reduction. The resulting image is presented Fig. 4.9 c. A certain amount of non-motile bacteria are always observed in the images. These bacteria are dead or dormant bacteria that settle at the bottom of the microchannels and adversely affect monitoring of the motile MTB. To eliminate them from our images, we perform an average on all the captured frames, obtaining a background of the complete video. By subtracting this image on each of the original frames, static objects and non-uniform illumination artefacts are eliminated.

- Enhance contrast and contours of MTB. The resulting image is presented in Fig. 4.9 d. This is carried out using ImageJ tools that enhance pixel intensity in each frame facilitating the bacteria detection.

After completing the preprocessing of the video, we can start tracking MTB. In order to analyze MTB trajectories, different options have been evaluated. Finally, due to its simple, sensible and practical user interface we have decided to use the dedicated program *Trackmate* [176].

4.2.4. *Trackmate*

TrackMate is a Fiji ImageJ [110] plugin where tracking is performed in a recorded video using a step-by-step interface. The user is guided through several consecutive stages, during which different tracking algorithms can be selected and configured, providing immediate visual feedback. This allows the user to be free to navigate back and forth and readjust different settings until a satisfactory result is reached. It is precisely the capacity to see intermediate results together with the ease of annotating numerical values of interest such as particle quality,

estimated diameter, track length or track displacement, what makes *TrackMate* such a powerful tool. To analyze the trajectories of the MTB, as was indicated in Fig. 4.8, first we use an algorithm to detect motile bacteria, then we track each of these bacteria, and finally we filter the results and select only those MTB we are interested in. To illustrate these steps, we are going to focus on the analysis of the trajectories of the MTB that were in Fig 4.9 d.

4.2.4.1. Bacteria detection

To automatically detect bacteria, we need to first choose an implemented detector in *Trackmate*. There are three possible detection algorithms all based on Laplacian of Gaussian (LOG) segmentation [176, 177]. We propose to use Difference of Gaussians (DOG) detector. This is ideal for small spot sizes, below 5 pixels, as in our case, and works faster than the other two. In principle, we set the estimated particle diameter to be around 4 μm, near the length value of *M. gryphyswaldense* bacteria.
In addition, to avoid detecting spurious spots not corresponding to MTB, we optimize the detection process by using a *quality* value parameter. This parameter measures the likelihood of each spot to be relevant following the properties of LOG filter. Spots with a quality lower that a specified threshold are discarded. The bacteria detected on the first frame of the video, after carrying out the previous steps, are shown in Fig. 4.10.

4.2.4.2. Bacteria tracking algorithm

Next step is to follow the selected MTB in the recorded video frame-by-frame, using one of the available particle-linking algorithms, or "trackers". In our case, we employed a Linear Assignment Problem (LAP) tracker. This is a linear motion tracker which can deal specifically with linear motion, or particles moving with a roughly constant velocity, as our MTB. The LAP tracker relies on a Kalman filter [178] to predict the most probable position of a particle undergoing constant velocity movement. This tracking algorithm addresses the principal challenges of Single Particle Tracking (SPT), namely high particle density, particle motion heterogeneity, temporary particle disappearance, and particle merging and splitting. As illustrated in Figure 4.11, algorithm first links particles between consecutive frames and then links the resulting track segments into complete trajectories, using three configuration fields, which are schematically represented in

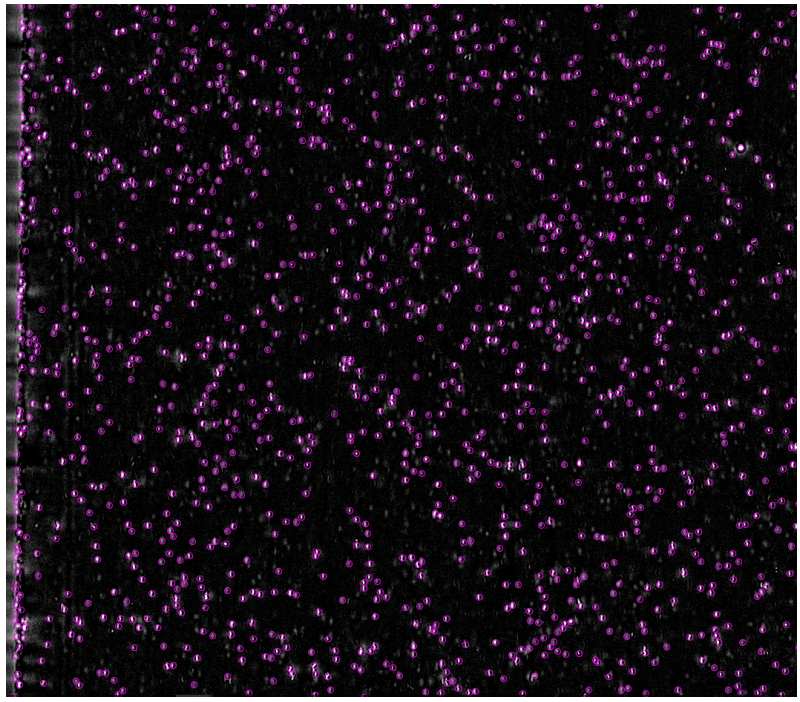

Figure 4.10: *Frame of the processed video where all the detected spots (bacterium) after filtering are shown.*

Fig. 4.11:

- *The maximal allowed linking distance (LD).* This value limits the spatial search range for candidate matching spots. If the spots in 2 consecutive frames are separated by more than the maximal allowed distance, the link is forbidden. Considering that the maximum velocity of the MTB is around 60 μm/s and the step time between frames is 0.133 s, then, we set the Linking Distance (LD) to be:

$$LD = v_{max} \cdot \tau = 60\frac{\mu m}{s} \cdot 0.133s \sim 8\mu m$$

- *The maximal distance for gap-closing (MD).* Once the linking distance has been established, this paramater represents the search radius after the prediction. In this case, we need to know the maximum difference between the maximum velocity value detected for a bacterium and the mean value of all trajectories.

This has been estimated to be $\Delta v_{max} = 20\frac{\mu m}{s}$. Therefore, we set the maximal distance (MD) as:

$$MD = \Delta v_{max} \cdot \tau = 20\frac{\mu m}{s} \cdot 0.133s \sim 3\mu m$$

- The third field deals with the detection of gap-closing events, and sets *the maximal frame interval* between two tracked spots to be bridged. After prediction, some Kalman filters might not get linked to a found spot. This event is called an occlusion. If the number of successive occlusions is too large, the track is considered terminated. After trying different values, we have been able to obtain optimal results setting the maximal frame interval to 2 frames duration.

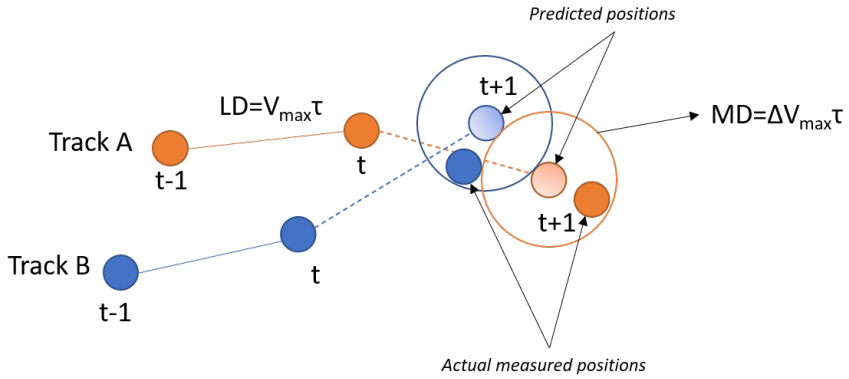

Figure 4.11: *Illustration of the parameters used for the tracking algorithm.*

4.2.5. Trajectory analysis results

After the previous process, the total number of detected trajectories in the video recorded corresponding to the area shown in Fig 4.10 is **3719**. In Fig. 4.12 a we plot a few selected trajectories. Among other things, these can be used to obtain important information about the motility of the MTB, such as their velocity distribution, as exemplified in Figure 4.12 b. We observe a bimodal distribution of median trajectory speeds. The one with a speed lower than 10 μm/s corresponds to inactive bacteria, while those with a speed higher than 10 μm/s correspond to active MTBs. Regarding the velocity of the

inactive bacteria, its non-zero speed is attributed to the residual flow of the medium in which the bacteria swim. In fact in [170] they use these trajectories of the inactive bacteria to determine the flow rate. From the analysis of the trajectories, we conclude that the active MTB exhibited magnetotactic behavior and swim along the magnetic field lines with an average swimming velocity of $49 \pm 10 \frac{\mu m}{s}$.

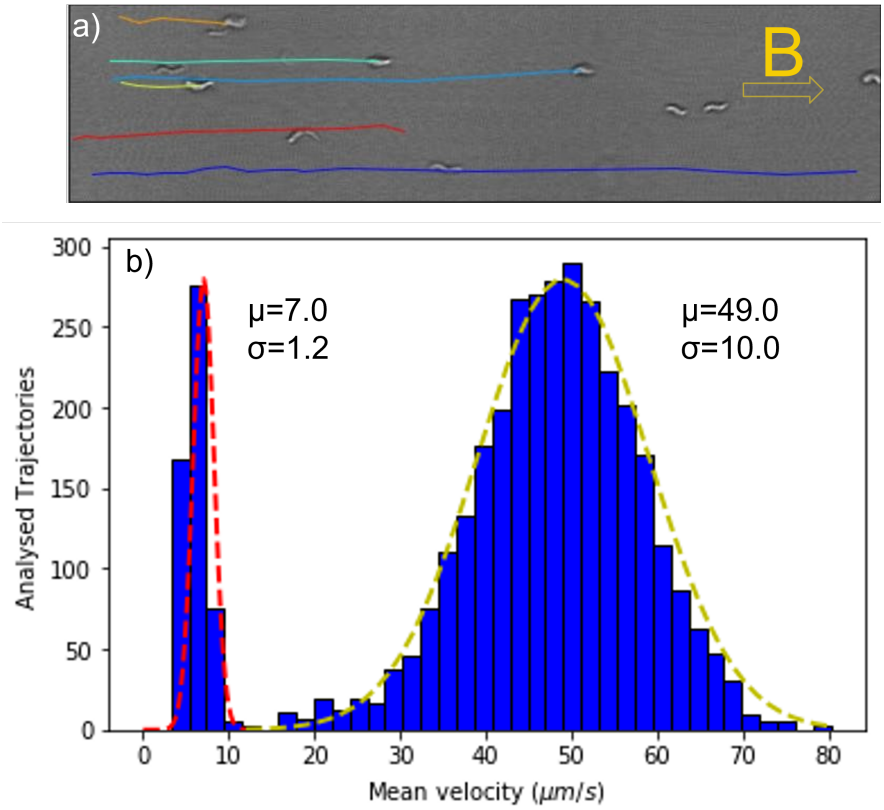

Figure 4.12: *(a)Directed navigation of M. gryphiswaldense in the direction of the magnetic field. Different colours show different trajectories. (b)Mean velocity distribution of bacteria for the analyzed trajectories.*

4.2.6. Summary

In this Chapter, we have proven that the species *M. gryphiswaldense* are very promising as magnetic hyperthermia agents for cancer treatment. Calorimetric measurements reveal that these bacteria can increase the temperature of the medium up to the therapeutic window (40–45°C) in less than 3 min by applying an external field with amplitude $\geq$ 300 Oe and frequency 300 kHz. We have also shown that the alignment of the bacteria with the field maximizes their heating efficiency. This has been clearly revealed in the AC hyperthermia magnetometrc measurements: hysteresis losses are maximized (reaching nearly optimum values) when the bacteria are parallel to the magnetic field. Moreover, the SAR values increase linearly with the magnetic field frequency, f, reaching a maximum SAR/f value of ~ 8 W $\cdot$ g^{-1} kHz^{-1} at 350 Oe, which is appreciably greater than those obtained for isolated magnetosomes.

In addition, in order to further explore the use of these MTB as nanobiots for cancer treatment, we have designed and assembled a Magnetotaxis Platform that allows us to guide and track them in a precise and controlled way. The platform consists on a system of three pairs of Helmholtz coils set, which can produce a 3D magnetic field to induce the alignment of the bacteria, and an inverted optical microscope, which has been optimized to attain both high enough magnification and field of view. Finally, we have also developed an *ex situ* tracking process using *TrackMate* to follow an analyze the trajectories of individual MTB in microfluidic channels. On our first tests commercial microfluidic channels have been used but the group is working on creating home made microfluidic channels that better mimick the characteristics of the blood vessels and tumoral regions inside the human body [179].

Materials and Methods

AC magnetometry

AC hyperthermia experiments were carried out in a homemade AMF magnetometer previously described by Garaio *et al.* [39]. It consists of an air-core inductor, part of a resonant circuit fed by a power amplifier. The dynamic magnetization, M_t , is obtained by a pick-up coil system composed of two coils wound in opposite directions. The signal is filtered using a low-pass filter with the cut-off frequency at 3 MHz. The magnetite mass concentration was determined from

saturation magnetization, measured using the VSM, and considering as reference the saturation magnetization value of 92.3 A $\cdot m^2 \cdot kg^{-1}$, corresponding to pure magnetite.

Calorimetric Measurements

The calorimetric hyperthermia was carried out with a commercial 4.2 kW Ambrell Easyheat LI 3542 system working at fixed frequency, 300 kHz. The measurements were done by Dr. Raja Das at the Functional Materials Laboratory, Department of Physics of the University of South Florida (USF). As in the case of AC magnetometry, suspensions of bacteria with a total magnetite concentration of $\sim$0.15 mg $\cdot$ ml^{-1} in distilled water and in 2% w/v agar were used for measurements and the AMF was tuned from 0 to 600 Oe.

Conclusions

We have focused first on using the magnetosomes as model magnetic nanoparticles for the development of tools and methodologies that can be extrapolated to other magnetic NPs. In this regard, the main advances are:

- A complete FEM model to calculate shape anisotropy energy density for a particular morphology has been designed.

- Using this model we have revealed the shape anisotropy density energy of regular polyhedrons like a cube, an octahedron or a truncated octahedron. Also we have proven that extrusions as small as 2% give rise to single easy axis anisotropies.

- Using ECT we have studied the morphology of *M. gryphiswaldense* magnetosomes, revealing that it slightly deviates from a perfect truncated octahedron, due to $\sim$7.5 % extrusion of one of the [001] directions and $\sim$10% extrusion of an adjacent [111] direction. This defines a quasi-uniaxial shape anisotropy density energy which is the key point to understand the 20° deviation of the magnetic moment of magnetosomes with respect to the chain axis.

- Using the shape anisotropy values obtained by FEM and an ECT analysis of the magnetosome chain, we have been able to simulate, within the framework of the Landau–Lifshitz–Gilbert model, the AC hystereis loops measured for MTB.

- A novel methodology based on a combination of EH and ET with a FEM optimization method has been presented as a powerful tool to reproduce the magnetization of different nanostructures.

Conclusions

Harvesting new MTB species is a very important task in order to expand their range of applications. With respect to the study of the magnetic properties of different MTB species, we highlight the following conclusions:

- Significant differences appear between the three species: *M. gryphiswaldense*, *M. magneticum* and *M. blakemorei*.
- The different culture media used to grow MTB can deeply influence their magnetic properties.
- Using XMCD we have seen that Co ions present in the culture medium (MSGM+W) are incorporated as Co^{2+} into the magnetosome structure substituing Fe^{2+} located in octahedral places. This substitution produces important changes in the magnetic properties.
- The magnetic behaviour changes appearing between species and culture media can be reproduced with the help of a modified Stoner-Wohlfarth model.
- In the case of *M. magneticum* grown without Wolfe supplement (MSGM-W) the obtained K_c= -10 kJ/m^3 corresponds to the magnetocrystalline anisotropy value typically obtained in bulk magnetite at room temperature. On the other hand, for both *M. magneticum* and *M.blakemorei* grown with Wolfe supplement (MSGM+W), the Co ions in the medium gives rise to a doping of the magnetosomes with this element, increasing the magnetocrystalline constant to K_c= 3 kJ/m^3. For all the analyzed species the uniaxial anisotropy value ranges between K_{uni}= 12(4) kJ/m^3-16(4) kJ/m^3.
- *M. magneticum* and *M. gryphiswaldense* species have the effective anisotropy axis at similar angles, at 15° and 20°, with respect to the <111> direction. In the case of the *M. blakemorei* magnetosomes, their truncated-hexaoctahedral shape imposes a direction of easy magnetization in the [111] direction, $\hat{u}_{uni}$ at 0°, which is the chain direction.

Finally, we have focused on the extraordinary and promising research area consisting on using the whole MTB as biorobots for cancer treatment:

Conclusions

- Calorimetric measurements reveal that these bacteria can increase the temperature of the medium up to the therapeutic window (40–45°C) in less than 3 min by applying an external field with amplitude $\geq$ 300 Oe and frequency 300 kHz.
- The magnetic alignment capacity of MTB maximizes the heating efficiency, increasing the SAR value from 5 $W \cdot g^{-1}$ kHz^{-1} from isolated magnetosomes to 8 $W \cdot g^{-1}$ kHz^{-1} for bacteria. Using magnetometric measurements we have revealed that this is because when the bacteria are parallel to the magnetic field, hysteresis losses are maximized.
- MTB can be guided by the application of a controlled magnetic field. We have designed and assembled a magnetotaxis platform together with a dedicated detection and tracking algorithm to further investigate this approach.

Bibliography

[1] R. Blakemore, "Magnetotactic bacteria," *Science*, vol. 190, no. 4212, pp. 377–379, 1975.

[2] R. E. Dunin-borkowski, M. R. Mccartney, R. B. Frankel, D. A. Bazylinski, and P. R. Buseck, "Magnetic Microstructure of Magnetotactic Bacteria by Electron Holography," *Science*, pp. 2–5, 1998.

[3] D. A. Bazylinski and R. B. Frankel, "Magnetosome formation in prokaryotes," *Nature Reviews Microbiology*, vol. 2, no. 3, pp. 217–230, 2004.

[4] D. Faivre and D. Schüler, "Magnetotactic bacteria and magnetosomes," *Chemical Reviews*, vol. 108, no. 11, pp. 4875–4898, 2008.

[5] D. A. Bazylinski, C. T. Lefèvre, and B. H. Lower, "Magnetotactic bacteria, magnetosomes, and nanotechnology," *Nanomicrobiology: Physiological and Environmental Characteristics*, vol. 97, pp. 39–74, 2014.

[6] J. R. Taylor and R. Stocker, "Trade-offs of chemotactic foraging in turbulent water," *Science*, vol. 338, no. 6107, pp. 675–679, 2012.

[7] R. Stocker, "Marine microbes see a sea of gradients," *Science*, vol. 338, no. 6107, pp. 628–633, 2012.

[8] K. Son, D. R. Brumley, and R. Stocker, "Live from under the lens: Exploring microbial motility with dynamic imaging and microfluidics," *Nature Reviews Microbiology*, vol. 13, no. 12, pp. 761–775, 2015.

[9] X. Garcia, S. Rafaï, and P. Peyla, "Light control of the flow of phototactic microswimmer suspensions," *Physical Review Letters*, vol. 110, no. 13, 2013.

[10] J. O. Kessler, "Hydrodynamic focusing of motile algal cells," *Nature*, vol. 313, no. 5999, pp. 218–220, 1985.

[11] E. Paster and W. S. Ryu, "The thermal impulse response of Escherichia coli," *Proceedings of the National Academy of Sciences of the United States of America*, vol. 105, no. 14, pp. 5373–5377, 2008.

[12] F. Popp, J. P. Armitage, and D. Schüler, "Polarity of bacterial magnetotaxis is controlled by aerotaxis through a common sensory pathway," *Nature Communications*, vol. 5, 2014.

[13] A. M. Spormann and R. S. Wolfe, "Chemotactic, magnetotactic and tactile behaviour in a magnetic spirillum," *FEMS Microbiology Letters*, vol. 22, no. 3, pp. 171–177, 1984.

[14] W. Lin and Y. Pan, "Temporal variation of magnetotactic bacterial communities in two freshwater sediment microcosms," *FEMS Microbiology Letters*, vol. 302, no. 1, pp. 85–92, 2010.

[15] C. Rensing, "Magnetoreception and Magnetosomes in Bacteria," *Microbe Magazine*, vol. 2, no. 10, pp. 512–512, 2007.

[16] R. B. Frankel, D. A. Bazylinski, M. S. Johnson, and B. L. Taylor, "Magneto-aerotaxis in marine coccoid bacteria," *Biophysical Journal*, vol. 73, no. 2, pp. 994–1000, 1997.

[17] R. B. Frankel and D. A. Bazylinski, "Magnetosomes and magneto-aerotaxis," *Contributions to Microbiology*, vol. 16, pp. 182–193, 2009.

[18] R. B. Frankel, T. J. Williams, and D. A. Bazylinski, "Magneto-Aerotaxis," *Magnetoreception and Magnetosomes in Bacteria*, pp. 1–24, 2006.

[19] F. F. Guo, W. Yang, W. Jiang, S. Geng, T. Peng, and J. L. Li, "Magnetosomes eliminate intracellular reactive oxygen species in Magnetospirillum gryphiswaldense MSR-1," *Environmental Microbiology*, vol. 14, no. 7, pp. 1722–1729, 2012.

[20] D. Muñoz, L. Marcano, R. Martín-Rodríguez, L. Simonelli, A. Serrano, A. García-Prieto, M. L. Fdez-Gubieda, and A. Muela, "Magnetosomes could be protective shields against metal stress in magnetotactic bacteria," *Scientific Reports*, vol. 10, no. 1, 2020.

[21] Z. S. Buchwald and J. A. Efstathiou, "Immunotherapy and radiation – A new combined treatment approach for bladder cancer?," *Bladder Cancer*, vol. 1, no. 1, pp. 15–27, 2015.

[22] R. B. Frankel, "Magnetic guidance of organisms.," *Annual review of biophysics and bioengineering*, vol. 13, pp. 85–103, 1984.

[23] B. H. Lower and D. A. Bazylinski, "The bacterial magnetosome: A unique prokaryotic organelle," *Journal of Molecular Microbiology and Biotechnology*, vol. 23, no. 1-2, pp. 63–80, 2013.

[24] P. Bender, L. Marcano, I. Orue, D. Alba Venero, D. Honecker, L. Fernández Barquín, A. Muela, and M. L. Fdez-Gubieda, "Probing the stability and magnetic properties of magnetosome chains in freeze-dried magnetotactic bacteria," *Nanoscale Advances*, vol. 2, no. 3, pp. 1115–1121, 2020.

[25] B. D. Cullity and C. D. Graham, *Introduction to Magnetic Materials (2nd Edition)*. Wiley, 2009.

[26] S. Blundell, *Magnetism in Condensed Matter*. Oxford ; *New York :Oxford University Press*, 2001.

[27] R. Prozorov, T. Prozorov, S. K. Mallapragada, B. Narasimhan, T. J. Williams, and D. A. Bazylinski, "Magnetic irreversibility and the Verwey transition in nanocrystalline bacterial magnetite," *Physical Review B - Condensed Matter and Materials Physics*, vol. 76, no. 5, pp. 1–10, 2007.

[28] C. T. Lefevre and D. A. Bazylinski, "Ecology, Diversity, and Evolution of Magnetotactic Bacteria," *Microbiology and Molecular Biology Reviews*, vol. 77, pp. 497–526, sep 2013.

[29] A. C. V. Araujo, F. Abreu, K. T. Silva, D. A. Bazylinski, and U. Lins, "Magnetotactic bacteria as potential sources of bioproducts," *Marine Drugs*, vol. 13, no. 1, pp. 389–430, 2015.

[30] R. Uebe and D. Schüler, "Magnetosome biogenesis in magnetotactic bacteria," *Nature Reviews Microbiology*, vol. 14, no. 10, pp. 621–637, 2016.

[31] F. Abreu, J. L. Martins, T. Souza Silveira, C. N. Keim, H. G. Lins de Barros, F. J. Filho, and U. Lins, "'Candidatus magnetoglobus multicellularis', a multicellular, magnetotactic prokaryote from a hypersaline environment," *International Journal of Systematic and Evolutionary Microbiology*, vol. 57, no. 6, pp. 1318–1322, 2007.

[32] M. L. Fdez-Gubieda, A. Muela, J. Alonso, A. García-Prieto, L. Olivi, R. Fernández-Pacheco, and J. M. Barandiarán, "Magnetite biomineralization in magnetospirillum gryphiswaldense: Time-resolved magnetic and structural studies," *ACS Nano*, vol. 7, pp. 3297–3305, apr 2013.

[33] T. Matsunaga, T. Sakaguchi, and F. Tadakoro, "Magnetite formation by a magnetic bacterium capable of growing aerobically," *Applied Microbiology and Biotechnology*, vol. 35, no. 5, pp. 651–655, 1991.

[34] S. Spring, R. Amann, W. Ludwig, K. H. Schleifer, D. Schüler, K. Poralla, and N. Petersen, "Phylogenetic Analysis of Uncultured Magnetotactic Bacteria from the Alpha-Subclass of Proteobacteria," *Systematic and Applied Microbiology*, vol. 17, no. 4, pp. 501–508, 1995.

[35] "Global cancer observatory." See https://gco.iarc.fr for information on global cancer statistics.

[36] Y. Chen, P. Jungsuwadee, M. Vore, D. A. Butterfield, and D. K. St. Clair, "Collateral damage in cancer chemotherapy: Oxidative stress in nontargeted tissues," *Molecular Interventions*, vol. 7, no. 3, pp. 147–156, 2007.

[37] M. L. Fdez-Gubieda, J. Alonso, A. García-Prieto, A. García-Arribas, L. Fernández Barquín, and A. Muela, "Magnetotactic bacteria for cancer therapy," *Journal of Applied Physics*, vol. 128, no. 7, p. 070902, 2020.

[38] Q. A. Pankhurst, N. K. Thanh, S. K. Jones, and J. Dobson, "Progress in applications of magnetic nanoparticles in

biomedicine," *Journal of Physics D: Applied Physics*, vol. 42, no. 22, 2009.

[39] E. Garaio, J. M. Collantes, F. Plazaola, J. A. Garcia, and I. Castellanos-Rubio, "A multifrequency eletromagnetic applicator with an integrated AC magnetometer for magnetic hyperthermia experiments," *Measurement Science and Technology*, vol. 25, no. 11, p. 115702, 2014.

[40] I. Rodrigo, I. Castellanos-Rubio, E. Garaio, O. K. Arriortua, M. Insausti, I. Orue, J. Á. García, and F. Plazaola, "Exploring the potential of the dynamic hysteresis loops via high field, high frequency and temperature adjustable AC magnetometer for magnetic hyperthermia characterization," *International Journal of Hyperthermia*, vol. 37, no. 1, pp. 976–991, 2020.

[41] A. S. Mathuriya, "Magnetotactic bacteria for cancer therapy," *Biotechnology Letters*, vol. 37, no. 3, pp. 491–498, 2015.

[42] A. Plan Sangnier, S. Preveral, A. Curcio, A. K. A. Silva, C. T. Lefèvre, D. Pignol, Y. Lalatonne, and C. Wilhelm, "Targeted thermal therapy with genetically engineered magnetite magnetosomes@RGD: Photothermia is far more efficient than magnetic hyperthermia," *Journal of Controlled Release*, vol. 279, pp. 271–281, 2018.

[43] A. Muela, D. Muñoz, R. Martín-Rodríguez, I. Orue, E. Garaio, A. Abad Díaz De Cerio, J. Alonso, J. Á. García, and M. L. Fdez-Gubieda, "Optimal Parameters for Hyperthermia Treatment Using Biomineralized Magnetite Nanoparticles: Theoretical and Experimental Approach," *Journal of Physical Chemistry C*, vol. 120, pp. 24437–24448, oct 2016.

[44] R. Le Fèvre, M. Durand-Dubief, I. Chebbi, C. Mandawala, F. Lagroix, J. P. Valet, A. Idbaih, C. Adam, J. Y. Delattre, C. Schmitt, C. Maake, F. Guyot, and E. Alphandéry, "Enhanced antitumor efficacy of biocompatible magnetosomes for the magnetic hyperthermia treatment of glioblastoma," *Theranostics*, vol. 7, no. 18, pp. 4618–4631, 2017.

[45] R. T. Liu, J. Liu, J. Q. Tong, T. Tang, W. C. Kong, X. W. Wang, Y. Li, and J. T. Tang, "Heating effect and biocompatibility of bacterial magnetosomes as potential materials used

in magnetic fluid hyperthermia," *Progress in Natural Science: Materials International*, vol. 22, no. 1, pp. 31–39, 2012.

[46] E. Alphandéry, I. Chebbi, F. Guyot, and M. Durand-Dubief, "Use of bacterial magnetosomes in the magnetic hyperthermia treatment of tumours: A review," *International Journal of Hyperthermia*, vol. 29, no. 8, pp. 801–809, 2013.

[47] E. Alphandéry, S. Faure, L. Raison, E. Duguet, P. A. Howse, and D. A. Bazylinski, "Heat production by bacterial magnetosomes exposed to an oscillating magnetic field," *Journal of Physical Chemistry C*, vol. 115, pp. 18–22, jan 2011.

[48] E. Alphandéry, A. Idbaih, C. Adam, J. Y. Delattre, C. Schmitt, F. Guyot, and I. Chebbi, "Development of non-pyrogenic magnetosome minerals coated with poly-l-lysine leading to full disappearance of intracranial U87-Luc glioblastoma in 100% of treated mice using magnetic hyperthermia," *Biomaterials*, vol. 141, pp. 210–222, 2017.

[49] E. Alphandéry, A. Idbaih, C. Adam, J. Y. Delattre, C. Schmitt, F. Gazeau, F. Guyot, and I. Chebbi, "Biodegraded magnetosomes with reduced size and heating power maintain a persistent activity against intracranial U87-Luc mouse GBM tumors," *Journal of Nanobiotechnology*, vol. 17, no. 1, 2019.

[50] D. Chang, M. Lim, J. A. Goos, R. Qiao, Y. Y. Ng, F. M. Mansfeld, M. Jackson, T. P. Davis, and M. Kavallaris, "Biologically targeted magnetic hyperthermia: Potential and limitations," *Frontiers in Pharmacology*, vol. 9, no. AUG, 2018.

[51] H. S. Huang and J. F. Hainfeld, "Intravenous magnetic nanoparticle cancer hyperthermia," *International Journal of Nanomedicine*, vol. 8, pp. 2521–2532, 2013.

[52] A. J. Clark, D. T. Wiley, J. E. Zuckerman, P. Webster, J. Chao, J. Lin, Y. Yen, and M. E. Davis, "CRLX101 nanoparticles localize in human tumors and not in adjacent, nonneoplastic tissue after intravenous dosing," *Proceedings of the National Academy of Sciences of the United States of America*, vol. 113, no. 14, pp. 3850–3854, 2016.

[53] A. Sokolov, M. M. Apodaca, B. A. Grzybowski, and I. S. Aranson, "Swimming bacteria power microscopic gears," *Proceedings of the National Academy of Sciences of the United States of America*, vol. 107, no. 3, pp. 969–974, 2010.

[54] W. T. Bull and W. B. Coley, "II. Observations upon the Operative Treatment of Hernia at the Hospital for the Ruptured and Crippled.," *Annals of surgery*, vol. 28, no. 5, pp. 577–604, 1898.

[55] S. Zhou, C. Gravekamp, D. Bermudes, and K. Liu, "Tumour-targeting bacteria engineered to fight cancer," *Nature Reviews Cancer*, vol. 18, pp. 727–743, dec 2018.

[56] Ferlay J, Ervik M, Lam F, Colombet M, Mery L, Piñeros M, Znaor A, Soerjomataram I, and Bray F, "Global Cancer Observatory: Cancer Today.," *International Agency for Research on Cancer*, vol. 68, no. 6, pp. 3–4, 2020.

[57] M. R. Benoit, D. Mayer, Y. Barak, I. Y. Chen, W. Hu, Z. Cheng, S. X. Wang, D. M. Spielman, S. S. Gambhir, and A. Matin, "Visualizing implanted tumors in mice with magnetic resonance imaging using magnetotactic bacteria," *Clinical Cancer Research*, vol. 15, no. 16, pp. 5170–5177, 2009.

[58] M. Mahmoudi, A. Tachibana, A. B. Goldstone, Y. J. Woo, P. Chakraborty, K. R. Lee, C. S. Foote, S. Piecewicz, J. C. Barrozo, A. Wakeel, B. W. Rice, C. B. Bell, and P. C. Yang, "Novel MRI Contrast Agent from Magnetotactic Bacteria Enables in Vivo Tracking of iPSC-derived Cardiomyocytes," *Scientific Reports*, vol. 6, p. 26960, 2016.

[59] E. Alphandéry, S. Faure, O. Seksek, F. Guyot, and I. Chebbi, "Chains of magnetosomes extracted from AMB-1 magnetotactic bacteria for application in alternative magnetic field cancer therapy," *ACS Nano*, vol. 5, no. 8, pp. 6279–6296, 2011.

[60] M. S. Tabatabaei, H. Girouard, and S. Martel, "Magnetotactic bacteria as micro-carriers of thermal ablation agents," in *International Conference on Manipulation, Automation and Robotics at Small Scales, MARSS 2017 - Proceedings*, 2017.

[61] D. Gandia, L. Gandarias, I. Rodrigo, J. Robles-García, R. Das, E. Garaio, J. Á. García, M. H. Phan, H. Srikanth, I. Orue,

J. Alonso, A. Muela, and M. L. Fdez-Gubieda, "Unlocking the Potential of Magnetotactic Bacteria as Magnetic Hyperthermia Agents," *Small*, vol. 15, p. 1902626, 2019.

[62] C. Chen, L. Chen, Y. Yi, C. Chen, L. F. Wu, and T. Song, "Killing of Staphylococcus aureus via magnetic hyperthermia mediated by magnetotactic bacteria," *Applied and Environmental Microbiology*, vol. 82, pp. 2219–2226, feb 2016.

[63] M. I. Nkandu, "Biomimicry as an Alternative Approach to Sustainability," *Architecture Research*, vol. 8, no. 1-11., 2018.

[64] J. S. Turner and R. C. Soar, "Beyond biomimicry: What termites can tell us about realizing the living building," *First International Conference on Industrialized, Intelligent Construction (I3CON)*, no. May, pp. 14–16, 2008.

[65] A. M. Huízar-Félix, D. Muñoz, I. Orue, C. Magén, A. Ibarra, J. M. Barandiarán, A. Muela, and M. L. Fdez-Gubieda, "Assemblies of magnetite nanoparticles extracted from magnetotactic bacteria: A magnetic study," *Applied Physics Letters*, vol. 108, p. 063109, feb 2016.

[66] H. Gojzewski, M. Makowski, A. Hashim, P. Kopcansky, Z. Tomori, and M. Timko, "Magnetosomes on surface: an imaging study approach," *Scanning*, vol. 34, pp. 159–169, may 2012.

[67] J. M. García-Ruiz, E. Nakouzi, E. Kotopoulou, L. Tamborrino, and O. Steinbock, "Biomimetic mineral self-organization from silica-rich spring waters," *Science Advances*, vol. 3, no. 3, 2017.

[68] S. Sturm, M. Siglreitmeier, D. Wolf, K. Vogel, M. Gratz, D. Faivre, A. Lubk, B. Büchner, E. V. Sturm, and H. Cölfen, "Magnetic Nanoparticle Chains in Gelatin Ferrogels: Bioinspiration from Magnetotactic Bacteria," *Advanced Functional Materials*, vol. 29, no. 45, 2019.

[69] C. Martinez-Boubeta, K. Simeonidis, A. Makridis, M. Angelakeris, O. Iglesias, P. Guardia, A. Cabot, L. Yedra, S. Estradé, F. Peiró, Z. Saghi, P. a. Midgley, I. Conde-Leborán, D. Serantes, and D. Baldomir, "Learning from nature to improve the heat generation of iron-oxide nanoparticles for magnetic hyperthermia applications," *Scientific Reports*, vol. 3, p. 1652, 2013.

[70] S. A. Corr, S. J. Byrne, R. Tekoriute, C. J. Meledandri, D. F. Brougham, M. Lynch, C. Kerskens, L. O'Dwyer, and Y. K. Gun'ko, "Linear assemblies of magnetic nanoparticles as MRI contrast agents," *Journal of the American Chemical Society*, vol. 130, no. 13, pp. 4214–4215, 2008.

[71] I. Orue, L. Marcano, P. Bender, A. García-Prieto, S. Valencia, M. A. Mawass, D. Gil-Cartón, D. Alba Venero, D. Honecker, A. García-Arribas, L. Fernández Barquín, A. Muela, and M. L. Fdez-Gubieda, "Configuration of the magnetosome chain: A natural magnetic nanoarchitecture," *Nanoscale*, vol. 10, pp. 7407–7419, apr 2018.

[72] L. Marcano, *Magnetic and Structural Characterization of Magnetite Nanoparticles Synthesized by Magnetotactic Bacteria*. PhD thesis, 2018.

[73] D. Lisjak and A. Mertelj, "Progress in Materials Science Anisotropic magnetic nanoparticles : A review of their properties , syntheses and potential applications," *Progress in Materials Science*, vol. 95, pp. 286–328, 2018.

[74] H. Khurshid, J. Alonso, Z. Nemati, M. H. Phan, P. Mukherjee, M. L. Fdez-Gubieda, J. M. Barandiarán, and H. Srikanth, "Anisotropy effects in magnetic hyperthermia: A comparison between spherical and cubic exchange-coupled FeO/Fe3O4 nanoparticles," *Journal of Applied Physics*, vol. 117, p. 17A337, may 2015.

[75] Ó. Iglesias and A. Labarta, "Finite-size and surface effects in maghemite nanoparticles: Monte Carlo simulations," *Physical Review B - Condensed Matter and Materials Physics*, vol. 63, no. 18, 2001.

[76] M. E. Mchenry, D. E. Laughlin, M. Science, and C. Mellon, *Magnetic Properties of Metals and Alloys*. Elsevier, fifth edit ed., 2014.

[77] G. F. Dionne, *Anisotropy and Magnetoelastic Properties*. Springer, 2009.

[78] J. Restrepo, Y. Labaye, and J. M. Greneche, "Surface anisotropy in maghemite nanoparticles," *Physica B: Condensed Matter*, vol. 384, pp. 221–223, 2006.

[79] J. Mazo-Zuluaga, J. Restrepo, and J. Mejía-López, "Surface anisotropy of a Fe3O4 nanoparticle: A simulation approach," *Physica B: Condensed Matter*, vol. 398, no. 2, pp. 187–190, 2007.

[80] H. Kachkachi, A. Ezzir, M. Noguès, and E. Trouc, "Surface effects in nanoparticles: Application to maghemite γ-Fe2O3," *European Physical Journal B*, vol. 14, no. 4, pp. 681–689, 2000.

[81] J. Mazo-Zuluaga, J. Restrepo, and J. Mejía-López, "Effect of surface anisotropy on the magnetic properties of magnetite nanoparticles: A Heisenberg-Monte Carlo study," *Journal of Applied Physics*, vol. 103, no. 11, 2008.

[82] R. H. Kodama and A. E. Berkowitz, "Atomic-scale magnetic modeling of oxide nanoparticles," *Physical Review B - Condensed Matter and Materials Physics*, vol. 59, no. 9, pp. 6321–6336, 1999.

[83] J. L. Dormann, D. Fiorani, and E. Tronc, "On the models for interparticle interactions in nanoparticle assemblies: comparison with experimental results," *Journal of Magnetism and Magnetic Materials*, vol. 202, no. 1, pp. 251–267, 1999.

[84] M. F. Hansen and S. Mørup, "Models for the dynamics of interacting magnetic nanoparticles," *Journal of Magnetism and Magnetic Materials*, vol. 184, no. 3, pp. L262–274, 1998.

[85] R. Moreno, S. Poyser, D. Meilak, A. Meo, S. Jenkins, V. K. Lazarov, G. Vallejo-Fernandez, S. Majetich, and R. F. Evans, "The role of faceting and elongation on the magnetic anisotropy of magnetite Fe3O4 nanocrystals," *Scientific Reports*, vol. 10, no. 1, pp. 1–14, 2020.

[86] B. Devouard, M. Pósfai, X. Hua, D. A. Bazylinski, R. B. Frankel, and P. R. Buseck, "Magnetite from magnetotactic bacteria: Size distributions and twinning," *American Mineralogist*, vol. 83, no. 11-12 PART 2, pp. 1387–1398, 1998.

[87] G. Singh, H. Chan, A. Baskin, E. Gelman, N. Repnin, P. Král, and R. Klajn, "Self-assembly of magnetite nanocubes into helical superstructures," *Science*, vol. 345, no. 6201, pp. 1149–1153, 2014.

[88] Z. Nemati, J. Alonso, I. Rodrigo, R. Das, E. Garaio, J. Á. García, I. Orue, M.-H. Phan, and H. Srikanth, "Improving the Heating Efficiency of Iron Oxide Nanoparticles by Tuning Their Shape and Size," *The Journal of Physical Chemistry C*, vol. 122, pp. 2367–2381, feb 2018.

[89] I. Castellanos-Rubio, I. Rodrigo, R. Munshi, O. Arriortua, J. S. Garitaonandia, A. Martinez-Amesti, F. Plazaola, I. Orue, A. Pralle, and M. Insausti, "Outstanding heat loss in nanooctahedra above 20 nm in size: from wustite-rich nanoparticles to magnetite single-crystals," *Nanoscale*, vol. 11, pp. 16635–16649, sep 2019.

[90] J. Lee and S. H. Ko, "Fundamentals of hierarchical nanostructures," *RSC Nanoscience and Nanotechnology*, vol. 2015-Janua, no. 35, pp. 7–25, 2015.

[91] S. Mann, T. T. Moench, and R. J. Williams, "A high resolution electron microscopic investigation of bacterial magnetite. Implications for crystal growth," *Proceedings of the Royal Society of London - Biological Sciences*, vol. 221, pp. 385–393, 1984.

[92] L. Marcano, D. Munoz, R. Martín-Rodríguez, I. Orue, J. Alonso, A. García-Prieto, A. Serrano, S. Valencia, R. Abrudan, L. Fernández Barquín, A. García-Arribas, A. Muela, and M. L. Fdez-Gubieda, "Magnetic Study of Co-Doped Magnetosome Chains," *Journal of Physical Chemistry C*, vol. 122, no. 13, pp. 7541–7550, 2018.

[93] COMSOL, "COMSOL Multiphysics ® Modeling Software v.5.4," 2016.

[94] D. X. Chen, E. Pardo, and A. Sanchez, "Demagnetizing factors of rectangular prisms and ellipsoids," *IEEE Transactions on Magnetics*, vol. 38, no. 4 II, pp. 1742–1752, 2002.

[95] Y. Xia, Y. Xiong, B. Lim, and S. E. Skrabalak, "Shape-controlled synthesis of metal nanocrystals: Simple chemistry

meets complex physics?," *Angew Chem Int Ed Engl*, vol. 48, no. 1, pp. 60–103, 2009.

[96] N. A. Usov and J. M. Barandiarán, "Magnetic nanoparticles with combined anisotropy," *Journal of Applied Physics*, vol. 112, no. 5, p. 053915, 2012.

[97] A. Körnig, M. A. Hartmann, C. Teichert, P. Fratzl, and D. Faivre, "Magnetic force imaging of a chain of biogenic magnetite and Monte Carlo analysis of tip-particle interaction," *Journal of Physics D: Applied Physics*, vol. 47, no. 23, p. 235403, 2014.

[98] E. Barati and M. Cinal, "Gilbert damping in binary magnetic multilayers," *Physical Review B*, vol. 95, no. 13, 2017.

[99] W. T. Coffey, D. S. Crothers, J. L. Dormann, Y. P. Kalmykov, E. C. Kennedy, and W. Wernsdorfer, "Thermally activated relaxation time of a single domain ferromagnetic particle subjected to a uniform field at an oblique angle to the easy axis: Comparison with experimental observations," *Physical Review Letters*, vol. 80, no. 25, pp. 5655–5658, 1998.

[100] H. Lichte and M. Lehmann, "Electron holography - Basics and applications," *Reports on Progress in Physics*, vol. 71, no. 1, 2008.

[101] M. R. McCartney and D. J. Smith, "Electron holography: Phase imaging with nanometer resolution," *Annual Review of Materials Research*, vol. 37, pp. 729–767, 2007.

[102] A. Tonomura, T. Matsuda, J. Endo, T. Arii, and K. Mihama, "Holographic interference electron microscopy for determining specimen magnetic structure and thickness distribution," *Physical Review B*, vol. 34, no. 5, pp. 3397–3402, 1986.

[103] A. Fukuhara, K. Shinagawa, A. Tonomura, and H. Fujiwara, "Electron holography and magnetic specimens," *Physical Review B*, vol. 27, no. 3, pp. 1839–1843, 1983.

[104] B. G. Frost and T. L. Jenkins, "On the interpretation of magnetic and electric fields imaged by low- magnification off-axis electron holography," *Journal of Microscopy*, vol. 187, no. 2, pp. 85–95, 1997.

[105] S. Ghaisari, M. Winklhofer, P. Strauch, S. Klumpp, and D. Faivre, "Magnetosome Organization in Magnetotactic Bacteria Unraveled by Ferromagnetic Resonance Spectroscopy," *Biophysical Journal*, vol. 113, no. 3, pp. 637–644, 2017.

[106] A. U. Gehring, H. Fischer, M. Charilaou, and I. García-Rubio, "Magnetic anisotropy and Verwey transition of magnetosome chains in Magnetospirillum gryphiswaldense," *Geophysical Journal International*, vol. 187, no. 3, pp. 1215–1221, 2011.

[107] E. T. Simpson, T. Kasama, M. Pósfai, P. R. Buseck, R. J. Harrison, and R. E. Dunin-Borkowski, "Magnetic induction mapping of magnetite chains in magnetotactic bacteria at room temperature and close to the Verwey transition using electron holography," *Journal of Physics: Conference Series*, pp. 108–121, 2005.

[108] D. N. Mastronarde, "Automated electron microscope tomography using robust prediction of specimen movements," *Journal of Structural Biology*, vol. 152, no. 1, pp. 36–51, 2005.

[109] J. R. Kremer, D. N. Mastronarde, and J. R. McIntosh, "Computer visualization of three-dimensional image data using IMOD," *Journal of Structural Biology*, vol. 116, no. 1, pp. 71–76, 1996.

[110] J. Schindelin, I. Arganda-Carreras, E. Frise, V. Kaynig, M. Longair, T. Pietzsch, S. Preibisch, C. Rueden, S. Saalfeld, B. Schmid, J. Y. Tinevez, D. J. White, V. Hartenstein, K. Eliceiri, P. Tomancak, and A. Cardona, "Fiji: An open-source platform for biological-image analysis," *Nature Methods*, vol. 9, no. 7, pp. 676–682, 2012.

[111] E. F. Pettersen, T. D. Goddard, C. C. Huang, G. S. Couch, D. M. Greenblatt, E. C. Meng, and T. E. Ferrin, "UCSF Chimera - A visualization system for exploratory research and analysis," *Journal of Computational Chemistry*, vol. 25, no. 13, pp. 1605–1612, 2004.

[112] K. Harada, A. Tonomura, Y. Togawa, T. Akashi, and T. Matsuda, "Double-biprism electron interferometry," *Applied Physics Letters*, vol. 84, no. 17, pp. 3229–3231, 2004.

[113] D. Wolf, A. Lubk, H. Lichte, and H. Friedrich, "Towards automated electron holographic tomography for 3D mapping of electrostatic potentials," *Ultramicroscopy*, vol. 110, no. 5, pp. 390–399, 2010.

[114] Y. Zhang, X. Zhang, W. Jiang, Y. Li, and J. Li, "Semicontinuous culture of Magnetospirillum gryphiswaldense MSR-1 cells in an autofermentor by nutrient-balanced and isosmotic feeding strategies," *Applied and Environmental Microbiology*, vol. 77, no. 17, pp. 5851–5856, 2011.

[115] A. Fernández-Castané, H. Li, O. R. Thomas, and T. W. Overton, "Development of a simple intensified fermentation strategy for growth of Magnetospirillum gryphiswaldense MSR-1: Physiological responses to changing environmental conditions," *New Biotechnology*, vol. 46, pp. 22–30, 2018.

[116] J. B. Sun, J. H. Duan, S. L. Dai, J. Ren, L. Guo, W. Jiang, and Y. Li, "Preparation and anti-tumor efficiency evaluation of doxorubicin-loaded bacterial magnetosomes: Magnetic nanoparticles as drug carriers isolated from Magnetospirillum gryphiswaldense," *Biotechnology and Bioengineering*, vol. 101, no. 6, pp. 1313–1320, 2008.

[117] K. T. Silva, P. E. Leão, F. Abreu, J. A. López, M. L. Gutarra, M. Farina, D. A. Bazylinski, D. M. Freire, and U. Lins, "Optimization of magnetosome production and growth by the magnetotactic vibrio Magnetovibrio blakemorei strain MV-1 through a statistics-based experimental design," *Applied and Environmental Microbiology*, vol. 79, no. 8, pp. 2823–2827, 2013.

[118] Y. Liu, G. R. Li, F. F. Guo, W. Jiang, Y. Li, and L. J. Li, "Large-scale production of magnetosomes by chemostat culture of Magnetospirillum gryphiswaldense at high cell density," *Microbial Cell Factories*, vol. 9, 2010.

[119] I. Ali, C. Peng, Z. M. Khan, and I. Naz, "Yield cultivation of magnetotactic bacteria and magnetosomes: A review," *Journal of Basic Microbiology*, vol. 57, no. 8, pp. 643–652, 2017.

[120] K. L. Thomas-Keprta, S. J. Clemett, D. A. Bazylinski, J. L. Kirschvink, D. S. McKay, S. J. Wentworth, H. Vali, E. K.

Gibson, M. F. McKay, and C. S. Romanek, "Truncated hexa-octahedral magnetite crystals in ALH84001: Presumptive biosignatures," *Proceedings of the National Academy of Sciences of the United States of America*, vol. 98, no. 5, pp. 2164–2169, 2001.

[121] C. D. Yang, H. Takeyama, T. Tanaka, and T. Matsunaga, "Effects of growth medium composition, iron sources and atmospheric oxygen concentrations on production of luciferase-bacterial magnetic particle complex by a recombinant Magnetospirillum magneticum AMB-1," *Enzyme and Microbial Technology*, vol. 29, no. 1, pp. 13–19, 2001.

[122] U. Heyen and D. Schüler, "Growth and magnetosome formation by microaerophilic Magnetospirillum strains in an oxygen-controlled fermentor," *Applied Microbiology and Biotechnology*, vol. 61, no. 5-6, pp. 536–544, 2003.

[123] J. Li, N. Menguy, M. A. Arrio, P. Sainctavit, A. Juhin, Y. Wang, H. Chen, O. Bunau, E. Otero, P. Ohresser, and Y. Pan, "Controlled cobalt doping in the spinel structure of magnetosome magnetite: New evidences from element- and site-specific X-ray magnetic circular dichroism analyses," *Journal of the Royal Society Interface*, vol. 13, no. 121, 2016.

[124] S. Staniland, B. Ward, A. Harrison, G. Van Der Laan, and N. Telling, "Rapid magnetosome formation shown by real-time x-ray magnetic circular dichroism," *Proceedings of the National Academy of Sciences of the United States of America*, vol. 104, no. 49, pp. 19524–19528, 2007.

[125] R. Abrudan, F. Brüssing, R. Salikhov, J. Meermann, I. Radu, H. Ryll, F. Radu, and H. Zabel, "ALICE - An advanced reflectometer for static and dynamic experiments in magnetism at synchrotron radiation facilities," *Review of Scientific Instruments*, vol. 86, no. 6, 2015.

[126] J. Grabis, A. Nefedov, and H. Zabel, "Diffractometer for soft x-ray resonant magnetic scattering," *Review of Scientific Instruments*, vol. 74, no. 9, pp. 4048–4051, 2003.

[127] C. Pearce, N. Telling, D. Vaughan, J. Charnock, E. Arenholz, and F. Tuna, "Iron site occupancies in magnetite-ulvospinel

solid solution: A new approach using XMCD," *American Mineralogist*, vol. 95, pp. 425–439, 2009.

[128] E. Stavitski and F. M. de Groot, "The CTM4XAS program for EELS and XAS spectral shape analysis of transition metal L edges," *Micron*, vol. 41, no. 7, pp. 687–694, 2010.

[129] S. Staniland, W. Williams, N. Telling, G. Van Der Laan, A. Harrison, and B. Ward, "Controlled cobalt doping of magnetosomes in vivo.," *Nature nanotechnology*, vol. 3, no. 3, pp. 158–162, 2008.

[130] E. C. Stoner and E. P. Wohlfarth, "A mechanism of magnetic hysteresis in heterogeneous alloys," *IEEE Transactions on Magnetics*, vol. 27, no. 4, pp. 3475–3518, 1991.

[131] J. Carrey, B. Mehdaoui, and M. Respaud, "Simple models for dynamic hysteresis loop calculations of magnetic single-domain nanoparticles: Application to magnetic hyperthermia optimization," *Journal of Applied Physics*, vol. 109, no. 8, 2011.

[132] W. T. Coffey and L. J. Geoghegan, "Differential recurrence relations for the Fokker-Planck equation for magnetic after-effect and dielectric relaxation in non axially symmetric potentials," *Journal of Molecular Liquids*, vol. 69, no. 9 SPEC. ISS., pp. 53–81, 1996.

[133] J. Li, Y. Pan, G. Chen, Q. Liu, L. Tian, and W. Lin, "Magnetite magnetosome and fragmental chain formation of Magnetospirillum magneticum AMB-1: Transmission electron microscopy and magnetic observations," *Geophysical Journal International*, vol. 177, no. 1, pp. 33–42, 2009.

[134] L. Jovane, F. Florindo, D. A. Bazylinski, and U. Lins, "Prismatic magnetite magnetosomes from cultivated Magnetovibrio blakemorei strain MV-1: A magnetic fingerprint in marine sediments?," *Environmental Microbiology Reports*, vol. 4, no. 6, pp. 664–668, 2012.

[135] J. M. Thomas, E. T. Simpson, T. Kasama, and R. E. Dunin-Borkowski, "Electron holography for the study of magnetic nanomaterials," *Accounts of Chemical Research*, vol. 41, no. 5, pp. 665–674, 2008.

[136] S. S. Kalirai, D. A. Bazylinski, and A. P. Hitchcock, "Anomalous Magnetic Orientations of Magnetosome Chains in a Magnetotactic Bacterium: Magnetovibrio blakemorei Strain MV-1," *Plos ONE*, vol. 8, no. 1, 2013.

[137] N. H. Sparks, S. Mann, D. A. Bazylinski, D. R. Lovley, H. W. Jannasch, and R. B. Frankel, "Structure and morphology of magnetite anaerobically-produced by a marine magnetotactic bacterium and a dissimilatory iron-reducing bacterium," *Earth and Planetary Science Letters*, vol. 98, no. 1, pp. 14–22, 1990.

[138] S. Mann, N. H. Sparks, and R. G. Board, "Magnetotactic bacteria: Microbiology, biomineralization, palaeomagnetism and biotechnology," *Advances in Microbial Physiology*, vol. 31, pp. 125–181, 1990.

[139] S. J. Clemett, K. L. Thomas-Keprta, J. Shimmin, M. Morphew, J. R. McIntosh, D. A. Bazylinski, J. L. Kirschvink, S. J. Wentworth, D. S. McKay, H. Vali, E. K. Gibson, and C. S. Romanek, "Crystal morphology of MV-1 magnetite," *American Mineralogist*, vol. 87, no. 11-12, pp. 1727–1730, 2002.

[140] O. Felfoul, M. Mohammadi, S. Taherkhani, D. De Lanauze, Y. Zhong Xu, D. Loghin, S. Essa, S. Jancik, D. Houle, M. Lafleur, L. Gaboury, M. Tabrizian, N. Kaou, M. Atkin, T. Vuong, G. Batist, N. Beauchemin, D. Radzioch, and S. Martel, "Magneto-aerotactic bacteria deliver drug-containing nanoliposomes to tumour hypoxic regions," *Nature Nanotechnology*, vol. 11, no. 11, pp. 941–947, 2016.

[141] D. Ortega and Q. A. Pankhurst, "Magnetic hyperthermia," *Nanoscience*, pp. 60–88, dec 2012.

[142] J. Van Der Zee, D. González González, G. C. Van Rhoon, J. D. Van Dijk, W. L. Van Putten, and A. A. Hart, "Comparison of radiotherapy alone with radiotherapy plus hyperthermia in locally advanced pelvic tumours: A prospective, randomised, multicentre trial," *Lancet*, vol. 355, no. 9210, pp. 1119–1125, 2000.

[143] T. Ohguri, H. Imada, H. Narisada, K. Yahara, T. Morioka, K. Nakano, Y. Miyaguni, and Y. Korogi, "Systemic chemotherapy using paclitaxel and carboplatin plus regional hyperthermia

and hyperbaric oxygen treatment for non-small cell lung cancer with multiple pulmonary metastases: Preliminary results," *International Journal of Hyperthermia*, vol. 25, no. 2, pp. 160–167, 2009.

[144] Y. Zhang, W. Zhang, C. Geng, T. Lin, X. Wang, L. Zhao, and J. Tang, "Thermal ablation versus conventional regional hyperthermia has greater anti-tumor activity against melanoma in mice by upregulating CD4+ cells and enhancing IL-2 secretion," *Progress in Natural Science*, vol. 19, no. 12, pp. 1699–1704, 2009.

[145] "Magforce®." See `https://www.magforce.com` for information on magnetic hyperthermia clinical trials carried out at MagForce company. Accessed: 2021-11-11.

[146] J. P. Fortin, C. Wilhelm, J. Servais, C. Ménager, J. C. Bacri, and F. Gazeau, "Size-sorted anionic iron oxide nanomagnets as colloidal mediators for magnetic hyperthermia," *Journal of the American Chemical Society*, vol. 129, no. 9, pp. 2628–2635, 2007.

[147] M. Ma, Y. Wu, J. Zhou, Y. Sun, Y. Zhang, and N. Gu, "Size dependence of specific power absorption of Fe3O 4 particles in AC magnetic field," *Journal of Magnetism and Magnetic Materials*, vol. 268, no. 1-2, pp. 33–39, 2004.

[148] Y. Piñeiro-Redondo, M. Bañobre-López, I. Pardiñas-Blanco, G. Goya, M. A. López-Quintela, and J. Rivas, "The influence of colloidal parameters on the specific power absorption of PAA-coated magnetite nanoparticles," *Nanoscale Research Letters*, vol. 6, pp. 1–7, 2011.

[149] R. E. Rosensweig, "Heating magnetic fluid with alternating magnetic field," *Journal of Magnetism and Magnetic Materials*, vol. 252, no. 1-3 SPEC. ISS., pp. 370–374, 2002.

[150] D. Serantes, K. Simeonidis, M. Angelakeris, O. Chubykalo-Fesenko, M. Marciello, M. Del Puerto Morales, D. Baldomir, and C. Martinez-Boubeta, "Multiplying magnetic hyperthermia response by nanoparticle assembling," *Journal of Physical Chemistry C*, vol. 118, no. 11, pp. 5927–5934, 2014.

[151] I. Andreu and E. Natividad, "Accuracy of available methods for quantifying the heat power generation of nanoparticles for magnetic hyperthermia," *International Journal of Hyperthermia*, vol. 29, no. 8, pp. 739–751, 2013.

[152] I. A. Brezovich, "Low Frequency Hyperthermia: Capacitive and Ferromagnetic Thermoseed Methods.," *Medical Physics Monograph No 16: Biological, physical, and clinical aspects of hyperthermia:*, pp. 82–110, 1988.

[153] P. De La Presa, Y. Luengo, M. Multigner, R. Costo, M. P. Morales, G. Rivero, and A. Hernando, "Study of heating efficiency as a function of concentration, size, and applied field in γ-Fe2O3 nanoparticles," *Journal of Physical Chemistry C*, vol. 116, no. 48, pp. 25602–25610, 2012.

[154] P. Guardia, R. Di Corato, L. Lartigue, C. Wilhelm, A. Espinosa, M. Garcia-Hernandez, F. Gazeau, L. Manna, and T. Pellegrino, "Water-soluble iron oxide nanocubes with high values of specific absorption rate for cancer cell hyperthermia treatment," *ACS Nano*, vol. 6, no. 4, pp. 3080–3091, 2012.

[155] R. Hergt and S. Dutz, "Magnetic particle hyperthermia-biophysical limitations of a visionary tumour therapy," *Journal of Magnetism and Magnetic Materials*, vol. 311, no. 1 SPEC. ISS., pp. 187–192, 2007.

[156] E. A. Périgo, G. Hemery, O. Sandre, D. Ortega, E. Garaio, F. Plazaola, and F. J. Teran, "Fundamentals and advances in magnetic hyperthermia," *Applied Physics Reviews*, vol. 2, p. 041302, dec 2015.

[157] C. Blanco-Andujar, F. Teran, and D. Ortega, "Current Outlook and Perspectives on Nanoparticle-Mediated Magnetic Hyperthermia," *Iron Oxide Nanoparticles for Biomedical Applications*, pp. 197–245, 2018.

[158] K. Simeonidis, M. P. Morales, M. Marciello, M. Angelakeris, P. De La Presa, A. Lazaro-Carrillo, A. Tabero, A. Villanueva, O. Chubykalo-Fesenko, and D. Serantes, "In-situ particles reorientation during magnetic hyperthermia application: Shape matters twice," *Scientific Reports*, vol. 6, no. April, p. 38382, 2016.

[159] R. Das, J. Alonso, Z. Nemati Porshokouh, V. Kalappattil, D. Torres, M. H. Phan, E. Garaio, J. Á. García, J. L. Sanchez Llamazares, and H. Srikanth, "Tunable High Aspect Ratio Iron Oxide Nanorods for Enhanced Hyperthermia," *Journal of Physical Chemistry C*, vol. 120, pp. 10086–10093, apr 2016.

[160] I. Conde-Leboran, D. Baldomir, C. Martinez-Boubeta, O. Chubykalo-Fesenko, M. Del Puerto Morales, G. Salas, D. Cabrera, J. Camarero, F. J. Teran, and D. Serantes, "A Single Picture Explains Diversity of Hyperthermia Response of Magnetic Nanoparticles," *Journal of Physical Chemistry C*, vol. 119, no. 27, pp. 15698–15706, 2015.

[161] A. Lohße, I. Kolinko, O. Raschdorf, R. Uebe, S. Borg, A. Brachmann, J. M. Plitzko, R. Müller, Y. Zhang, and D. Schüler, "Overproduction of magnetosomes by genomic amplification of biosynthesis-related gene clusters in a magnetotactic bacterium," *Applied and Environmental Microbiology*, vol. 82, no. 10, pp. 3032–3041, 2016.

[162] E. C. Abenojar, S. Wickramasinghe, J. Bas-Concepcion, and A. C. S. Samia, "Structural effects on the magnetic hyperthermia properties of iron oxide nanoparticles," *Progress in Natural Science: Materials International*, vol. 26, no. 5, pp. 440–448, 2016.

[163] L. C. Branquinho, M. S. Carrião, A. S. Costa, N. Zufelato, M. H. Sousa, R. Miotto, R. Ivkov, and A. F. Bakuzis, "Effect of magnetic dipolar interactions on nanoparticle heating efficiency: Implications for cancer hyperthermia," *Scientific Reports*, vol. 3, 2013.

[164] B. Gleich and J. Weizenecker, "Tomographic imaging using the nonlinear response of magnetic particles," *Nature*, vol. 435, no. 7046, pp. 1214–1217, 2005.

[165] A. Kraupner, D. Eberbeck, D. Heinke, R. Uebe, D. Schüler, and A. Briel, "Bacterial magnetosomes-nature's powerful contribution to MPI tracer research," *Nanoscale*, vol. 9, no. 18, pp. 5788–5793, 2017.

[166] J. Mosayebi, M. Kiyasatfar, and S. Laurent, "Synthesis, functionalization, and design of magnetic nanoparticles for theranostic applications," *Advanced Healthcare Materials*, vol. 6, no. 23, 2017.

[167] P. S. Patrick, Q. A. Pankhurst, C. Payne, T. L. Kalber, and M. F. Lythgoe, "Magnet-targeted delivery and imaging," *Design and Applications of Nanoparticles in Biomedical Imaging*, pp. 123–152, 2016.

[168] J. Riegler, A. Liew, S. O. Hynes, D. Ortega, T. O'Brien, R. M. Day, T. Richards, F. Sharif, Q. A. Pankhurst, and M. F. Lythgoe, "Superparamagnetic iron oxide nanoparticle targeting of MSCs in vascular injury," *Biomaterials*, vol. 34, no. 8, pp. 1987–1994, 2013.

[169] S. Martel and M. Mohammadi, "Switching between magnetotactic and aerotactic displacement controls to enhance the efficacy of MC-1 magneto-aerotactic bacteria as cancer-fighting nanorobots," *Micromachines*, vol. 7, no. 6, 2016.

[170] S. Rismani Yazdi, R. Nosrati, C. A. Stevens, D. Vogel, P. L. Davies, and C. Escobedo, "Magnetotaxis Enables Magnetotactic Bacteria to Navigate in Flow," *Small*, vol. 14, p. 1702982, feb 2018.

[171] I. S. Khalil, M. P. Pichel, B. A. Reefman, O. S. Sukas, L. Abelmann, and S. Misra, "Control of magnetotactic bacterium in a micro-fabricated maze," *Proceedings - IEEE International Conference on Robotics and Automation*, pp. 5508–5513, 2013.

[172] M. P. Pichel, T. A. Hageman, I. S. Khalil, A. Manz, and L. Abelmann, "Magnetic response of Magnetospirillum gryphiswaldense observed inside a microfluidic channel," *Journal of Magnetism and Magnetic Materials*, vol. 460, pp. 340–353, 2018.

[173] E. Alphandéry, "Applications of magnetosomes synthesized by magnetotactic bacteria in medicine.," *Frontiers in bioengineering and biotechnology*, vol. 2, no. March, p. 5, 2014.

[174] C. J. Pierce, E. Mumper, E. E. Brown, J. T. Brangham, B. H. Lower, S. K. Lower, F. Y. Yang, and R. Sooryakumar, "Tuning

bacterial hydrodynamics with magnetic fields," *Physical Review E*, vol. 95, no. 6, 2017.

[175] R. Bitter, T. Mohiuddin, and M. Nawrocki, *LabVIEW: Advanced programming techniques*. Crc Press, 2006.

[176] J. Y. Tinevez, N. Perry, J. Schindelin, G. M. Hoopes, G. D. Reynolds, E. Laplantine, S. Y. Bednarek, S. L. Shorte, and K. W. Eliceiri, "TrackMate: An open and extensible platform for single-particle tracking," *Methods*, vol. 115, pp. 80–90, 2017.

[177] "Trackmate Manual." `https://imagej.net/plugins/trackmate/getting-started/`. [Online accessed 05-Jan-2022].

[178] R. E. Kalman, "A new approach to linear filtering and prediction problems," *Journal of Fluids Engineering, Transactions of the ASME*, vol. 82, no. 1, pp. 35–45, 1960.

[179] E. W. Esch, A. Bahinski, and D. Huh, "Organs-on-chips at the frontiers of drug discovery," *Nature Reviews Drug Discovery*, vol. 14, no. 4, pp. 248–260, 2015.

List of publications resulting from this thesis

1. D. Gandia, L. Gandarias et al., "Unlocking the Potential of Magnetotactic Bacteria as Magnetic Hyperthermia Agents," *Small*, vol. 15, pp. 1902626, 2019.

2. D. Gandia et al., "Elucidating the role of shape anisotropy in faceted magnetic nanoparticles using biogenic magnetosomes as a model," *Nanoscale*, vol. 12, no. 30, pp. 16081–16090, 2020.

3. L. Marcano, I. Orue, D. Gandia, L. Gandarias, M. Weigand, R. abrudan, A. García-Prieto, A. García-Arribas, A. Muela, M.L Fdez-Gubieda and S. Valencia, "Magnetic anisotropy of individual nanomagnets embedded in biological systems determined by axi-asymmetric x-ray transmission microscopy". Submitted to ACS Nano, under referees.

4. D. Gandia, L. Gandarias, L. Marcano, I. Orue, J. Alonso, A. Muela and M.L Fdez- Gubieda, "Magnetic characterization of *Magnetospirillum magneticum*". Under Preparation.

Other publications

- P. G. Saiz, D. Gandia et al., "Enhanced mass sensitivity in novel magnetoelastic resonators geometries for advanced detection systems," *Sensors Actuators, B Chem.*, vol. 296, no. May, p. 126612, 2019.